OPTIMIZED EVALUATION OF BONE TISSUE MATERIAL PROPERTIES BY INVERSE FINITE ELEMENT ANALYSIS AND FEMUR FRACTURE TESTING

A Dissertation
Submitted to the Graduate Faculty
of the
North Dakota State University
of Agriculture and Applied Science

By

Samad Javid

In Partial Fulfillment of the Requirements
for the Degree of
DOCTOR OF PHILOSOPHY

Major Department:
Mechanical Engineering

October 2014

Fargo, North Dakota

North Dakota State University
Graduate School

Title

OPTIMIZED EVALUATION OF BONE TISSUE MATERIAL PROPERTIES BY INVERSE FINITE ELEMENT ANALYSIS AND FEMUR FRACTURE TESTING

By

Samad Javid

The Supervisory Committee certifies that this ***disquisition*** complies with North Dakota State University's regulations and meets the accepted standards for the degree of

DOCTOR OF PHILOSOPHY

SUPERVISORY COMMITTEE:

Dr. Ghodrat Karami
Chair

Dr. Mariusz Ziejewski

Dr. Fardad Azarmi

Dr. Kambiz Farahmand

Dr. Dan Dragomir-Daescu

Approved:

4/9/2015	Dr. Alan Kallmeyer
Date	Department Chair

ABSTRACT

The main objective of this research is to characterize bone inhomogeneous elastic, yield, and post-yield behaviors, using a computational-experimental approach. The current study uses the force-displacement results of one hundred four cadaveric femora that were previously tested to fracture in a fall on the hip loading configuration. Recorded force-displacement data are used to determine stiffness, yield force, and femoral strength values. Finite element (FE) models of the femora are developed from the quantitative computed tomography scans captured before the fracture tests. A power law, or a sigmoid function, is used to determine the elastic modulus from the ash densities for each case modeled. The models are used for FE simulations that mimic the experiments. Inverse finite element analysis is employed to identify the unknown coefficients in the bone density-elasticity relationships. Optimization algorithms are used to minimize the error function between the experimental and FE estimated results in a large subset of female femora. The results of the obtained relationships show a good agreement with the experimental data. This contributes to a coefficient of determination of 70%, which is higher than those of previously proposed density-elasticity relationships on the same set of femora. The parts of the bones with the densities up to 0.5 g/cm^3, play an important role in the deformation of the neck and the head of the femur. While power law and sigmoid function show similar correlation in the prediction of stiffness, distribution of stresses and strains are notably different, showing different response in the yield and post-yield behavior.

To simulate the material damage, a power density-yield strain relationship is used as the failure criterion in FE models, assuming a ductile and a brittle material behavior for the bone. The unknown coefficients in the density-yield strain relationship are identified for the ductile and brittle material models. The ductile material model shows a more realistic post-yield behavior

than the brittle model, but it is computationally expensive and may face convergence issues due to nonlinearities. The brittle material model, on the other hand, estimates the bone strength fairly and, due to its simplicity, it seems more applicable for clinical use.

ACKNOWLEDGMENTS

I am very grateful to Professor Ghodrat Karami, my advisor in the Department of Mechanical Engineering, North Dakota State University (NDSU), for his outstanding and invaluable support, guidance, and mentorship during my graduate education. I would also like to thank Dr. Dan Dragomir-Daescu for allowing me the opportunity to perform research on femoral fracture in the Division of Engineering (DOE) at Mayo Clinic and for encouraging me to use the research for my dissertation. I wish to thank all of my Advisory Committee members for their valuable guidance throughout my PhD research; and the entire faculty, staff, and my friends in the Department of Mechanical Engineering (ME) at NDSU for their help and support, as well.

I thank my colleagues in the DOE, Mayo Clinic, for their help and for providing a collaborative and fun work environment. Above all, I would especially like to thank Asghar Rezaei for his inspiration, his very helpful comments in my dissertation, and for his friendship. I also want to give special appreciation to Sean McEligot for his assistance in resolving the details regarding Mayo Clinic's Intellectual Property and Copyright. I would like to thank Dr. Philip Araoz in the Department of Radiology, Mayo Clinic, for offering me a secondary research job which provided financial support during the second year of my dissertation research at Mayo Clinic.

I want to express special gratitude to Dr. Don and Rosella Kvernen, as well as to Dr. Jarrett and Linda Richardson for their endless friendship, kindness, and support throughout my time in Rochester.

I thank the Army Research Office for the financial support of the first two years of my PhD study at NDSU. With their financial support, I was able to publish two journal papers. I also acknowledge the funding support for my thesis from the National Institutes of Health (NIH)

(grant AR027065Z-30S1) and the Grainger Foundation (Grainger Innovation Fund). The QCT imaging of the femora was performed through the Opus CT Imaging Resource of Mayo Clinic (NIH construction grant RR018898).

Finally, I am forever grateful to my family; to my kind and supportive wife, Haydeh, and to my lovely children, Mohammad and Suzan. Undoubtedly, without their help, endless support and sacrifice, and inspiration I would not have been able to pursue my dream of earning a PhD.

PREFACE

This work was supported by Mayo Clinic and was carried out while I was working at the DOE, Mayo Clinic. I declare that the copyright of any unpublished material in this thesis belongs to Mayo Clinic. I started my one-year internship at the DOE in May 2012. The bone material optimization, as a part of the quantitative computed tomography based finite element analysis (QCT/FEA) bone project, was determined, by my Advisory Committee, to be my PhD research. Many people had worked or have been working on this project. Several experimental fracture bone tests had been carried out before I joined the group. The experimental data analysis (EDA) and the QCT/FEA method had been established, as well. The main focus of my dissertation was on the material properties of the femoral bones for which I used the previous experimental data, the QCT/FEA method, and the ANSYS APDL and TCL scripts developed in-house.

I highly appreciate the work and contributions of Sean McEligot, Dan Dragomir-Daescu, Timothy Rossman, Susheil Uthamaraj, Rachel Entwistle, and several other individuals (Alex Cong, Jorn op Den, …) who left the project before I started working with it. Without their help and previous work, I would not have been able to complete my dissertation at Mayo Clinic.

TABLE OF CONTENTS

LIST OF TABLES

LIST OF FIGURES

CHAPTER 1. INTRODUCTON AND BACKGROUND

Bones are the main component of the skeletal system in the human body. The general health situation of a person is significantly affected by the health condition of his/her bones. The structural integrity of the human skeleton system is continuously challenged by mechanical environmental loads. In younger age ranges, bones usually fracture only when they are exposed to loads considerably greater than those in normal daily activities. Falls from heights, motor vehicle accidents, and sports-related traumas are the main causes of bone fractures in young individuals. Attempts to prevent or moderate bone fractures caused by these kinds of activities mostly focus on designing safer protective environments and equipment in order to decrease the applied loads to levels below bone strength. In contrast, bone fractures in older people usually result from incidents which significantly expose lower energies to the bones, such as lifting weights or falling from a standing height. The primary reasons for these types of fractures are increased bone fragility and reduced bone strength due to osteoporosis. The main interventions to reduce osteoporotic fractures are treatment of osteoporosis, fall prevention, and use of protective mechanisms such as energy absorbing floors and hip padding to decrease the energy level transmitted to the skeletal system [1].

Bone fracture is a focal public health problem in the elderly population due to its morbidity and mortality side effects [2]. In the last few decades, a huge amount of research has been forwarded toward understanding the mechanisms and risk predictors of bone fractures [3-11]. Traditionally, reduction in bone mineral density (BMD) and deterioration of bone microarchitecture has been considered as the main predictor of fracture risk [4, 12]. In addition to low BMD, however, other factors such as age, sex, low body weight, height, etc. affect bone fracture [9, 13-15]. BMD alone, therefore, cannot predict bone fracture risk [16-19].

This chapter describes a general mechanistic understanding of human bone functions, composition, and structure required to recognize the mechanisms of bone fracture and to develop new methods to predict bone fracture risk.

1.1. Bone Functions in the Skeletal System

As a vital component of the skeletal system, bones execute a variety of functions in the body. Their multi-functions can be categorized into three main classes:

I. Mechanical functions [20]:

- Protection: bones act to support and protect delicate and important organs at different locations inside the body. For instance, the skull protects the brain, or the ribcage supports the heart.
- Shape: due to their stiff nature, bones deliver a rigid framework around which the body is formed.
- Movement: bones collaborate with other skeletal components such as joints, ligaments, tendons, and muscles to comprise the moving mechanism of the body.

II. Metabolic functions [21, 22]:

- Mineral Storage: bones store vital minerals such as phosphorus and calcium.
- Fat storage: bones accumulate fats in the yellow bone marrow of long bones.
- Preservation of pH balance in blood: bones regulate the pH in blood by releasing or absorbing alkaline salts.
- Detoxification: bones detoxify the body by removing heavy metals and other foreign elements from the blood and storing them to decrease their effects on other organs.

III. Synthetic function [23]:

- Production of blood cells: one of the main functions of the bone marrow, which is located inside the long bones, is to produce red and white blood cells in a process called hematopoiesis.

1.2. Composition and Hierarchical Structure of the Bone

Bone is a natural composite material with unique structure and material properties. It has three main constituents: 1) an organic matrix (primarily type-I collagen), 2) an inorganic ceramic reinforcement (predominantly hydroxyapatite), and 3) water. By weight, bone is composed of 60% hydroxyapatite, 30% collagen, and 10% water [24]. Bone can be examined on a hierarchical structure with, at least, five scale levels (Figure 1.1): 1) macro-scale, 2) micro-scale (from 10 to 500 μm), 3) sub-micro-scale (1–10 μm), 4) nano-scale (from a few hundred nanometers to 1 μm), and 5) sub-nano-scale (below a few hundred nanometers) [25].

At macro-scale, there are two types of bone material: 1) cortical (compact) and 2) trabecular (cancellous or spongy) bone. Cortical bone, with a porosity of 5-30%, is the denser bone which forms the outer cortex, or the shell, of bones. It is stiffer, harder, and stronger than trabecular bone. By weight, about 80% of a human skeleton consists of cortical bone [26, 27]. Trabecular bone is a porous structure (30-90% porosity) surrounded by the cortical tissue. Due to its lower density, trabecular bone has a greater surface area to mass compared to cortical bone, leading to a weaker, more flexible, and softer structure [28]. At micro-scale level, the primary anatomical units of cortical and trabecular bones are osteons and trabeculae (trabecular packets), respectively [29]. Osteons are made up of organized cylindrical lamellae with central haversian (vascular) canals, while trabeculae are composed of beam, strut, or rod-like lamellae. At the sub-

micro-scale level, lamellae consist of collagen fibers of ~ 100 nm in diameter. Depending on the location in the bone, they can be cylindrical or parallel plate lamellae.

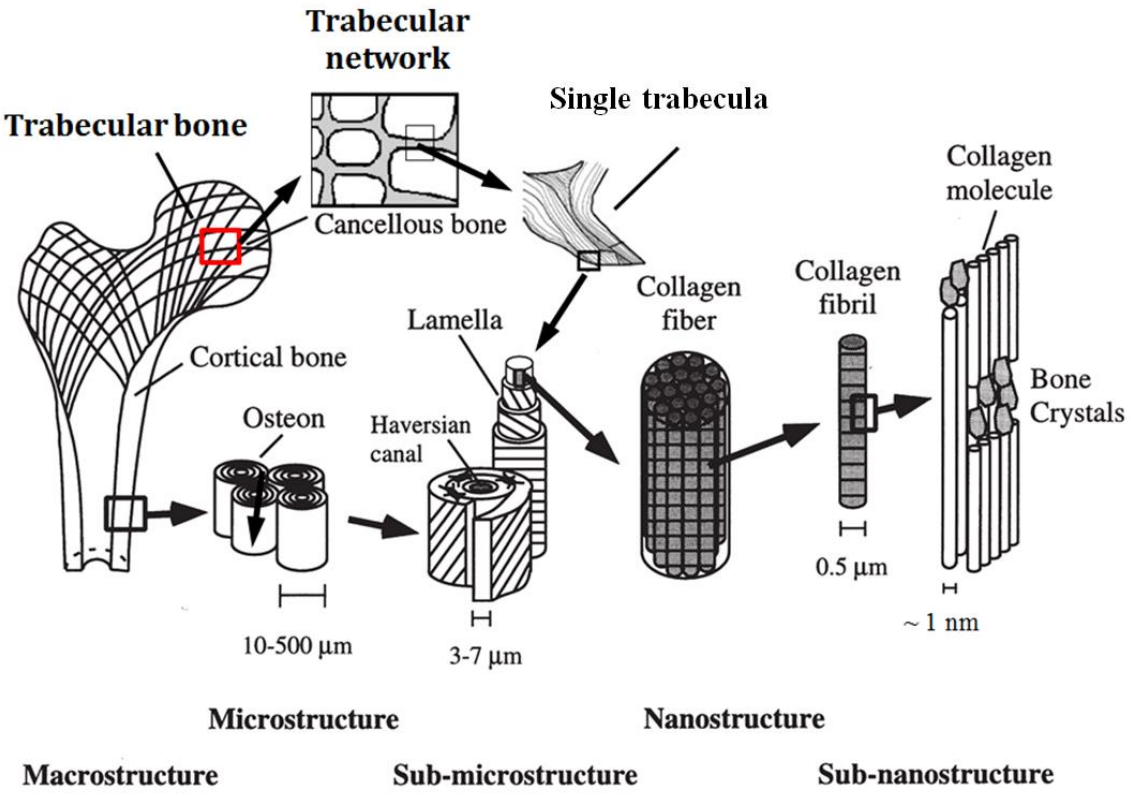

Figure 1.1. Hierarchical structure of bone with five scale levels scales: macro-scale, micro-scale (from 10 to 500 μm), sub-micro-scale (1–10 μm), nano-scale (from a few hundred nanometers to 1 μm), and sub-nano-scale (below a few hundred nanometers). (Modified from [25]).

At nano-scale, collagen fibrils lump together to create collagen fibers. The mineralized collagen fibrils organize themselves into several structures: circumferential, twisted, or parallel (Figure 1.2). At sub-nano-scale level, the smallest hierarchical scale level, tropocollagen chains assemble together to form collagen fibrils. Hydroxyapatite minerals (5 nm thickness, ~50-100 nm lateral dimension) disperse between the gap regions and around collagen to create mineralized collagen fibrils (Figure 1.3). Three helixes of α-collagen molecular chains, made up of amino acids, bundle together to form tropocollagen (300 nm length, 1.5 nm diameter), the primary unit of the bone.

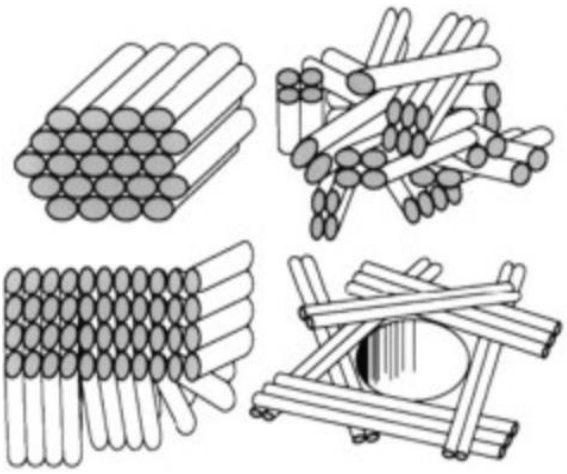

Figure 1.2. Fibril array patterns; mineralized collagen fibrils are organized in circumferential, twisted, or parallel structures at different bone locations. (Modified from [24]).

1.3. Osteoporosis and Hip Fracture

Osteoporosis is a progressive skeletal disorder characterized by microstructural degradation of bone tissue and low bone mass [30]. Figure 1.4 shows the cross sections of a normal bone and an osteoporotic bone. As illustrated, the anatomical structures are thinner in the osteoporotic bone. This leads to an increase in porosity and reduction in bone mass. Bones are alive and change continually throughout life. Bone cells die and dissolve in a process called bone resorption [31], and new bone cells grow back in a process named ossification [32]. The whole process of bone turnover is called bone remodeling. This process controls the healing or reshaping of bones after fractures and allows bones to adapt themselves against mechanical loadings [33]. Each year around 10% of an adult skeleton is remodeled, thus the entire skeleton is renewed completely every 10 years [34]. After reaching the peak bone mass at age of 30, bone density decreases naturally for everyone, and around age of 35 bones gradually become weaker. In osteoporotic bones, metabolic processes destroy the balance between the creation of new bone tissue and removal of the old bone tissue, thus bone mass reduction happens faster than in normal bones. Consequently, bones become weak, brittle, and susceptible to fracture [35].

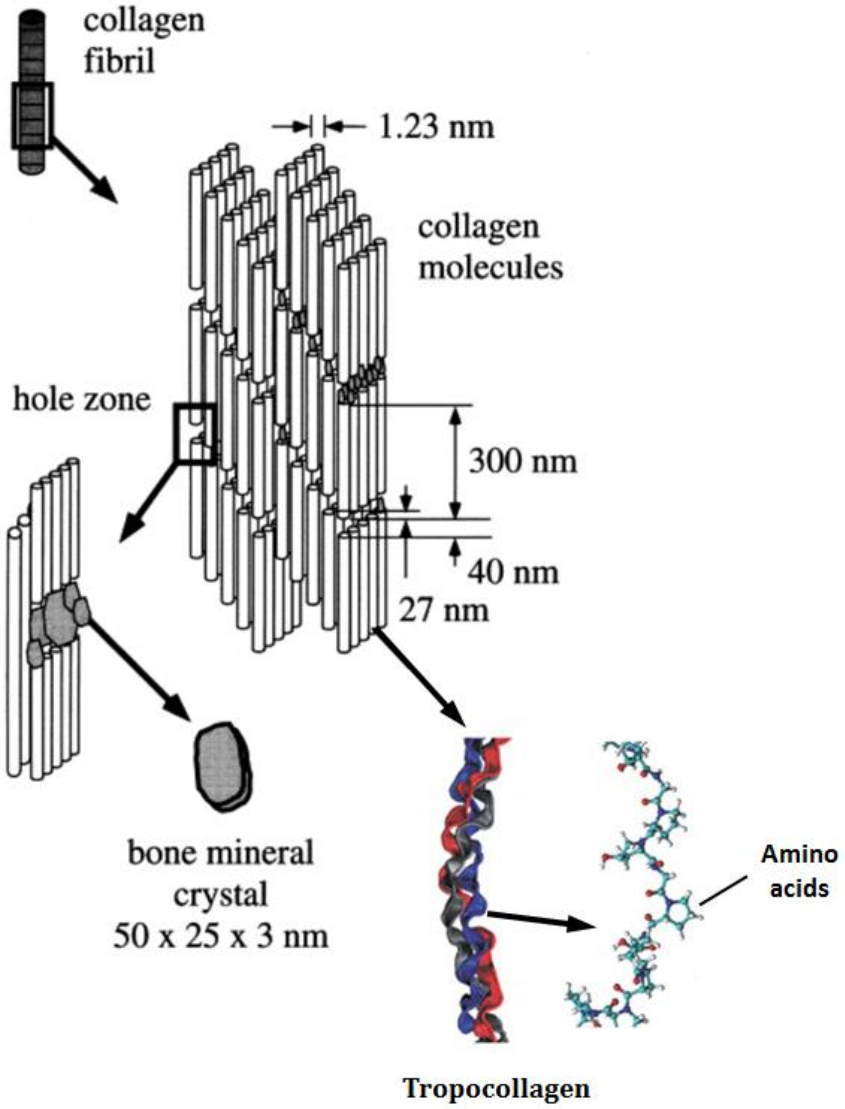

Figure 1.3. Tropocollagen, the smallest hierarchical level of the bone; three helixes of α-collagen molecular chains of amino acids form collagen molecules. Hydroxyapatite minerals are scattered between the gap regions and around collagen molecules to reinforce the collagen fibrils. (Modified from [2, 25]).

According to a report released recently by National Osteoporosis Foundation (NOF), osteoporosis or low bone mass affects around 54 million Americans, which exposes them to a high risk for bone fracture. In 2010, 27.5 million people were estimated to have osteoporosis in the European Union (EU). Scientists estimate this number will increase by 23% and reach to 33.9 million by 2025 [36].

Figure 1.4. Cross-section of normal and osteoporotic bones; due to the deterioration of bone microarchitecture and substantial loss of bone mineral density, osteoporotic bones are weaker and more fragile, making them more susceptible to fracture. (© 2014 WebMD, LLC. All rights reserved).

Women are three times more likely than men to become osteoporotic. This is partly due to the biological changes, such as estrogen deficiency, happening in women at menopause; partly due to the lower age for peak bone mass in women; and partly because of the longer life of women compared to men, which leads to greater reductions in females bone mass [30]. Osteoporosis is usually specified as a silent disorder because it does not have any symptoms, and patients do not feel their bones getting weaker and more fragile. A bone fracture is frequently the first sign of osteoporosis [30].

Osteoporosis is a leading public health concern in the elderly population, due to its association with increased risk of bone fracture [37]. Statistics show that osteoporosis will cause a bone fracture in almost 50% of women and up to 25% of men age 50 and older [30]. There were about nine million osteoporosis-related fractures worldwide in 2000. In that year, osteoporotic fractures cost around €30 billion in the EU and $20 billion in the United States (US)

[38]. In 2010, approximately 3.5 million new bone fractures occurred in the EU. This number is expected to increase by 28% and reach 4.5 million in 2025 [39]. The NOF estimates that the occurrence of osteoporotic fractures in the US will reach three million, by 2025, with a $25.3 billion annual cost.

Hip fracture, occurring in the proximal part of the femur (Figure 1.5), is the most catastrophic type of bone fracture, due to its association with morbidity and mortality [9, 40, 41]. Around 1.6 million hip fractures occur around the world each year, and by 2050 this number is predicted to reach 6.3 million [42]. Hip fractures are among the most expensive medical treatments. In 2011, US hospitals treated 316,000 hip fractures with an aggregated cost of around $4.9 billion [43]. A hip fracture can cost a patient more than $81,000 during their lifetime. Hip fractures lead to increased risk of death, mainly due to diseases caused by the immobility after a hip fracture [44]. Approximately 25% of patients with a hip fracture die within a year of their fracture injury [9, 40]. Falling is one of the main risk factors for hip fractures, with falls from standing height, especially sideways falls, being the main cause of more than 90% of hip fractures [45-47]. Women sustain 75% of all hip fractures [48].

1.4. Assessment of Bone Fracture Risk

The current golden standard to diagnose osteoporosis and to assess bone fracture risk is to measure the areal bone mineral density (aBMD, g/cm^2) by Dual-energy X-Ray Absorptiometry (DEXA) [49]. The best location to measure aBMD is the neck or the whole proximal part of the femur (Figure 1.6A). The measured aBMD for an individual is compared to the average aBMD of healthy young adults whose aBMD has an approximately Gaussian normal distribution, regardless of the measurement method.

Figure 1.5. A hip fracture occurring in the proximal part of the femur, near the hip. (© 2014 WebMD, LLC. All rights reserved).

The difference between the measured aBMD and the reference value (the mean value of the aBMD distribution of a young healthy population), in terms of standard deviation (SD) units, is determined as a standard T score value (Figure 1.6B). Based on the T score value, bone condition is classified into one of the following categories (Figure 1.6C) which have been established by the World Health Organization (WHO) [50, 51]:

A. Normal: the bone has an aBMD equal to, or greater than, 1 SD below the reference value (T score $\geq$ -1)
B. Osteopenia: the measured aBMD is less than 1 SD below the reference value, but greater than 2.5 SD below this value (-2.5 < T score < -1)
C. Osteoporosis: the measured aBMD is equal to, or less than, 2.5 SD below the reference value (T score $\leq$ -2.5).

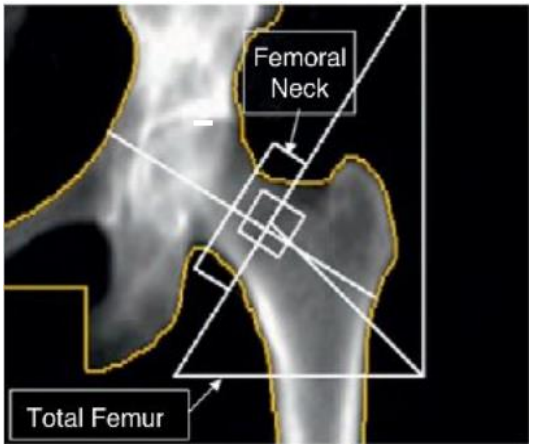

A

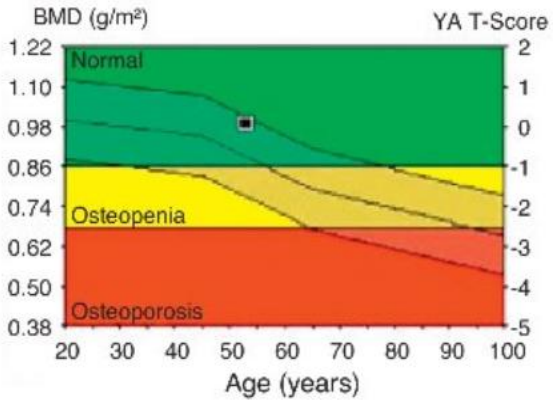

B

Category	T score range
Normal	T score ≥ -1
Osteopenia	-2.5 < T score < -1
Osteoporosis	T score ≤ -2.5

C

Figure 1.6. Measuring the aBMD by DEXA to quantify bone condition and to measure bone fracture risk: A) femoral neck and the whole proximal femur are the best locations to measure aBMD; B) bone condition based on T score compared to the reference aBMD value; and C) assessment of the bone health condition based on the measured T score.

1.5. Motivation of the Research

Although the current clinical benchmark for estimating bone osteoporosis, aBMD, has been used widely as a strong and effective predictor of risk for bone fracture [52, 53], it has a number of limitations:

- Areal bone mineral density has only a moderate correlation to bone fracture [17]. Numerous femur fractures have been reported to occur in people without osteoporosis, i.e. with a T-score greater than -2.5. The view is growing that intervention should not, therefore, be based solely on aBMD [16-19].

- It does not take into account bone shape, geometry, and microarchitecture, even though these are among the major factors that affect bone strength [54, 55].
- It cannot discern cortical bone from trabecular structure, while both contribute considerably to bone strength [54].
- It only measures bone density in a small two-dimensional (2D) area of the bone, while the three-dimensional (3D) distribution and varied material properties in the whole bone significantly affect bone strength [56].
- It does not account for various loading scenarios, while the mechanical behavior of the bone, like with other mechanical structures, differs considerably by the way it is loaded.

Quantitative computed tomography based finite element analysis (QCT/FEA) is a non-invasive method which can predict the mechanical behavior of bones against different loadings, and thus it has the potential to improve the assessment of bone fracture risk in patients beyond aBMD [57-61]. Evaluation of spatial distribution of material properties throughout the bone, which affects the FE simulation results significantly [62], has been a major challenge for bone researches for the last two decades [63]. Despite the huge amount of valuable research that has been conducted on the characterization of inhomogeneous material properties of the bone [64-66], there is still controversy regarding a robust material model to predict the bone behavior, especially under a complex loading scenario [67, 68]. Moreover, there is no material model specifically for female bones, while the prevalence of osteoporosis and hip fractures is greater for women [39, 48].

1.6. Research Objectives and Scope

The objectives of this research were to evaluate bone elastic, plastic, and damage material models in order to achieve accurate estimations of the overall femoral stiffness, ultimate

strength, and post-yield behavior in a fall on the hip. Three approaches were combined to achieve the goals of the research. First, the results of 104 human cadaveric proximal femora being previously tested to fracture, simulating sideways fall on the hip events, were utilized. The results included bone stiffness, yield point, ultimate strength point, and final fracture point which previously determined from recorded force-displacement graphs of each femur [69]. Secondly, the femoral fracture experiments were simulated in the finite element method (FEM) for seventy of these femora belonging to females. To this end, 3D geometric models of the femora were previously reconstructed from the QCT scans captured before the fracture tests. The models were meshed into finite elements (FEs). Boundary conditions (BCs), mimicking the experimental setup, were then applied on the models [54].

In the current study, density-dependent material properties were assigned to the elements, and the models were run in FE software to simulate the experiments. Estimated force-displacement graphs were derived from the FE simulations. Stiffness, yield point, ultimate strength point, and final fracture point were then determined from these graphs in the same way that they were determined from the experimental results. Finally, optimization algorithms were employed to evaluate the inhomogeneous elastic property of the female bone by minimizing error functions between the experimental and FE estimated results. To this end, the 70 female femora were randomly divided into two groups of 35 femora. The first group, called the training set, was used to evaluate the material models, and the second group, named the validation set, was used to cross-validate the obtained material models.

Furthermore, a ductile and a brittle material model were used separately for the bone tissue in the FE modeling of a set of nine female femora, selected from the fractured specimens, to investigate the yield and damage behavior of femoral bones under a complex loading scenario.

Optimization algorithms integrated with an inverse computational-experimental study were employed to find the unknown coefficients in the yield and post-yield material models by matching the FE estimated results to their experimental counterparts. Finally, the performance of the ductile and brittle material models for using in the subject-specific modeling of femora was cross-validated on another set of nine female femora.

CHAPTER 2. CADAVERIC FEMORAL FRACTURE TESTS AND QUANTITATIVE COMPUTED TOMOGRAPHY-BASED FINITE ELEMENT ANALYSIS METHOD

2.1. Introduction

It is necessary to fully understand the biomechanical processes involved in bone fractures in order to understand the mechanical behavior of the skeletal system, to recognize the mechanisms of bone fractures, and to develop novel methods for fracture risk assessment. Biomechanical experiments such as, ex-vivo strength testing of human cadaveric bones, can provide important insights to these processes [70, 71]. Cadaveric femoral strength testing in a fall on the hip configuration is very effective in determining the relationship between femoral strength and factors affecting the structural capacity of the femur [53].

Courtney et al. [70, 72] mechanically tested a number of cadaveric femora under loading rates of 2 mm/s and also of 100 mm/s and showed that the fracture load increased significantly with a high rate. However, energy absorption did not increase with an increased loading rate. They found that femoral fracture risk increased with aging. Eckstein et al. [73] performed fracture tests on human cadaveric femora to investigate the correlation between femoral strength (fracture load) and aBMD. They determined the differences between the strength of the left and right femora and used those calculations to evaluate the precision error of mechanical tests in a sideways fall configuration. Pinilla et al. [74] studied the effect of loading direction on the femoral fracture load. They concluded that the influence of loading direction on the fracture load was as significant as the effect of aging. Roberts et al. [75] performed a set of femoral cadaveric fracture tests to develop a new biomechanical femoral fracture risk assessment, named the factor of risk, which was equal to the ratio of applied load to bone strength. They concluded that their

newly developed factor of risk might predict patients femoral fracture risk more precisely than BMD. Pulkkinen et al. [76] conducted mechanical fracture tests on human cadaveric femora in a sideways fall configuration and showed that bone geometry and trabecular structure could estimate femoral fracture loads with the same accuracy as DEXA.

The objectives of the current chapter were to achieve the following goals:

I. To study the effects of aBMD, age, sex, and femoral geometric parameters on femoral strength (fracture load),
II. To characterize the sequence of events leading to femoral fracture during sideways falls by employing high speed video recordings,
III. To investigate femoral fracture locations and patterns by using 3D models reconstructed from high-resolution QCT scans of the femora after fracture tests,
IV. To produce a set of benchmark data for developing a QCT/FEA method to assess bone fracture risk and for characterizing bone material's elastic, yield, plastic, and damage properties, using inverse computational-experimental approaches.

2.2. Mechanical Fracture Tests[1]

One hundred four fresh-frozen human cadaveric femora (100 unpaired and four paired, 50 left and 54 right side) had been tested previously, at Mayo Clinic, to fracture in a sideways fall on the hip loading configuration. The procedure of sample preparation, fracture tests, and the experimental data analysis to extract the force-displacement data had been formerly reported [54, 67]. The characteristics of the bones used in the experimental fracture tests are presented in Table 2.1. Figure 2.1 shows the experimental setup.

[1] This is a part of a manuscript entitled "Experimental proximal femur fractures of osteoporotic, osteopenic, and normal femora in a fall on the hip configuration", Dan Dragomir-Daescu, Samad Javid, Tim Rossman, Susheil Uthamaraj, Sean McEligot, Michael Yaszemski, Philip Araoz (in preparation); used with permission of Mayo Foundation for Medical Education and Research, all rights reserved.

Table 2.1 Characteristics of the femora specimens. (Used with permission of Mayo Foundation for Medical Education and Research, all rights reserved).

	Female	**Male**	**All**
Age (*year*) mean ± SD, range	71 ± 14, [37-99]	67 ± 164, [34-91]	70 ± 15, [34-99]
Neck aBMD (g/cm^2) mean ± SD, range	0.725 ± 0.191, [0.374-1.363]	0897 ± 0.199, [0.469-1.424]	0.781 ± 0.209, [0.374-1.424]
Total hip aBMD (g/cm^2) mean ± SD, range	0.785 ± 0.216, [0.394-1.394]	0.992 ± 0.187, [0.560-1.414]	0.853 ± 0.228, [0.394-1.414]
Condition based on neck aBMD (*no.*)	Normal: 11 Osteopenic: 24 Osteoporotic: 35	Normal: 18 Osteopenic: 13 Osteoporotic: 3	Normal: 29 Osteopenic: 37 Osteoporotic: 38

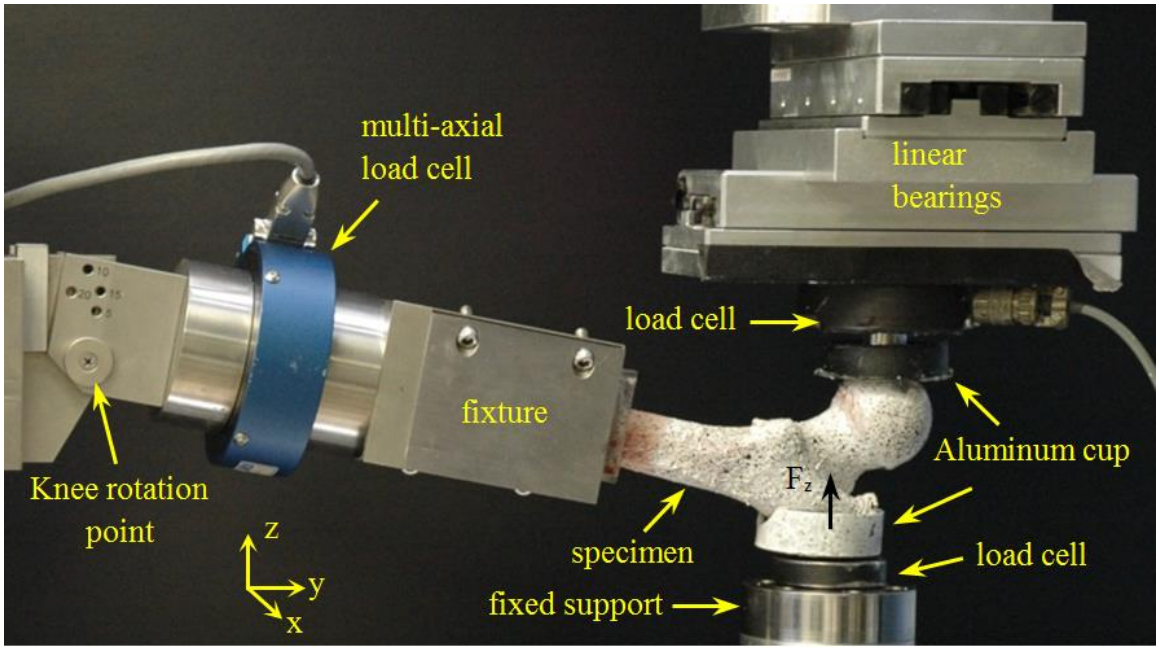

Figure 2.1 Photograph of the fracture experimental setup; the femoral shaft distal end, cured in an acrylic container with dental cement, was clinched in a fixture. The bone shaft was initially positioned at an angle of 10º compared to the horizon and was free to rotate around an x-axis passing through the knee rotation point. The MTS hydraulic ram moved down with a constant velocity of 100 *mm/s* [69].

Figure 2.2 demonstrates a schematic graph of experimental force-displacement data of a femur. As illustrated, the slope of the linear elastic part indicated the stiffness (K, *N/mm*) of the bone. The yield point of the bone was identified upon horizontal deviation of 2% from the linear elastic part which was almost equivalent to 0.2% in stress-strain curve of the femur. The femur

then underwent plastic deformation up to femoral strength which was the maximum force (F_s, *N*). Afterward, the force started declining to the fracture point (F_f, *N*).

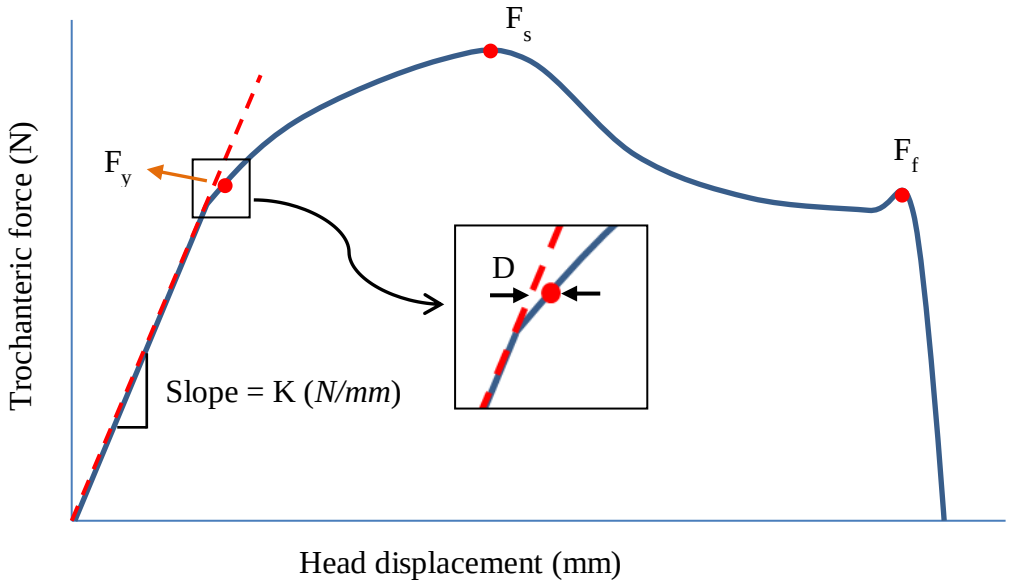

Figure 2.2. A schematic trochanteric force versus head displacement graph for a fractured femur; the slope of the linear elastic part was considered as the femoral stiffness (K, *N/mm*). The onset of the yield was the first point on the graph which had a horizontal distance (D) equal or greater than 2% from the regression line of the elastic region. The maximum force was bone strength (F_s, *N*) and the force at the final fracture point was called fracture load (F_f, *N*).

2.3. Classification of Fracture Types[2]

Fractures in long bones may be categorized based on location, type, severity, and bone dislocation. One of the widely used classification systems of bone fractures, defined in terms of fracture location and severity, is Müller AO Classification of Fractures-Long Bones [77]. Based on this method, proximal femur (hip) fractures can be classified into four groups: 1) subcapital, 2) transcervical, 3) intertrochanteric, and 4) pertrochanteric (Figure 2.3). In consultation with an orthopedic expert and using post-fracture 3D geometric models and high-speed videos, fractures in broken femora were classified [69].

[2] This section is a part of a manuscript entitled "Experimental proximal femur fractures of osteoporotic, osteopenic, and normal femora in a fall on the hip configuration", Dan Dragomir-Daescu, Samad Javid, Tim Rossman, Susheil Uthamaraj, Sean McEligot, Michael Yaszemski, Philip Araoz (in preparation); used with permission of Mayo Foundation for Medical Education and Research, all rights reserved.

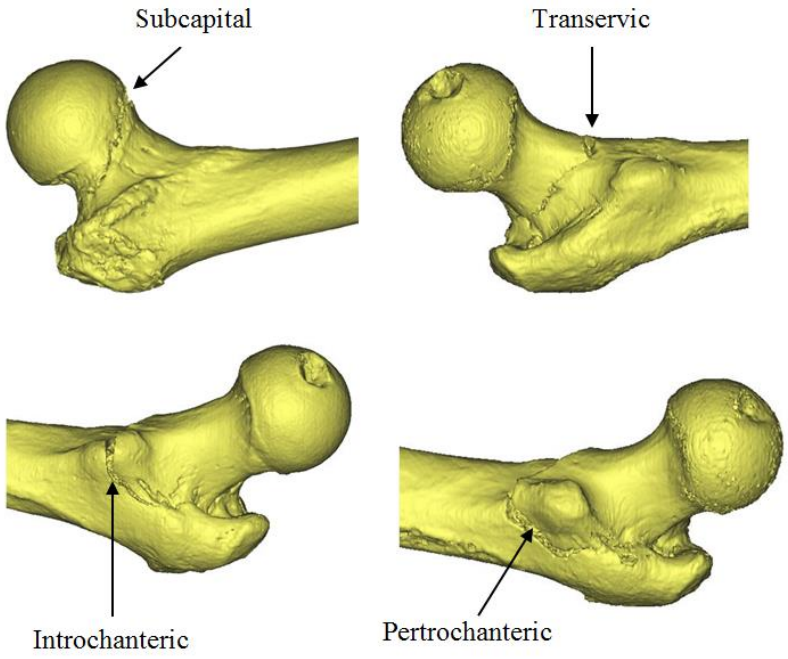

Figure 2.3. Classification of femoral fractures based on Müller AO Classification of Fractures-Long Bones. (Used with permission of Mayo Foundation for Medical Education and Research, all rights reserved).

2.4. QCT/FEA Method

QCT/FEA is a new method that aims to improve the assessment of femoral fracture risk in patients [18, 19, 54, 55, 78-80] beyond what is currently available using DEXA [81]. QCT/FEA better accounts for the spatial distribution of bone geometry and bone material properties [54, 82] and can estimate local stress and strain distributions [83-85] throughout the femur under different loading conditions [57, 63, 86-88]. Figure 2.4 illustrates the steps employed in the QCT/FEA procedure to simulate a femoral fracture event in a fall on the hip configuration [54]. First, QCT scans of multiple slices of each specimen were captured. A 3D geometric model was then developed from the QCT scans of each femur and subsequently was meshed into finite elements. Inhomogeneous material properties were applied to the finite elements. A boundary condition (BC) type mimicking a fall on the hip configuration was

enforced. The FE model was run to simulate the mechanical behavior of the specimen under a sideways fall loading impact [54].

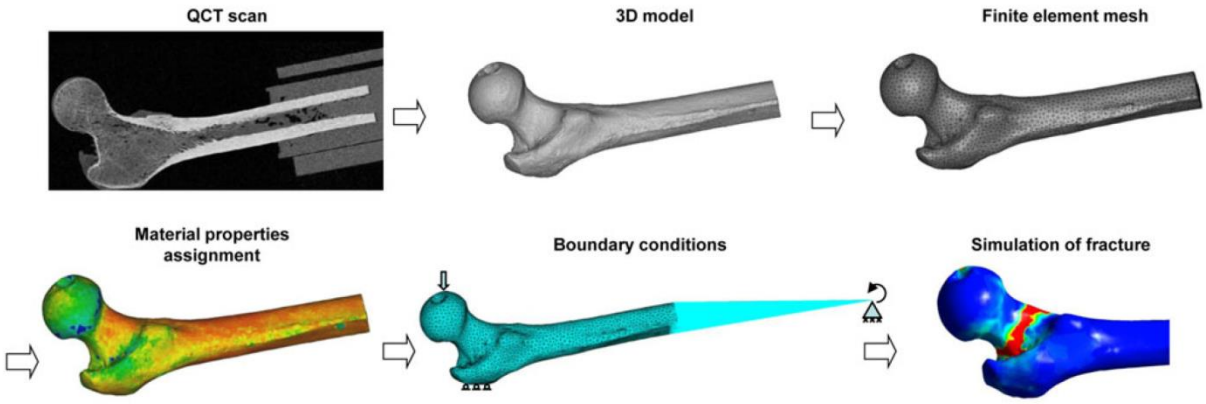

Figure 2.4. Steps of the QCT/FEA procedure to simulate the mechanical behavior of a femur in a sideways fall configuration; a 3D geometric model was reconstructed from the QCT scans of the femur. An FE model was developed from the 3D geometry of the specimen. The model was then run in the FE method to simulate the femoral fracture in a fall on the hip event. The steps of the FE modeling included discretizing the model into finite elements, assigning material properties to the elements, applying BCs representing a sideways fall on the hip loading configuration, and simulating the fracture event [54].

The QCT/FEA models of the 104 experimentally fractured femora were developed from the QCT data captured before the fracture tests. Using the QCT/FEA procedure developed previously, a simulated trochanteric force versus head displacement graph was prepared for each femur; and stiffness (K, *N/mm*), strength (F_s, *N*), and fracture load (F_f, *N*) were determined from this graph.

2.5. Results

The stiffness, yield force, femoral strength, and fracture force were measured from the force-displacement data of the femora, and their correlations with bone conditions, aBMD, age, and sex were investigated. High speed video recordings and 3D models, reconstructed from the QCT data, were employed to classify the fracture location and type.

2.5.1. Results in normal, osteopenic and osteoporotic femora

Table 2.2 represents the mean, SD, and range for femoral stiffness, yield force, strength, and final fracture load for the 104 fractured femora. The force-displacement curve of a typical experiment showed a linear elastic region followed by post-yielding associated with sinking of the superior neck region into the greater trochanter (74 of the tested femora). Fatal crack initiated in tension on the inferior region of the neck or medial shaft (Figure 2.5) [69].

Table 2.2. Femoral stiffness, yield load, strength, and final fracture load for 104 femora (mean ± SD, range). (Used with permission of Mayo Foundation for Medical Education and Research, all rights reserved).

Description	**Normal**	**Osteopenic**	**Osteoporotic**	**All**
Stiffness (*N/mm*)	2259 ± 504, [1269-3197]	1653 ± 437, [973-2611]	1107 ± 281, [502-1751]	1622 ± 613, [502-3197]
Strength (*N*)	6367 ± 1581, [3604-10013]	3850 ± 974, [2021-5771]	2180 ± 639, [927-3485]	3942 ± 1990, [927-10013]
Yield load (*N*)	3552 ± 991, [1887-6004]	2321 ± 671, [1022-3960]	1258 ± 544, [256-2582]	2276 ± 1172, [256-6004]
Fracture load (*N*)	5284 ± 1709, [2522-9668]	2835 ± 854, [1528-4354]	1574 ± 472, [729-2754]	3057 ± 1832, [729-9668]

One-way analysis of variance (ANOVA) with Tukey-Kramer post hoc analysis showed that stiffness, yield load, strength, and fracture load were significantly lower for osteoporotic femora compared to normal and osteopenic femora ($p < 0.0001$) , as well as for osteopenic femora compared to normal specimens ($p < 0.0001$) (Figure 2.6).

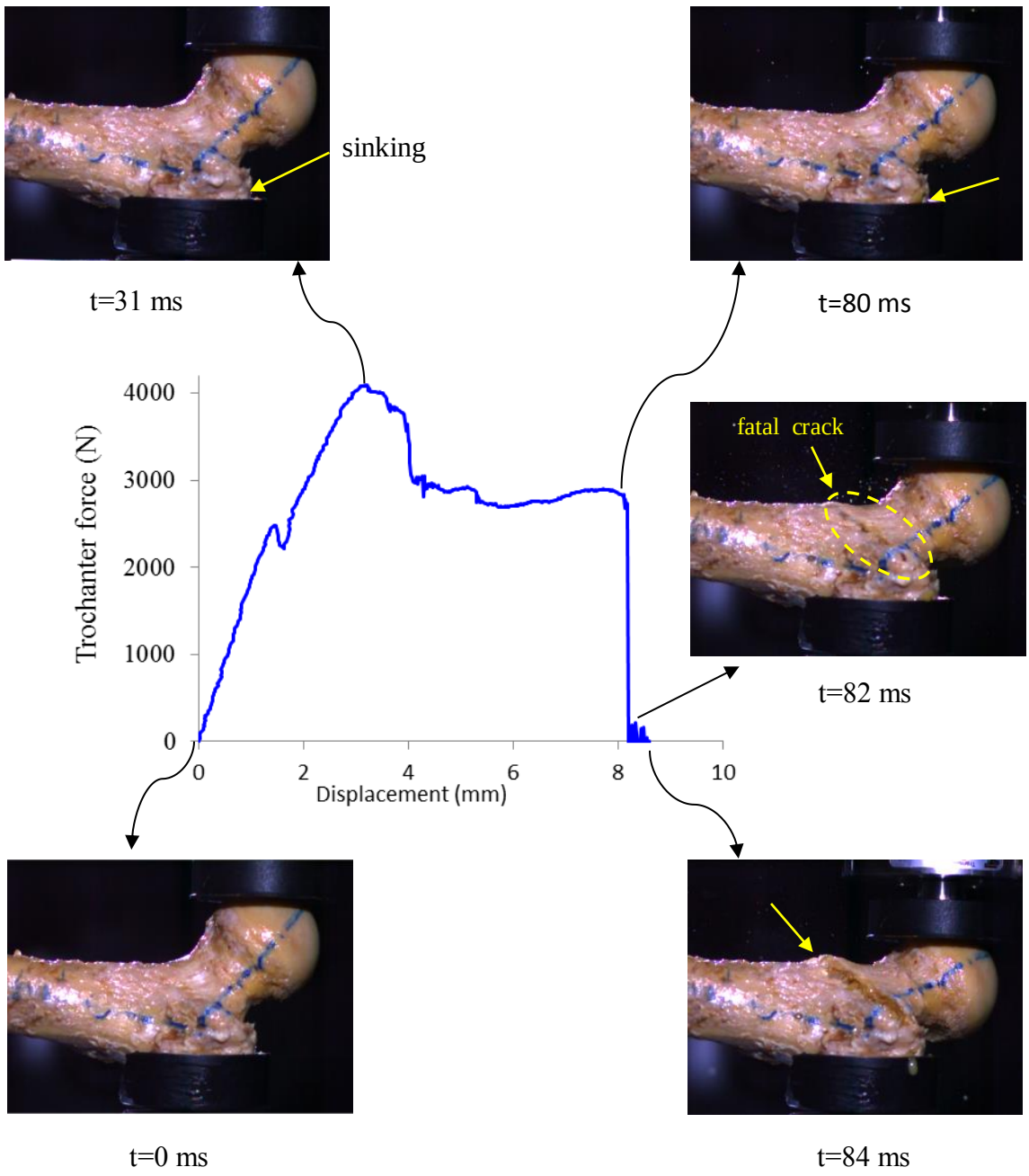

Figure 2.5. Force-displacement curve of a typical experiment; the graph showed a linear elastic region followed by post-yielding associated with sinking of the superior neck region into greater trochanter. Fatal crack initiated in tension on the inferior region of the neck or medial shaft. (Used with permission of Mayo Foundation for Medical Education and Research, all rights reserved).

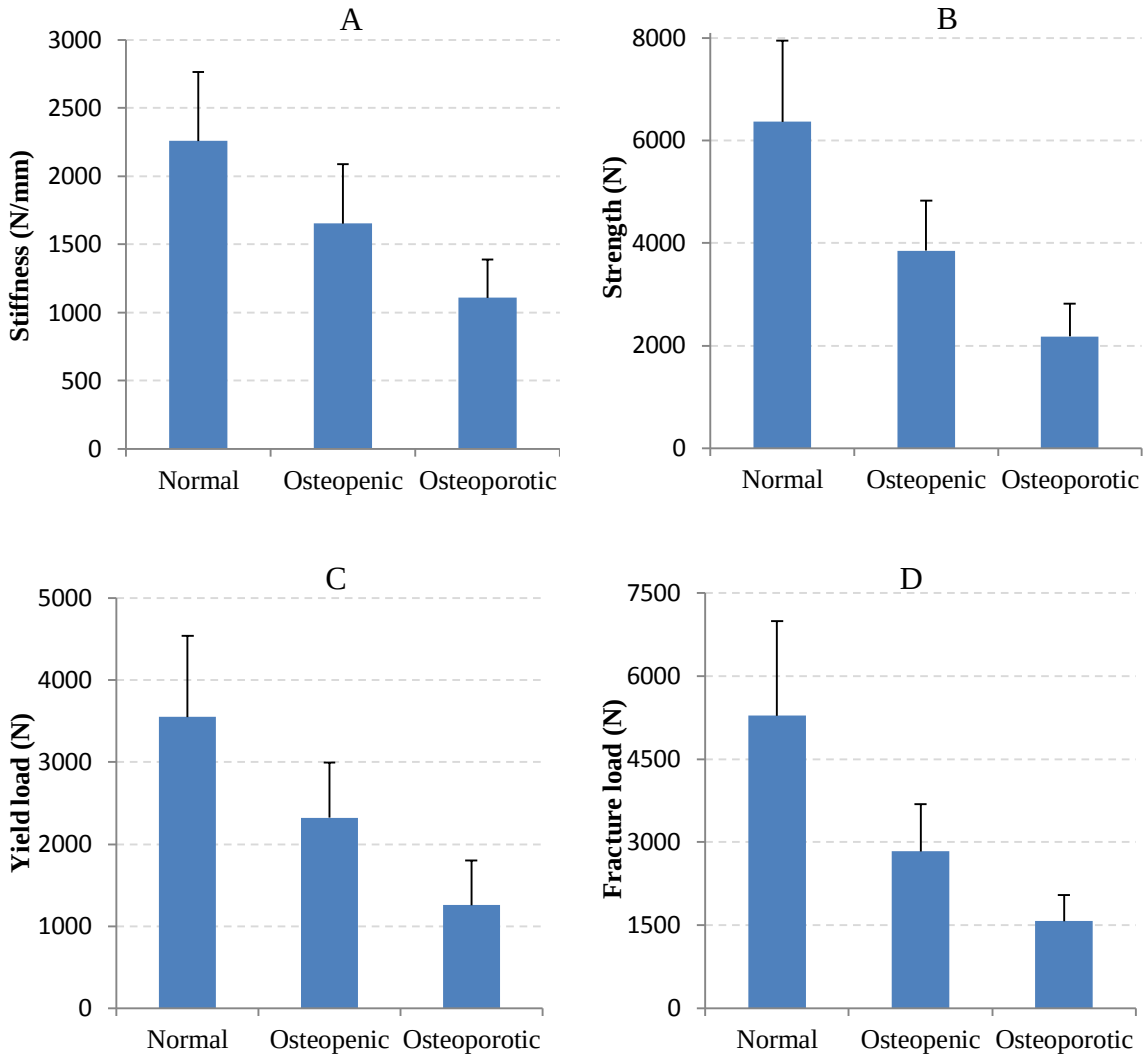

Figure 2.6. One-way ANOVA revealed that the femoral stiffness (A), yield load (B), strength (C), and fracture load (D) were significantly smaller for osteoporotic femora compared to normal and osteopenic femora, as well as for osteopenic specimens compared to normal femora. (Used with permission of Mayo Foundation for Medical Education and Research, all rights reserved).

2.5.2. Correlation with aBMD, Sex, and Age

Two sample t-tests showed that male femora had significantly higher neck aBMD, stiffness, and strength compared to female femora (aBMD: 0.897 ± 0.199 g/cm^2 versus 0.725 ± 0.191 g/cm^2, stiffness: 1996 ± 590 N/mm versus 1440 ± 543 N/mm, strength: 5394 ± 1819 N versus 3252 ± 1683 N) ($p < 0.0001$). Regression analysis showed strong correlations between femoral strength and neck aBMD with $R^2 = 0.79$, but the correlation between femoral stiffness

and neck aBMD was moderate with $R^2 = 0.57$ ($p < 0.0001$). Figure 2.7 shows the distribution of strength and stiffness versus neck aBMD, comparing male, female, and all femora. As illustrated, at the same aBMD value, the female femora tended to have smaller stiffness and strength values compared to the male ones. Femoral strength and stiffness values showed weak correlation to age with $R^2 = 0.4$ and $R^2 = 0.49$, respectively.

2.5.3. Correlation with geometric parameters

A 3D geometric model was reconstructed for each femur from the QCT scans captured before the fracture tests. Geometric parameters of the proximal femur, which involved the femoral neck axis length (L, *mm*), mean femoral neck diameter (D, *mm*), and neck/shaft angle (α ^{o}), were measured for each femur from their 3D model (Figure 2.8). The results are presented in Table 2.3. Regression analysis showed very weak correlations between femoral strength and geometric parameters with $R^2 = 0.12$ for femoral neck axis length, $R^2 = 0.16$ for femoral neck diameter, and $R^2 = 0.01$ for neck/shaft angle.

2.5.4. Fracture types

Table 2.4 shows the fracture types and their associated aBMD and fracture loads. One-way ANOVA showed that femora with introcanteric fracture had significantly lower neck aBMD than femora with pertrochanteric ($p = 0.023$) and transcervical fractures ($p = 0.0072$). Pursuant to this observation, femora with pertrochanteric and transcervical fractures had significantly higher fracture forces compared with those with introchanteric fractures with p-values of 0.023 and 0.0072, respectively [69].

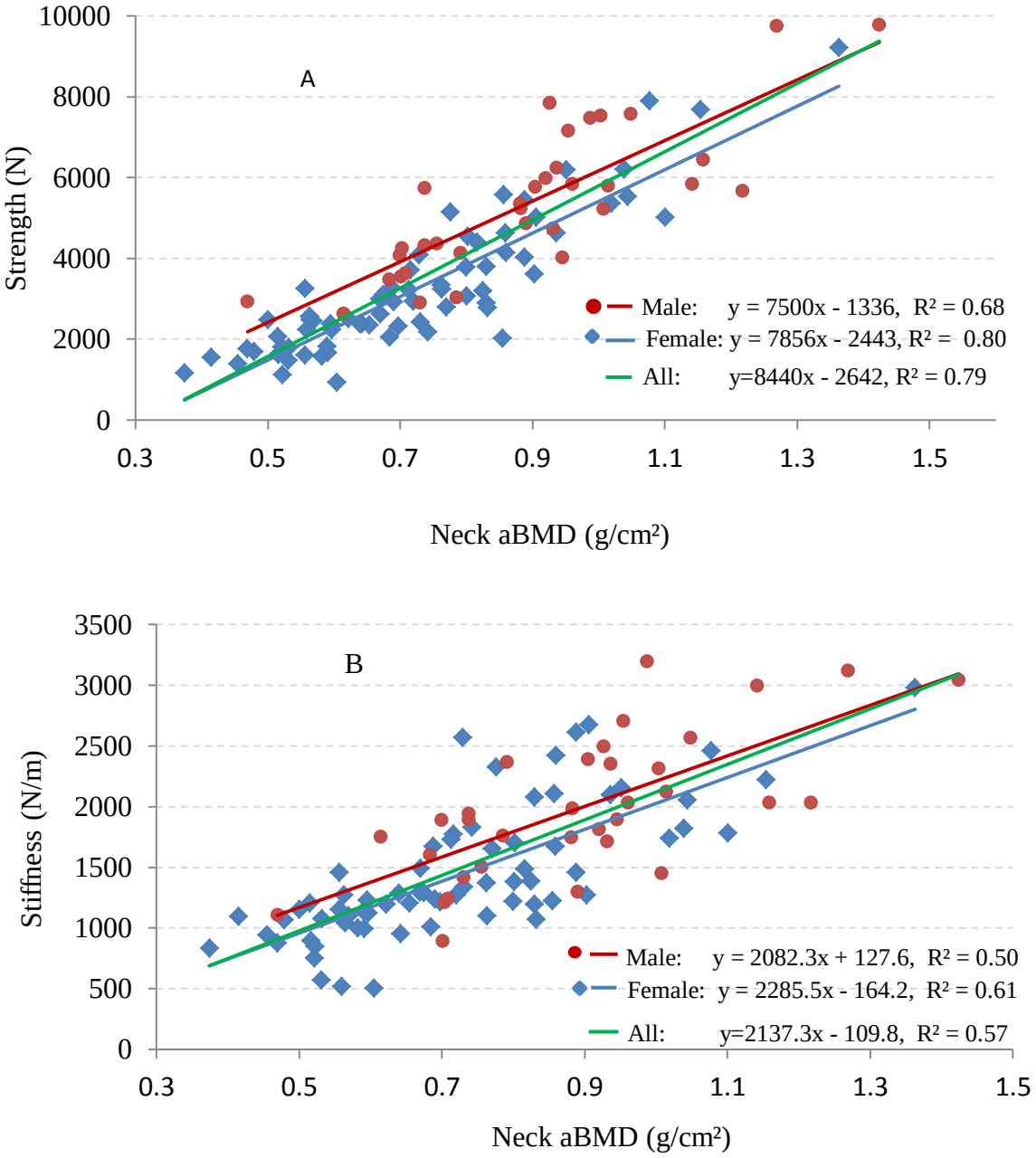

Figure 2.7. Distribution of (A) strength and (B) stiffness vs. neck aBMD for male, female, and all femora; at the same aBMD value, the female femora had smaller stiffness and strength values compared to the male ones. (Used with permission of Mayo Foundation for Medical Education and Research, all rights reserved).

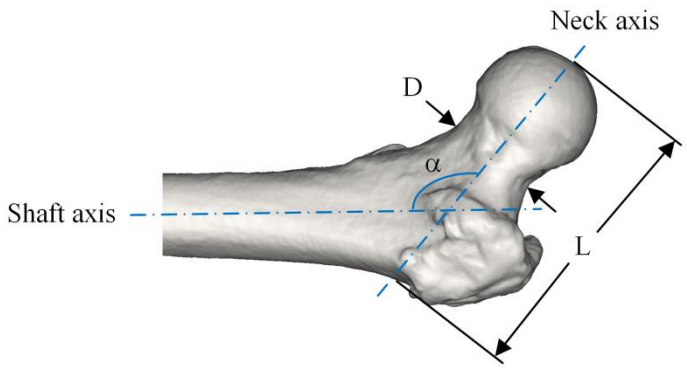

Figure 2.8. Geometric parameters of the proximal femur, including femoral neck axis length (L, *mm*), femoral neck diameter (D, *mm*), and neck/shaft angle (α°), measured from the 3D geometric model of each femur [69].

Table 2.3. Geometric parameters (mean ± SD, range) of the proximal femora. (Used with permission of Mayo Foundation for Medical Education and Research, all rights reserved).

Gender	L (mm)	D (mm)	α °
Female	96 ± 6, [81-111]	30 ± 2, [25-37]	134 ± 5, [124-147]
Male	107 ± 7, [93-124]	35 ± 2, [31-40]	133 ± 4, [126-143]
All	100 ± 8, [81-124]	32 ± 3, [25-40]	134 ± 5, [124-147]

Table 2.4. Fracture types and their associated aBMD and fracture loads (mean ± SD, range). (Used with permission of Mayo Foundation for Medical Education and Research, all rights reserved).

Description	Subcapital	Transcervical	Introchanteric	Pertrochanteric
Number	14	44	27	19
aBMD (g/cm^2)	0.72 ± 0.21, [0.37-1.02]	0.83 ± 0.23, [0.42-1.42]	0.706 ± 0.209, [0.46-1.36]	0.81 ± 0.15, [0.56-1.14]
Fracture load (*N*)	3662 ± 1712, [1097-7066]	4430 ± 2166, [1117-9553]	2931 ± 1933, [882-8539]	4373 ± 1452, [2299-7394]

2.6. Conclusion

The objective of this chapter was to investigate the biomechanics of femoral fractures in a fall on the hip loading configuration. Femoral strength showed strong correlation with aBMD, but stiffness had a moderate correlation with aBMD. At the same aBMD, female femora showed lower stiffness and strength results than male femora. The reason could be the smaller geometry

of female femora compared to those of males or discrepancies in material properties of female and male bones. While previous studies [74] showed a strong correlation between age and bone fracture risk, in the current study, age showed a weak impact on the strength and stiffness results. A reason could be the selection of the specimens mostly from elderly people. Unexpectedly, strength and stiffness results showed very weak correlation with geometric parameters. Video recordings helped to accurately describe the properties of sinking, damage, crack initiation and propagation, as well as final separation in bone fractures. The current study showed that a combination of load, moments, high speed video recordings, and 3D geometric models, developed from QCT scans of the fractured femora, allowed for a precise characterization of femoral fractures in a fall on the hip configuration. The experimental results would be used in the next chapters as a benchmark for the QCT/FEA estimated results and for characterization of mechanical properties of the bone.

CHAPTER 3. MESH SENSITIVITY ANALYSIS AND SEGMENTATION REPRODUCIBILITY IN QCT/FEA MODELS OF THE PROXIMAL FEMUR[3]

3.1. Introduction

The QCT/FEA method uses QCT scans to obtain the femoral geometry and bone mineral distribution for FE modeling [82, 89]. The resulting models are solved using BCs that mimic loading scenarios ranging from normal physiological to impact due to falls [90]. In order to develop patient specific models, a number of assumptions are made in the QCT/FEA technique. Therefore, before clinical application, the sensitivity of the parameters used for estimating bone strength and fracture properties needs to be examined. Researchers have focused on many potential sources of errors in QCT/FEA models such as the BCs [91], the constitutive material models [84, 92, 93], and the mesh [54, 94].

The accuracy of the results and the computational efficiency of the QCT/FEA technique depend significantly on the size of the FE meshes used in the FEA models of bones. Bessho et al. [94] investigated the effect of the mesh size on the results of the QCT/FEA models of proximal femora in a stance-like loading configuration. Employing linear tetrahedral elements, they showed that mesh size of 4 mm could lead to a reduction of 9% in total strain energy compared to a mesh of 2 mm, while a mesh size of 3 mm reduced the total strain energy by only 2%. However, they did not explore the influence of the mesh size on the QCT/FEA estimated results. Dragomir-Daescu et al. [54] studied the effect of the element size on the accuracy of the results and the computational efficiency of QCT/FEA models of cadaveric femora in a sideways fall on the hip configuration. Employing quadratic tetrahedral elements, it was shown that using a coarse mesh strategy with an element size of 5 mm may lead to 35% error in stiffness results

3 The main part of 'reproducibility in QCT/FEA models of the proximal femur' in this chapter belongs to a manuscript entitled "Segmentation reproducibility in QCT/FEA models of the proximal femur", Samad Javid, Tim Rossman, Dan Dragomir-Daescu, (Submitting); used with permission of Mayo Foundation for Medical Education and Research, all rights reserved.

compared to a fine mesh strategy with an element size of 2 mm. They proposed a smart mesh strategy with various element sizes at different parts of the femoral model to reduce the computational time while enhancing the accuracy of the results. A limitation of this study, however, was the small sample size. In the current study, a relatively large sample size of 24 proximal femora was employed to determine a robust and computationally efficient mesh size for the QCT/FEA modeling of proximal femora in a fall on the hip loading configuration.

Another source of error, not yet studied in detail, is variability introduced by the user during the segmentation of CT scans to reconstruct the femoral 3D geometry. Accurate 3D femur geometry is an important input to the QCT/FEA method and the variation from the segmentation process could lead to significant errors in QCT/FEA predictions. During segmentation, different tools are used to obtain a precise outer contour of the bone in each slice of the CT scans. Variation in selecting the femoral cortical boundary can arise based on the user's ability to delineate bone tissue from soft tissue, the user's experience level with the software, and simple errors that can occur when repetitively interpreting potentially hundreds of CT slices. Since the QCT/FEA method used here is based on continuum solid mechanics, errors in the geometric representation can directly contribute to errors in the prediction of forces and stresses.

Segmentation can also affect the mechanical properties of the elements near the surface of the bone. The mechanical properties, such as Young's modulus and yield strain, are functions of the averaged Hounsfield Unit (HU) values of the voxels enclosed by the finite element [67]. If the elements on the surface of the bone erroneously include external neighbor voxels with lower HU values, these elements will be affected by partial volume effects. Thus the mechanical properties of the cortical bone in these elements will be reduced.

In general, the user induced variation in a measurement system might be broken down to two categories: 1)repeatability and 2)reproducibility. Repeatability is the variation in measurements taken by one user on the same or replicate specimens, while reproducibility is the variation induced by different users measuring the same or replicate items [95]. Luo et al. [96] investigated the repeatability and reproducibility of the results of a DXA-based patient-specific FE procedure developed for assessing hip fracture risk. They found that inconsistent positioning of the femora during scanning and manual segmentation of the projected femur contour caused significant variability in the estimated fracture risk. Lee et al. [97] studied the repeatability and reproducibility of the results of a volumetric bone mineral density (vBMD) measurement method developed to determine local distribution and quality of bone mineral in the proximal humerus. They showed that their method could measure vBMD in a reproducible manner with a less than 2% reproducibility and repeatability error.

However, the user induced variation in the results of the QCT/FEA estimated femoral strength and stiffness due to segmentation was not yet quantified. The current study aimed to assess the quality and accuracy of QCT/FEA, in terms of reproducibility analysis, which is of interest in clinical applications. To the best of the author's knowledge, such an extensive study, with a large sample size, had not been investigated and published in the literature.

3.2. Mesh Sensitivity Analysis

The 3D models of 24 human cadaveric proximal femora (eight male and 18 female donors; age: 71 ± 15 yr; eight normal, eight osteopenic and eight osteoporotic based on neck aBMD) were obtained by segmenting QCT images of the femora. Each model was meshed with quadratic tetrahedral elements having different element sizes for a total of four mesh refinements. The maximum edge lengths of elements at different areas of the femoral models

(Figure 3.1) are reported in Table 3.1. The size of the elements was increased by a factor of 1.2 from the surface of the models toward their centers [54].

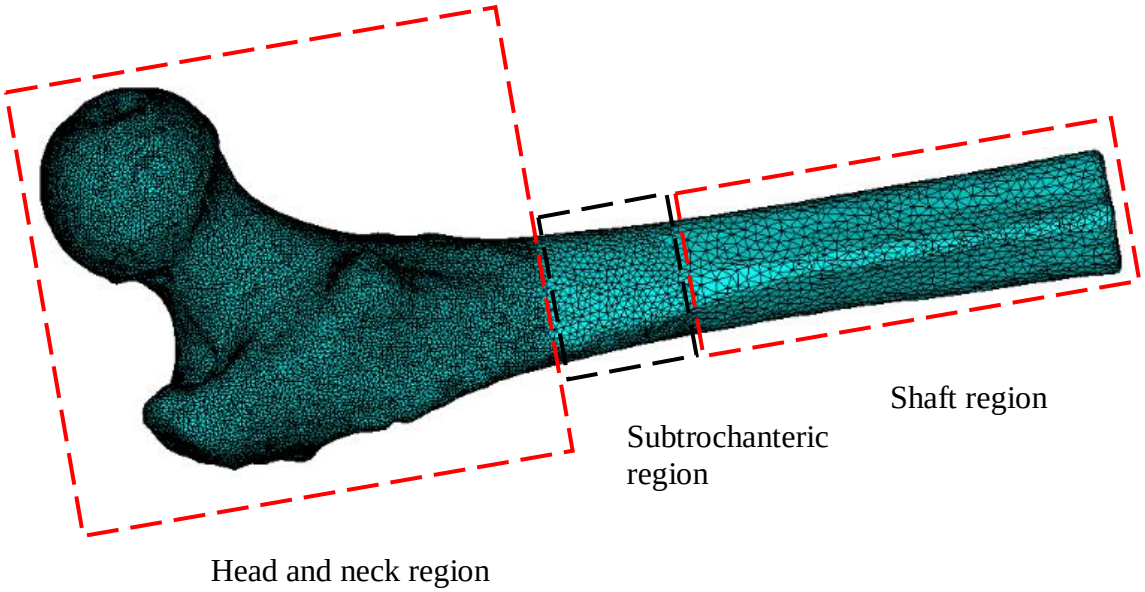

Figure 3.1. A femoral model meshed with tetrahedrons with different element edge length at head and neck region, subtrochanteric region, and shaft region. (Used with permission of Mayo Foundation for Medical Education and Research, all rights reserved).

Table 3.1. Maximum element edge length (*mm*) in different models. (Used with permission of Mayo Foundation for Medical Education and Research, all rights reserved).

Model No.	**Femoral head and neck region**	**Subtrochanteric region**	**Femoral shaft region**
1	2	3	5
2	1.5	2.5	4
3	1	2	3
4	0.5	1	2

The BCs mimicking a fall on the hip configuration were applied to all the support areas in the models (Figure 3.2). First, a rotation point was connected to the distal end using stiff beam elements. The model was made free to rotate around a horizontal x-axis passing through the rotation point. Secondly, a node group on the surface of the greater trochanter was constrained in the vertical translation degree of freedom. Finally, a force BC was applied in 100 *N* increments

distributed over a set of nodes located in a small area of the femoral head surface in the vertical direction (*z*-axis) [54, 67].

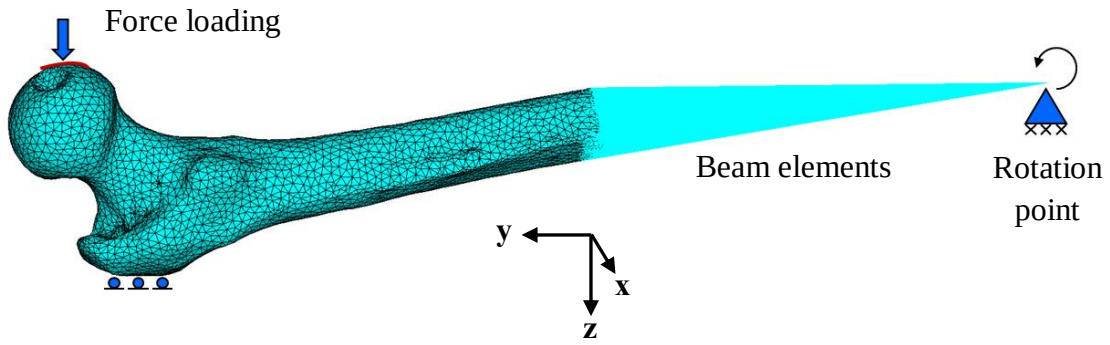

Figure 3.2. Simulation of the BCs applied at the support areas of a femoral model in a fall on the hip loading configuration. (Used with permission of Mayo Foundation for Medical Education and Research, all rights reserved).

After applying density-based material properties to the elements, ANSYS (ANSYS Inc., Canonsburg, PA, USA) was used to simulate a fall on the hip. For each model, vertical trochanteric reaction force and vertical head displacement were obtained on the BC application areas. The force-displacement graph was processed to calculate the femoral stiffness from the slope of the linear regression line passing through six force-displacement points at 0.1 *mm* increments. The predicted stiffness results converged for each femur. The model with the smallest element size (model 4) was used as a baseline and its stiffness was compared with the stiffness of the other three coarser meshes (models 1, 2, and 3). Errors of less than 5% were assumed acceptable.

At the tissue level, mechanical responses, such as strain and stress distributions, in models 1, 2, and 3 were compared to those of model 4 for each femur. In the current study, von Mises strain and stress were employed but the term von Mises was omitted for simplicity. The strain and stress values of all elements were recorded at the end of each loading step. Then, volume-averaged (VA) strain and stress values in the proximal part of the model (head and neck

region in Figure 3.1), experiencing the majority of deformation under loading, were determined using the following equations [98]:

$$\varepsilon_{VA} = \frac{\int \varepsilon dV}{\int dV}$$
$$\sigma_{VA} = \frac{\int \sigma dV}{\int dV} \quad (1)$$

The distribution and the maximum values of strain and stress were also used to explore the effect of the mesh size on the local tissue level response of models, while the VA values were employed to determine the effect of the mesh size on the global tissue level response.

3.2.1. Results and discussions of mesh sensitivity analysis

The average number of elements, the average elapsed time to complete the simulations, and the stiffness errors in models with different mesh sizes are reported in Table 3.2. The average number of elements in model 2 was around 586000, almost double that of model 1. Model 3 had an average number of elements of 1.2 million, almost a quarter of the number of elements in model 4. The maximum stiffness errors in models 1, 2 and 3 compared to model 4 was 6% (for three femora), 4% (for five femora) and 3% (for eight femora), respectively. The average stiffness error was 2% for models 1 and 2, and 1% for model 3. On the average, it took 3 hours to run a simulation using model 4 for six displacement load step of 0.1 *mm* by employing 10 cores of 2.67 *GHz* on a high speed high performance computing (HPC) cluster. In the same scenario, the elapsed time for models 3, 2, and 1 was: 55, 38, and 15 minutes, respectively.

Table 3.2. Number of elements, elapsed time to complete the simulations, and stiffness errors compared to target models (model 4). (Used with permission of Mayo Foundation for Medical Education and Research, all rights reserved).

	Model No.			
	1	**2**	**3**	**4**
Average number of elements	273179	586060	1173813	4797395
Average CPU time (min.)	15	38	55	179
Stiffness error (%) mean ± SD, range	2 ± 2, [0-6]	2 ± 1, [0-4]	1 ± 1, [0-3]	

At the tissue level, Figure 3.3 shows the strain and stress contour plots for models 1, 2, 3, and 4 of a typical femur at head displacement of 0.6 *mm*. For this femur, the stiffness error in models 1, 2, and 3, compared to the model 4, was 6%, 4%, and 2%, respectively. While all the meshes led to the same VA strain of 0.003, the VA stress was 0.86, 0.88, 0.9, and 0.91 *MPa* for meshes 1, 2, 3, and 4, respectively. The VA stress errors in models 1, 2, and 3, compared to model 4, was 5%, 3%, and 1%, respectively. This correlated well with the stiffness errors in the corresponding models. However, the maximum local stress and strain values varied considerably on different models, showing no similar pattern with the global responses. Comparing the VA to maximum stress values, one could conclude that local responses were not a good predictor to find the optimal mesh size. For this purpose, global responses at tissue and apparent levels should be employed.

Based on the global responses, model 2 satisfied the acceptable error level and showed that there was no need for reduction in the mesh size. Model 2 was also computationally efficient taking, on the average, about 38 minutes to compute the stiffness results. The current study highlighted the effect of the mesh size on the results and computational efficiency of the QCT/FEA model of the proximal femur. Too few elements could lead to erroneous predictions,

while too many elements would lead to an expensive computational effort. Thus an optimal mesh distribution needs to be used, especially if such methods are used in the clinic.

3.3. Segmentation Reproducibility in QCT/FEA Modeling

Five trained users[4] were instructed to produce 3D models from QCT scans and run FEA simulations to estimate femoral strength and stiffness. Each user followed a set of internally-developed standard operation procedures (SOPs) to reconstruct the 3D models from QCT scans of 45 fresh-frozen human cadaveric femora. The characteristics of the femoral set are shown in Table 3.3. Each set of 45 models segmented by a user is called a test series thereafter. The femoral models were then meshed with quadratic tetrahedral finite elements using smart mesh strategy as explained in the study of Dragomir-Daescu et al. [54]. To assign material properties, the geometry was divided into 42 equal material groups based on the density range.

The following empirical equation was employed to calculate the isotropic elastic modulus (*E, MPa*) of material groups as a function of their ash density (ρ_{ash}, g/cm^3) (Morgan et al. [66]).

$$E = 14664\rho_{ash}^{1.49} \tag{2}$$

This relationship was also used previously in QCT/FEA models of the proximal femur by Verhulp et al. [99]. To simulate bone damage due to loading, the following equation was employed to calculate the yield strain (ε_y) in each material group [54].

$$\varepsilon_y = 8.1 \times 10^{-3}\rho_{ash}^{-1.42} \tag{3}$$

A constant Poisson ratio of 0.3 was assigned to all material groups. After applying the BCs (Figure 3.2), the models were solved in ANSYS APDL software (ANSYS, Canonsburg, PA).

[4] Rachel C. Entwistle, Christina Salas, Viorel Hodis, Ian Gerstel, and Vishwas Mathur

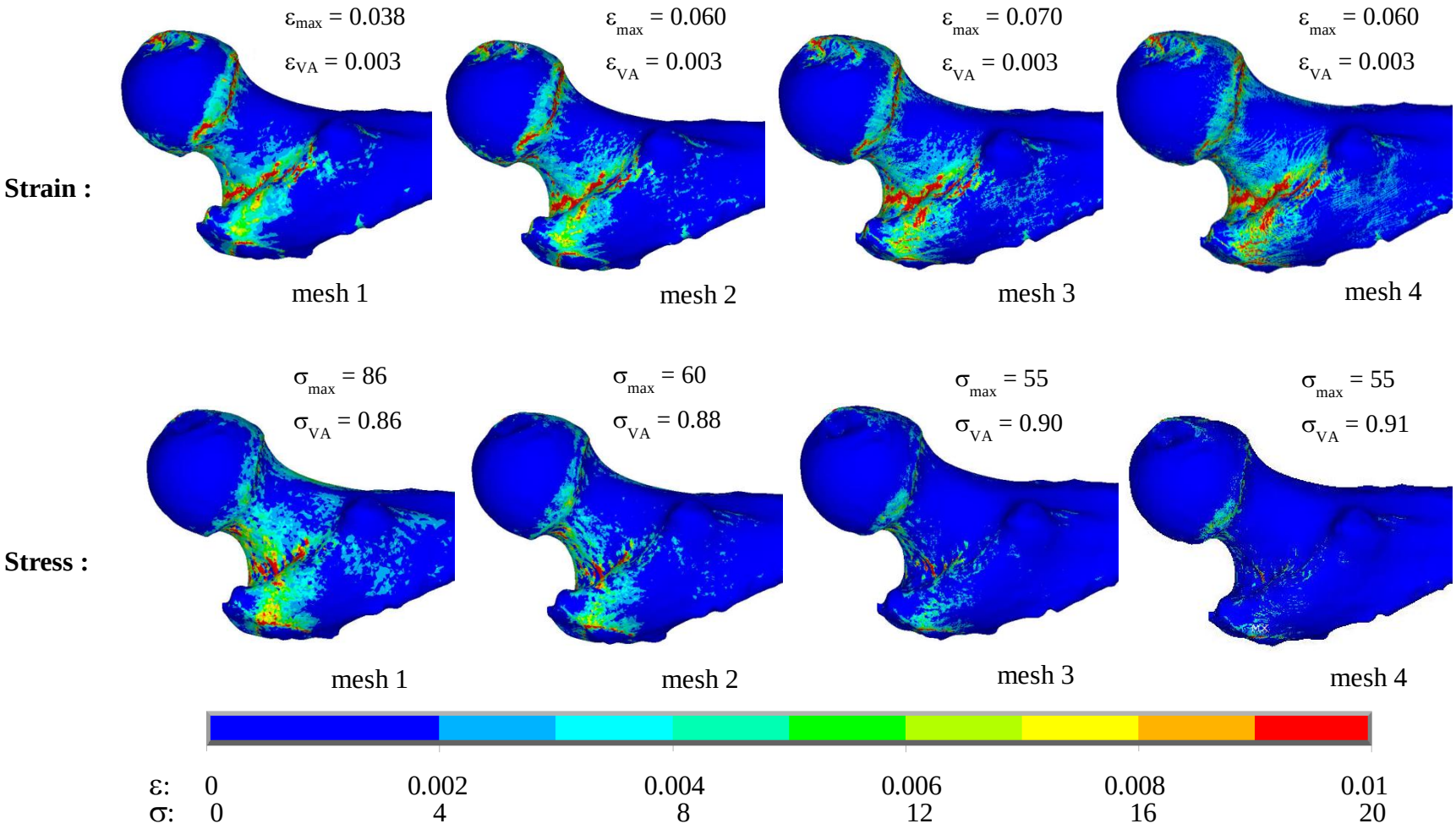

Figure 3.3. Strain (ε) and stress (σ, *MPa*) contour plots in a typical femoral model with different mesh size; the maximum (max) and the volume averaged (VA) quantities are shown for each model. (Used with permission of Mayo Foundation for Medical Education and Research, all rights reserved).

Table 3.3. Characteristics of the 45 cadaveric femora used in the current study. (Used with permission of Mayo Foundation for Medical Education and Research, all rights reserved).

	Females	**Males**	**All**
Number (*n*)	27	18	45
Age (*year*) mean ± SD, range	66 ± 13, [37-97]	68 ± 16, [34-91]	67 ± 14, [34-97]
Neck aBMD (g/cm^2) mean ± SD, range	0.751 ± 0.186, [0.374-1.154]	0.885 ± 0.225, [0.469-1.424]	0.804 ± 0.210, [0.374-1.424]
Bone condition based on neck aBMD (*n*)	normal:5 osteopenic: 10 osteoporotic: 12	normal: 10 osteopenic: 5 osteoporotic: 3	normal: 15 osteopenic: 15 osteoporotic: 15

Using in-house APDL scripts, at the end of each load step, the Young's moduli of elements with the von Mises strain (ε_{VM}) greater than their corresponding yield strain (ε_y), calculated from Eq. 3, were automatically reduced to the insignificant value of 0.01 *MPa*, to account for material damage. The simulation continued until the head displacement in the vertical direction reached 3.4 *mm*, which was the average vertical displacement of the femoral head at the onset of fracture as measured during the mechanical fracture testing. The force on the trochanter at the simulated fracture point was defined as the femoral strength (F_S, *N*). The stiffness of each femoral model (K, *N/mm*) was calculated as the slope of the initial linear portion of the trochanteric force versus displacement curve. All the steps in the FEA simulation, from pre-processing to post processing, were implemented automatically in ANSYS APDL scripts to eliminate user variability.

For each femur, the model with the largest volume was compared to the model with the smallest volume using 3-matic (Materialise, Leuven, Belgium), and the mean distance between the two reconstructed femoral surfaces was computed. The mean distance from each analysis, for all 45 femora, were then imported into MATLAB (MathWorks, Natick, MA, USA) to compute the mean and the SD of the mean distances. Finally, the distribution of the mean distances was compared to the average QCT voxel size (~0.5 mm). In addition, because the differences

between the points on the surface of two user models could be positive or negative, the root mean square (RMS) values were calculated as a measure of the average model surface differences.

The two users whose QCT/FEA strength and stiffness estimations had the largest difference with each other were selected. Linear regression analysis was used to correlate the strength and stiffness estimations by one of these two users with the results of the other one, respectively. The 95% confidence interval was determined for the regression lines between the QCT/FEA estimations of these two users. Moreover, Bland-Altman mean-difference plots were used to investigate the difference between the estimations of these two users.

For each femur, the SD and the mean value were calculated for five strength and stiffness values. The coefficient of variation (CV) was then determined for strength and stiffness results of each femur as the ratio of the SD to the mean value. The CV was used as a representative metric to measure the dispersion of the QCT/FEA results. The similarity among the strength and stiffness values obtained using models in five test series was tested by employing a multi-rater concordance correlation analysis (M-CCA) [100, 101].

3.4. Results of Segmentation Reproducibility Study

3.4.1. Geometry comparison

The mean and the range of the mean, the SD, and the root mean square (RMS) error of the distances for the largest and the smallest model segmentation volumes, for the entire cohort of 45 femora, are presented in Table 3.4. The mean distance was less than or equal to the size of the voxel for all femora. The largest RMS error was only slightly greater than the voxel size at about 0.53 *mm*. Figure 3.4 shows the histogram of the RMS error of the distances for all 45 femoral geometry comparisons. As depicted, the RMS error was slightly larger than a voxel size

for only three femora. This, confirmed that the geometry of the two largest and smallest segmented models of each femur were very similar.

Table 3.4. The mean and range of the mean, the SD, and the RMS error of distances (*mm*) from geometry comparison of the two extreme models of each femur in the set of 45 femora. (Used with permission of Mayo Foundation for Medical Education and Research, all rights reserved).

Mean	**SD**	**RMS**
0.168, [0.088-0.445]	0.149, [0.050-0.361]	0.218, [0.106-0.526]

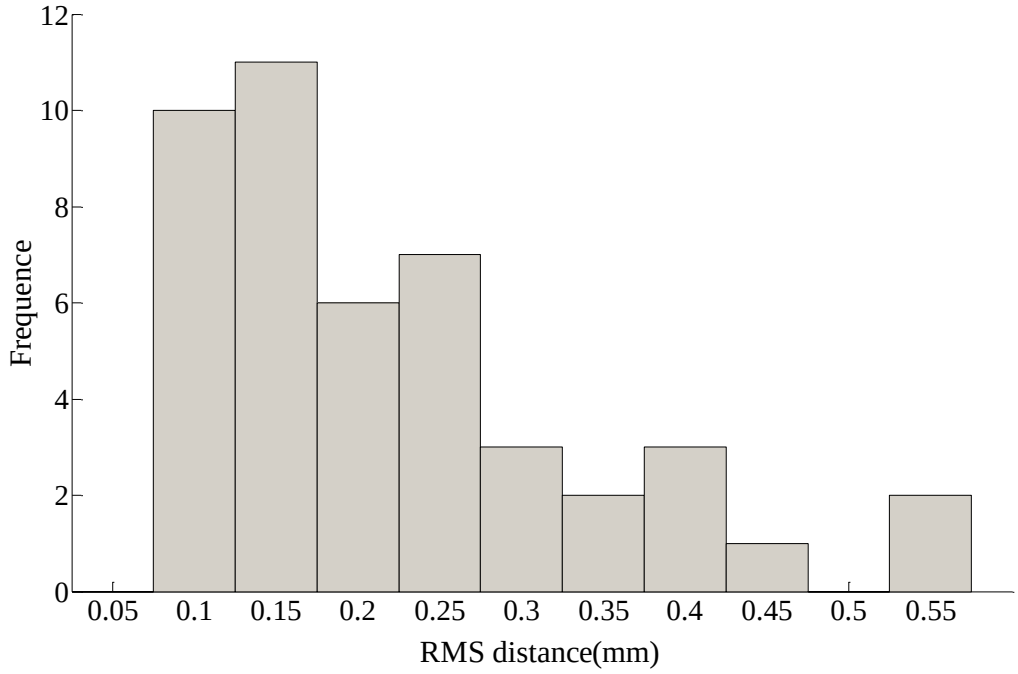

Figure 3.4. The distribution of the RMS error of the distances from the geometry comparison between two extreme models of each femur in the set of 45 femora. (Used with permission of Mayo Foundation for Medical Education and Research, all rights reserved).

3.4.2. Strength and stiffness comparison

Figure 3.5 shows the graphs of the QCT/FEA strength and stiffness estimations for test series one and three whose QCT/FEA predictions had the largest difference with each other compared to the others. The correlation equations between the strength (S, *KN*) and stiffness (K, *KN/mm*) results of these two test series were as follows:

$$S_3 = 1.021S_1 - 0.018 \quad (4)$$

$$K_3 = 1.041K_1 - 0.044 \quad (5)$$

with the coefficient of determination (R^2) 0.995 and 0.996 for the strength and stiffness regressions, respectively.

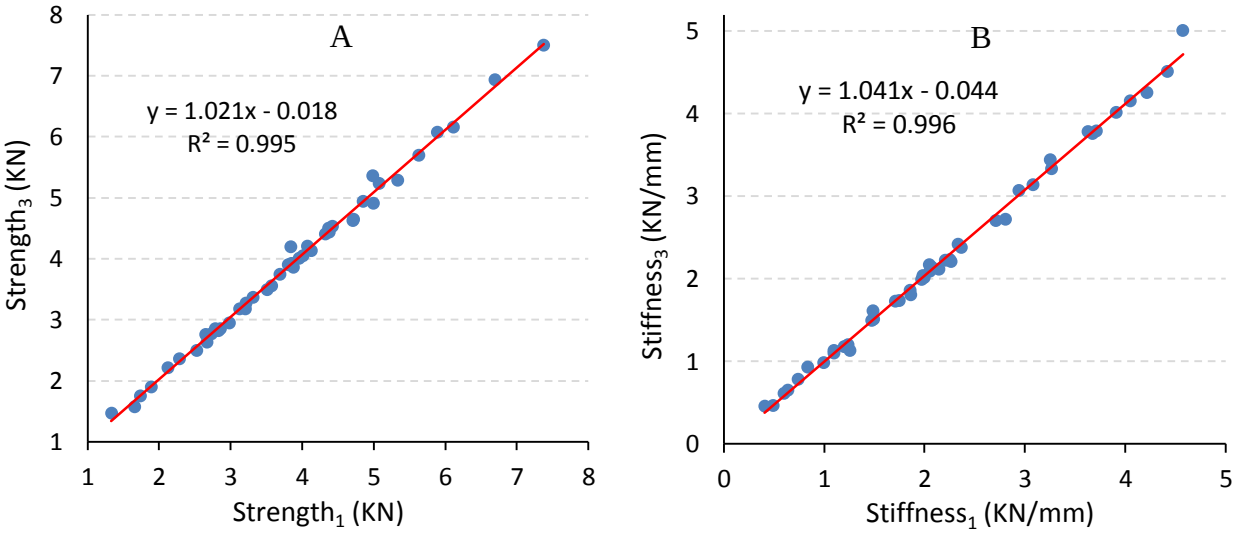

Figure 3.5. The QCT strength (A) and stiffness (B) estimations for the 45 femora models in test series one and three whose QCT/FEA estimations had the largest difference to each other. (Used with permission of Mayo Foundation for Medical Education and Research, all rights reserved).

In the aforementioned strength and stiffness correlation equations (Eq. 4 and 5), the slope is statistically significant ($p < 0.001$ paired t-test), while the intercept is not significant ($p = 0.676$ for strength and $p = 0.189$ for stiffness). For the strength correlation equation, the 95% confidence interval for the slope was 0.998-1.043 and for the intercept was -0.504 to 0.069, while the first and the second intervals included the expected value of 1.0 for the slope and 0.0 for the intercept, respectively. Similarly, for the stiffness correlation equation, the 95% confidence interval for the slope was 0.999-1.021 and for the intercept was -0.095 to 0.005, the first and the second intervals including the expected value of 1.0 for the slope and 0.0 for the intercept, respectively.

Figure 3.6 shows the Bland-Altman mean-difference plots for the strength and stiffness estimations for test series one and three. As depicted, the 95% confidence interval of the mean-

difference values for both strength and stiffness included zero. Figure 3.7 shows the graphs of the CV versus the mean value of the QCT/FEA strength and stiffness estimations for each of the 45 femora.

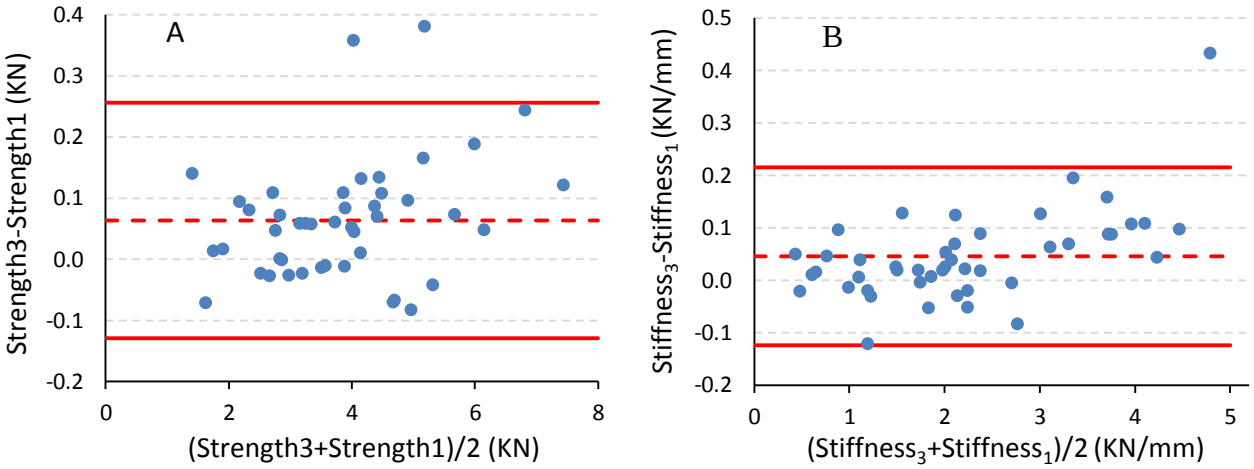

Figure 3.6 Bland-Altman mean-difference plots for strength (A) and stiffness (B) estimations for the 45 femoral models in test series one and three; the dash lines show the mean values and the solid lines show the confidence intervals. (Used with permission of Mayo Foundation for Medical Education and Research, all rights reserved).

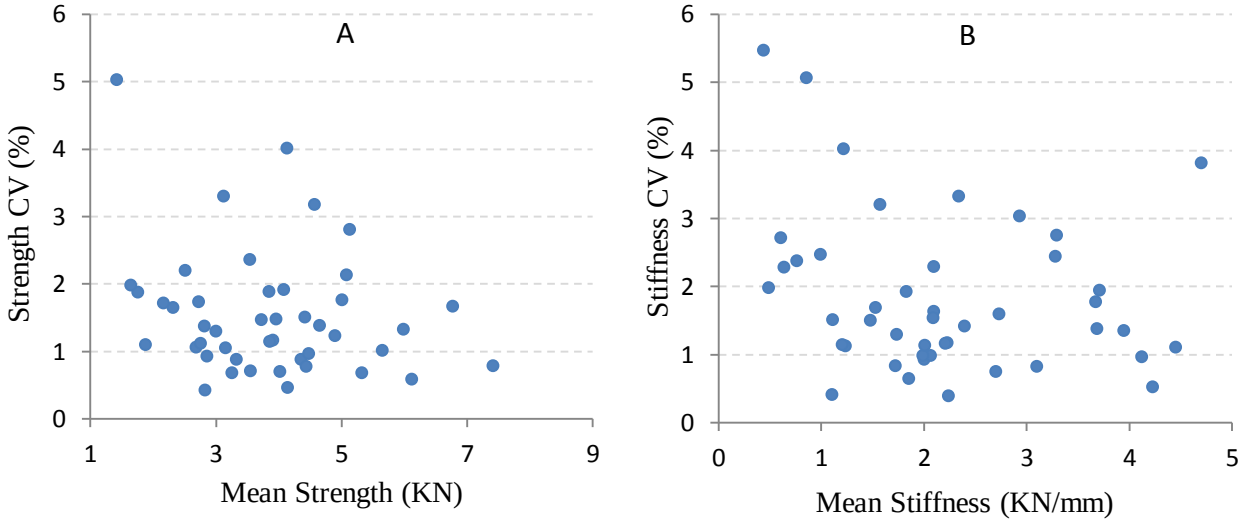

Figure 3.7. The CV (%) versus the mean value for the QCT/FEA strength (A) and stiffness (B) estimations for the 45 femora. (Used with permission of Mayo Foundation for Medical Education and Research, all rights reserved).

Figure 3.8 shows the histogram of the CV of the QCT/FEA strength and stiffness estimations for all 45 femora. As depicted, the vast majority of femora had a CV of less than 2% for both strength (40 femora) and stiffness (36 femora) estimations. Finally, using the M-CCA, a concordance correlation coefficient (CCC) value of 0.995 was obtained for the strength results. This value was greater than 0.99, a level that indicates almost complete agreement [102]. A similar level of agreement was obtained for the stiffness estimations where the multi-observer CCC was 0.998.

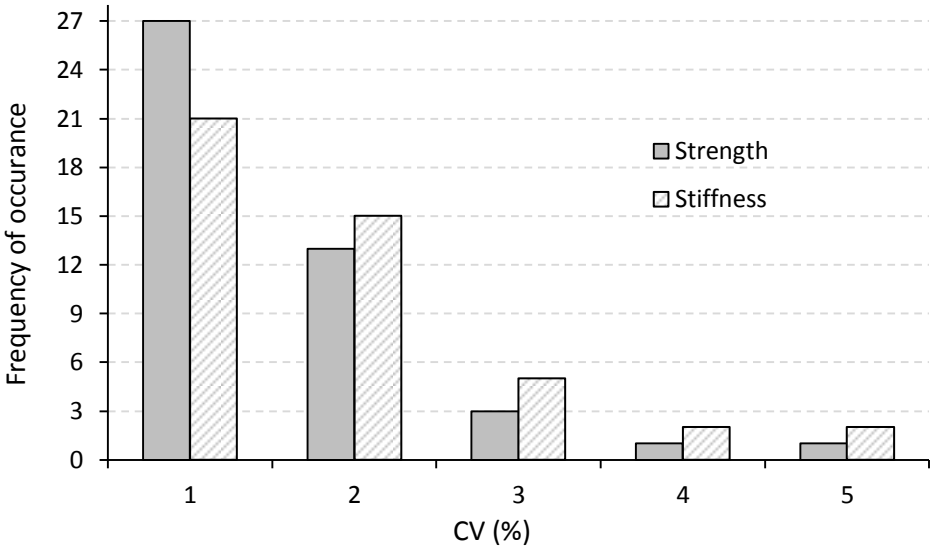

Figure 3.8. Histogram of the CV of the QCT/FEA strength and stiffness estimations for the 45 femora. (Used with permission of Mayo Foundation for Medical Education and Research, all rights reserved).

As the deformation of the bone originates from the interaction of mechanical parameters at the tissue level, stresses and strains of one of the femora were determined and compared for its FE models in five test series. Figure 3.9 shows the variation of FE estimated trochanteric force versus head displacement for five FE models of the femur. Among all, the five models of this femur had the largest variation in strength results. The largest and the smallest stiffness values were 3336 and 3140 *N/mm*, respectively, corresponding to a variation of 6%. The greatest and

the least strength results were 4710 and 4330 *N*, respectively, leading to a difference of 8%. All five models of the femur had almost the same strain and stress distributions in both elastic and post-yield regions.

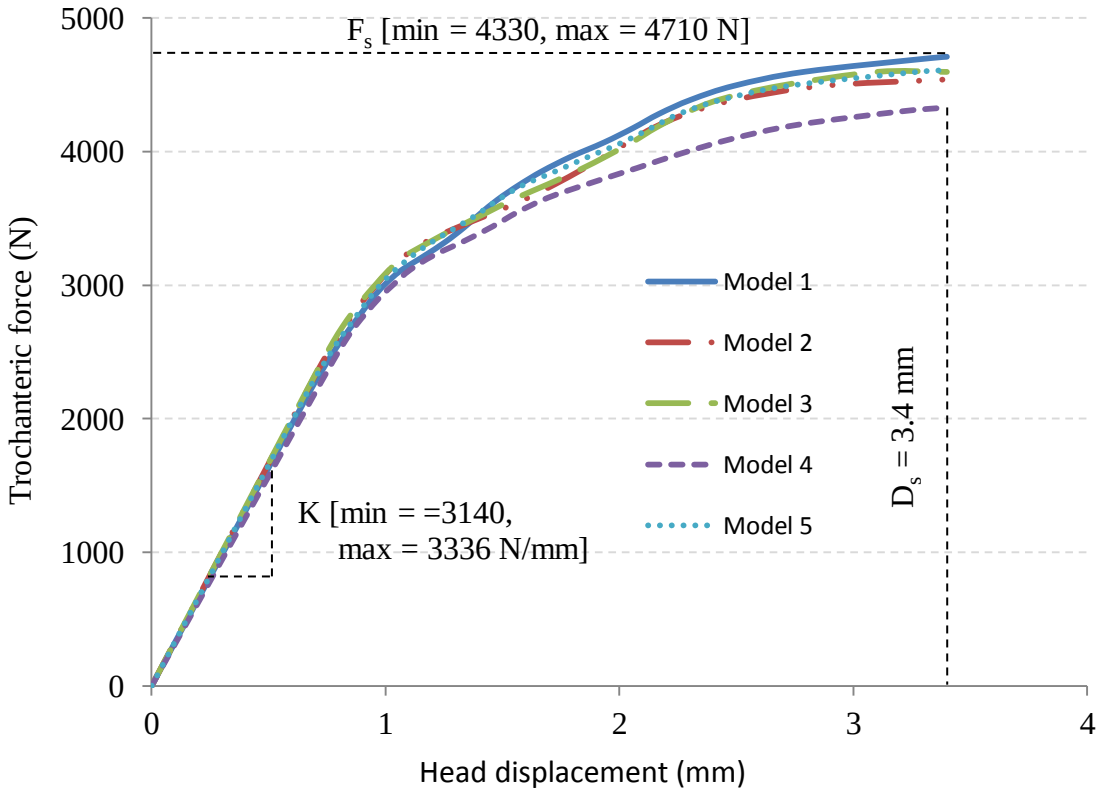

Figure 3.9. FE trochanteric force versus head displacement for five models of a femur; the largest and the smallest stiffness (K) values had a variation of 6%. The highest and the least strength (F_s) results contributed to a difference of 8%. (Used with permission of Mayo Foundation for Medical Education and Research, all rights reserved).

Typical strain and stress contour plots of the femur in the elastic region (displacement of 0.6 *mm*) and at the onset of fracture (displacement 3.4 *mm*) are presented in Figure 3.10.

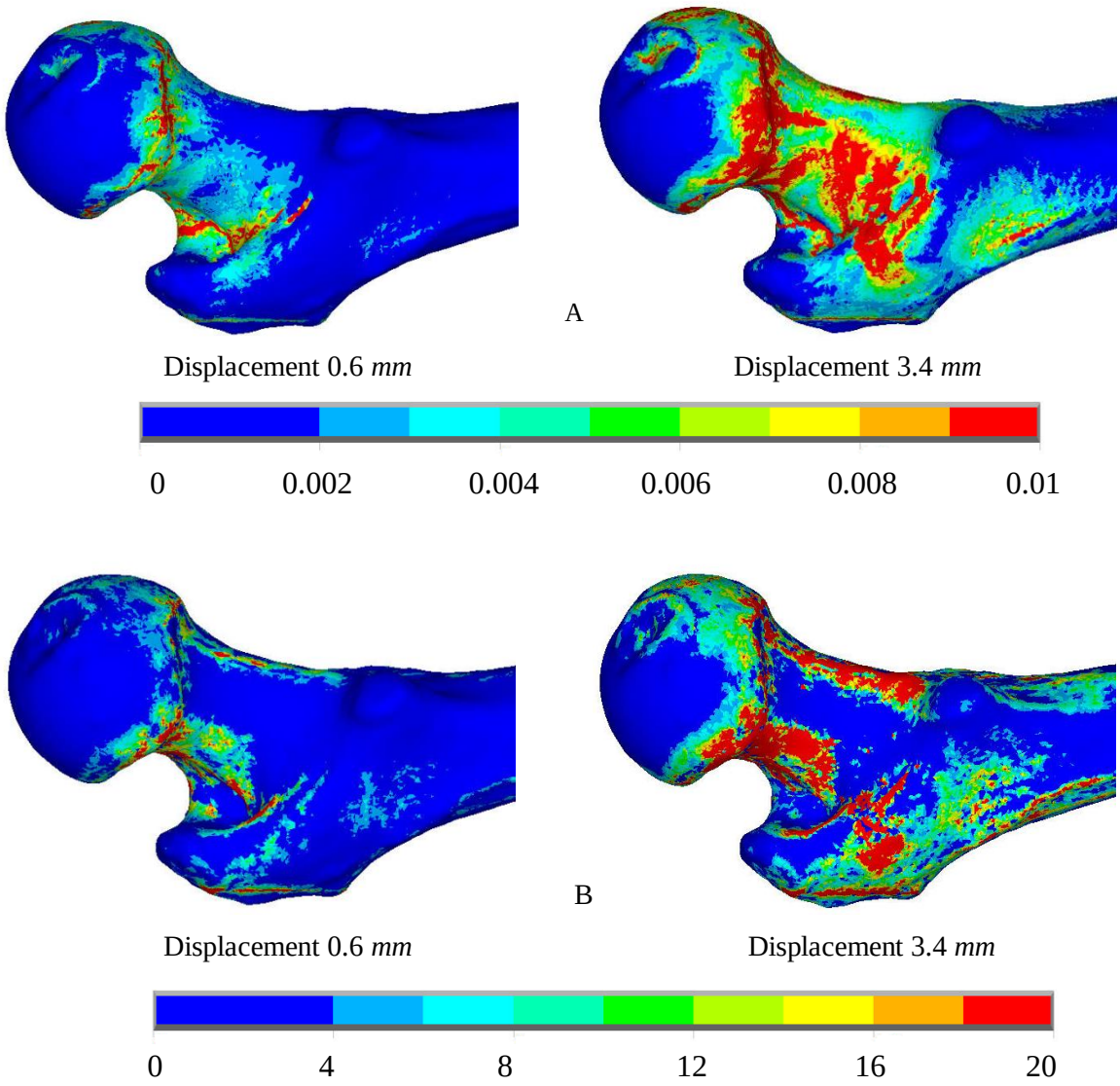

Figure 3.10. (A) Strain and (B) stress (*MPa*) contour plots in the elastic region (displacement 0.6 *mm*) and at the onset of fracture (displacement 3.4 *mm*) along the femoral model. (Used with permission of Mayo Foundation for Medical Education and Research, all rights reserved).

The VA and the maximum local strain and stress values for the FE models of the femur in its elastic region are presented in Table 3.5. The ratio of the VA stress to the VA strain, called VA modulus, was determined for each model and presented in this Table. The models 3 and 4 had, respectively, the largest and the smallest VA moduli, correlating well with stiffness values of these models. However, similar trend was not observed for the local maximum strain and stress values.

Table 3.5. Different mechanical parameters of the femoral models in the elastic region (displacement 0.6 *mm*). (Used with permission of Mayo Foundation for Medical Education and Research, all rights reserved).

	Model 1	**Model 2**	**Model 3**	**Model 4**	**Model 5**
VA strain	0.0025	0.0023	0.0023	0.0028	0.0025
VA stress (MPa)	2.3	2.21	2.2	2.44	2.43
VA modulus (MPa)	920	961	974	871	972
Local maximum strain	0.0783	0.1822	0.0661	0.0622	0.5120
Local maximum stress (MPa)	63	85	90	72	282

Table 3.6 shows the VA and the maximum strain and stress results of the femur at the onset of fracture for the five models. All the models had almost the same VA strain value. This, confirmed that they underwent the same deformation up to fracture, as expected. Models 1 and 4 had the greatest and the smallest VA stress values, being in agreement with the strength values of these models.

Table 3.6. VA, and maximum local strain and stress values of the five models of the femur at the onset of fracture (displacement 3.4 *mm*). (Used with permission of Mayo Foundation for Medical Education and Research, all rights reserved).

	Model 1	**Model 2**	**Model 3**	**Model 4**	**Model 5**
VA strain	0.012	0.012	0.012	0.013	0.012
VA stress (MPa)	7.61	7.53	7.48	7.39	7.50
Local maximum strain	3.302	3.703	3.051	3.781	3.005
Local maximum stress (MPa)	417	413	409	368	461

3.5. Discussions and Conclusion

The geometry comparison between the largest and smallest models of each femur showed very small differences between the models segmented by different users. The mean, SD, and RMS values for all 45 femora were less than or around the QCT scan's voxel size which is an acceptable error for segmentation. The results from the current study also showed small

variability in QCT/FEA predictions of femoral strength and stiffness attributed to users. The strength and stiffness estimations for the two test series whose QCT/FEA predictions had the largest difference with each other showed very strong correlations, with the coefficient of determinations greater than 0.994 for both strength and stiffness results. In both correlation equations, the slope was significant and very close to one and the intercept was insignificant and very close to zero. For the strength and stiffness estimations of these two test series, the 95% confidence interval of the Bland-Altman mean-difference plots involved zero difference. These analyses showed that the QCT/FEA estimations for these two test series were not statistically different.

The CV was used as a standard measure to investigate the discrepancy between the QCT/FEA estimations of the five test series. For none of the femora, the CV was higher than 5% for strength and stiffness results. The vast majority of the femora had a CV of less than 2% for both strength (40 femora) and stiffness (36 femora) estimations. Only one femur had a CV of 5% for strength and two femora had a CV of 5% for stiffness. This confirmed very small differences between the results of different test series. These relatively small differences were observed for a large femoral sample with a wide range of ages and aBMD which was representative of both sexes. Moreover, the multi-observer CCC obtained for the five test series was greater than 0.99 for both strength and stiffness estimations, a level that indicates almost complete agreement [102].

The current study has several limitations. First, it did not attempt to extend the user reconstructions to clinical scans. Such scans include surrounding soft tissues that make it more difficult to segment the bone. Different users may be more prone to interpret the boundary of the bone differently and produce more variability in the resulting 3D reconstruction. Secondly, the

current study did not investigate user repeatability due to the significant effort that would have been required for each user to repeatedly segment the set of 45 femora and run the FE analyses. Such a process took approximately 12 hours to complete for each bone per user and was not attainable due to resource availability. However, with the consistency observed from the independent results obtained for the five test series, one can conclude that this is a minor limitation of the current study. Finally, the current study was limited to one loading condition and failure criteria. More investigation needs to be done to extend the findings of the current study to other bone modeling methods including other loading conditions, failure criteria, etc.

In conclusion, the results of the current study showed that the QCT/FEA method was reproducible for the set of 45 femora which is a large enough sample size to claim that the method can be clinically employed for assessing bone fracture risk, provided the procedures are carefully followed by trained users for the whole process. The promising results of the current study also implied that the repeatability of the process can be likely guaranteed as the errors producing from one user, in the repetition of the QCT/FEA method, is lower compared to the ones from different users.

CHAPTER 4. OPTIMIZED EVALUATION OF INHOMOGENIOUS ELASTIC PROPERTIES OF FEMALE FEMORA USING INVERSE FINITE ELEMENT ANALYSIS

4.1. Introduction

Finite element analysis has been employed in orthopedic biomechanics for understanding the bone's interaction with implants [102-105], for assessing bone fracture healing [106], and for evaluating bone fracture risk [63, 107, 108]. A major challenge in subject-specific FEA of human bones is the evaluation of heterogeneous material properties in bone models [63] as the materials have vital impacts on the simulation results [62, 83, 84]. The elastic material properties are usually estimated from the CT scans using empirical equations from bone density [89, 109].

The majority of the bone density-elasticity relations have been derived from biomechanical tests on bone coupons from different anatomical sites [64-66, 93, 110]. Three of these relationships have been widely used in subject-specific FEA of human bones to estimate the mechanical characteristics of bones under different loading scenarios [54, 99, 111, 112]. Keller [64] conducted compression tests on cubic cortical and trabecular specimens from human vertebrae and femora and showed good correlation for both linear and power models between compressive elastic modulus and bone density.

Keyak et al. [65] performed compression tests on trabecular coupons acquired from cadaveric proximal tibiae and found power relationships between orthogonal elastic moduli and bone ash density. Morgan et al. [66] measured the compressive elastic moduli and apparent densities of trabecular coupons extracted from human vertebra, proximal tibia, and femur. Due to the very complex and inhomogeneous structure of bones, small coupons separated from the whole bone cannot represent the global response of intact bones [67]. Mechanical properties of

bones are also location dependent and different from one to the others [66], so that the coupon tests may erroneously predict the actual structural responses of bones. Furthermore, biomechanical tests for extracting bone density-elasticity relationships have usually been conducted under simple uniaxial loadings, while the majority of bone fractures, such as those resulted from a fall on the hip, happen under complex loadings involving a combination of tensile, compression, shear, bending and torsional loadings. Materially, the complex structure of bones cannot be characterized using simple uniaxial monotonic ramps [113, 114].

Performing experiments on the whole femur, on the other hand, provides better insight of what bones structurally respond to different loading conditions. This type of characterization, however, requires computational efforts as well. Several studies have tried to determine the bone density-elastic modulus relationships using inverse computational-experimental methods [67, 68, 115]. Huang et al. [115] performed an inverse computational study to estimate the elastic modulus of cortical bone specimens directly from the CT number. The obtained results are, however, only applicable to the CT machine they employed, because each CT scanner model has its own standard HU values. Cong et al. [67] (DOE, Mayo Clinic) identified the coefficients of the bone density-elastic modulus relationships by minimizing an error function between the FEA estimated and experimental stiffness of proximal femora in a fall on the hip configuration. They used a power law and a sigmoid function to express the relationship between the density and the elastic modulus of the bone. However, they used simplified BCs in bone FE models. Their study was also limited to a small sample size. Eberle et al. [68] used an inverse numerical-experimental study on cadaveric femora in a stance-like configuration to determine the coefficients of a power law between bone density and elastic modulus. They showed that subject-specific density-elastic modulus relationships lead to more accurate FE models of human femora compared to cohort-

specific relations. However, they did not cross-validate their proposed density-elasticity relation on another set of femora. Another limitation of this study was the small sample size. Moreover, their study was limited to a stance-like loading configuration, and they did not validate their findings against other loading scenarios, such as a sideways fall configuration as the most common loading pattern in hip fractures.

Despite great efforts in the material characterization of bones, reported density-elasticity relationships are significantly different from each other [67, 93], and there is still a need for an accurate and robust relation to determine the distribution of the elastic properties through the bone FE models. The previously proposed bone density-elasticity relationships have also been aimed at the mechanical properties of the whole population regardless of their sex, while female bones are more vulnerable to osteoporosis and hip fractures [116]. The overall objective of the current study was to identify the density-elastic modulus relationships of female bones under a complex load scenario. To this end, the mechanical behavior of female femora in a sideways fall was measured by mechanical experiments and was simulated by FE modeling (chapter 2).

4.2. Proposed Elastic Constitutive Equations for Bones

Unlike engineered materials and some of biological tissues, bone has a complex, inhomogeneous elastic property distribution. Carter and Hayes [110] performed mechanical tests on bone specimens and proposed a power law that relates the elastic modulus of the bone to its density as follows:

$$E = a\rho_{ash}^{b} \tag{1}$$

where a and b are material constant values. This mathematical relationship has been employed widely in the literature of bone FE modeling. Helgason et al. [93] summarized the majority of available bone density-elasticity relationships (Table 4.1). Additionally, Cong et al. [67]

introduced a new relationship in the form of a sigmoid function between the bone density and its elastic modulus as follows:

$$E = ce^{de^{f\rho_{ash}}} \quad (2)$$

where *c*, *d* and *f* are material constant values. In the current study both the power law and the sigmoid function were used separately in femoral FE models to map bone ash density (ρ_{ash}, g/cm^3) to its elastic modulus (E, *MPa*). The material constants were identified using an inverse computational-experimental approach and their performances on the bone response were investigated.

4.3. Inverse Finite Element Analysis

Characterization of mechanical properties of materials has been as a challenging problem in engineering. In cases where material specimens have simple standard geometries, derivation of specimen characteristics is easy; different mechanical test methods can be implemented and the responses of the samples are simply compared with well-suited mathematical equations to obtain the constants of the equations. However, in many complex engineering problems characterization of mechanical properties of different materials is not straight forward to fit only a mathematical equation on the experimental data.

Table 4.1. Bone density-elasticity relationships extracted from mechanical tests. (Revised from [93]).

Study	Site	Type of bone	Densitometric Measure	ρ-range (g/cm^3)	E (GPa)
Carter & Hayes [110]	Pooled	Cortical and trabecular	ρ_{app}	0.07–2.0	$E = 3.79\dot{\varepsilon}^{0.06}\rho_{app}^{3}$
Lotz et al. [118]	Human femoral neck	Trabecular	ρ_{app}	0.18–0.95[RFG]	$E = 1.31\rho_{app}^{1.40}$
Lotz et al. [119]	Human femoral metaphysis	Cortical	ρ_{app}	1.20–1.85[RFG]	$E = -13.43 + 14.261\rho_{app}$
Snyder & Schneider [120]	Human tibial diaphysis	Cortical	ρ_{app}	1.748–1.952	$E = 3.891\rho_{app}^{2.39}$
Hodgskinson & Currey [121]	Pooled	Trabecular	P_{dry}	0.094–1.111	$E = 3.98\rho_{dry}^{1.78}$
Linde et al. [122][b]	Human proximal tibia	Trabecular	ρ_{app}	0.273[c]	$E = 4.778\rho_{app}^{1.99}$
Anderson et al. [123]	Human proximal tibia	Trabecular	P_{dry}	0.14–0.48[RFG]	$E = 3.890\rho_{dry}^{2.0}$
Dalstra et al. [124]	Human pelvis	Trabecular	ρ_{app}	0.109–0.959	$E = 2.0173\rho_{app}^{2.46}$
Keller [64]	Human spine	Trabecular	ρ_{ash}	0.028–0.182	$E = 1.89\rho_{ash}^{1.92}$
Keller [64]	Human femur	Cortical and trabecular	ρ_{ash}	0.092–1.221	$E = 10.5\rho_{ash}^{2.29}$
Keller [64]	Pooled	Cortical and trabecular	ρ_{ash}	0.028–1.221	$E = 10.5\rho_{ash}^{2.57}$
Keyak et al. [65]	Human proximal tibia	Trabecular	ρ_{ash}	0.06–0.27	$E = 33.9\rho_{ash}^{2.20}$
Goulet et al. [125]	Pooled	Trabecular	*BV/TV*	0.06–0.36	$E = 6.310(\frac{BV}{TV})^{2.10}$
Keaveny et al. [126]	Human lumbar spine	Trabecular	ρ_{app}	0.09–0.28	$E = -0.058 + 1.540\rho_{app}$
Li & Aspden [127]	Human femoral head	Trabecular	ρ_{app}	0.14–1.4	$E = -0.0094 + 0.573\rho_{app}$
Ouyang et al. [128]	Human vertebra	Trabecular	ρ_{app}	0.46–0.71	$E = 2.3828\dot{\varepsilon}^{0.07}\rho_{app}^{1.88}$
Kopperdahl & Keaveny [129]	Human vertebra	Trabecular	ρ_{app}	0.11–0.27	$E = -0.08 + 2.1\rho_{app}$
Ciarelli et al. [130]	Human proximal femur	Trabecular	*BV/TV*	0.15–0.40[RFG]	$E = 7.541\left(\frac{BV}{TV}\right) - 0.637$
Morgan et al. [66]	Human vertebrae	Trabecular	ρ_{app}	0.11–0. 35	$E = 4.730\rho_{app}^{1.56}$
Morgan et al. [66]	Human proximal tibia	Trabecular	ρ_{app}	0.09–0. 41	$E = 15.52\rho_{app}^{1.93}$
Morgan et al. [66]	Greater trochanter	Trabecular	ρ_{app}	0.14–0. 28	$E = 15.01\rho_{app}^{2.18}$
Morgan et al. [66]	Human femoral neck	Trabecular	ρ_{app}	0.26–0. 75	$E = 6.850\rho_{app}^{1.49}$
Morgan et al. [66]	Pooled	Trabecular	ρ_{app}	0.09–0. 75	$E = 8.920\rho_{app}^{1.83}$
Kaneko et al. [131]	Human distal femur	Trabecular	ρ_{ash}	0.102–0.331	$E = 10.88\rho_{ash}^{1.61}$

[a] Pearson correlation coefficient as reported in the original work.
[b] Reported results are for cylindrical specimens with diameter of 7.5 mm and a height of 7.5 mm.
[c] Average value. Range not reported, RGF = read from graph.

Complex geometries, as well as a variety of loading scenarios, make it more complex to determine the constant parameters of the materials. The situation is even worse for biological tissues; due to time dependency and inhomogeneity in material properties across the tissue. For example, femoral bone material characterization is a challenge due to a complicated anatomical structure and material anisotropy. Inverse finite element method (IFEM) is a very effective tool that makes use of numerical methods to derive mechanical properties of such materials [117].

In an IFEM, the optimization algorithms are coupled with an FE code while the material properties are unknown. The initial values of the material properties are passed to the FE procedure and the results are compared with the experiments as reference data. Then, optimization procedures search for new sets of material properties to obtain the best possible fit. This process is repeated several times to minimize the error function between the FE estimated and the experimental results, and to eventually find the optimal values of parameters of interest.

Generally, the process of IFEM is computationally expensive, as it usually involves many iterations, and similar to different numerical techniques it may face convergence issues. The accuracy of the results is also dictated by the assumptions in the FE formulations and optimization algorithms. Although many strategies are implemented in the optimization algorithms to find the global optimal response of the problem, if the objective function is complex, including several local extrema, it will be difficult to find the global optimum of respective values. Therefore, the number of unknowns should be reduced to be as small as possible, and meaningful initial values should be chosen that relate to the physics of the problem. Another useful strategy is limiting the optimization space by applying constraints on the solutions. Without this, the process may converge to unreasonable solutions from a physical standpoint.

In the IFEM employed in the current study, the optimization algorithms were implemented through MATLAB (MathWorks, MA, USA) codes, the FE simulations were performed in ANSYS (ANSYS Inc., Canonsburg, PA, USA) through in-house ANSYS APDL codes and Tool Command Language (TCL), an interpreted scripting language, scripts. These tools were developed at Mayo Clinic.

4.4. Material Optimization Procedures

Seventy cadaveric female femora were previously tested to fracture in a fall on the hip loading configuration, and apparent stiffness values were determined from the force-displacement data. The FE models of the femora, developed from their QCT scans captured before the experiments, were used to simulate the fracture experiments (chapter 2). Apparent stiffness estimations were also computed from the subsequent simulated force-displacement data. The experimental and simulation stiffness results were then used integrated into optimization procedures to identify the unknown constants in the bone density-elasticity relationships. To this end, an objective function in the form of the RMS was defined between the experimental (K_i) and the FE predicted stiffness ($\widehat{K}_i$) values as an average error metric [67]:

$$J = \sqrt{\frac{1}{n}\sum_{i=1}^{n}\left(1-\frac{\widehat{K}_i}{K_i}\right)^2} \tag{3}$$

Where *n* is the number of femora used in the optimization process. Optimization algorithms were employed to minimize the objective function by changing the constants in the elastic modulus relationships used in the FE models in an iterative process. Consequently, the FE estimated stiffness values were compared to the experimental ones. When the change in the objective function for two consecutive iterations was less than an acceptable tolerance of 10^{-5}, the optimization process was stopped and the last set of material coefficients was reported as the

optimal constants. Figure 4.1 shows a detailed flowchart of the numerical implementation of the optimization process used in the current study.

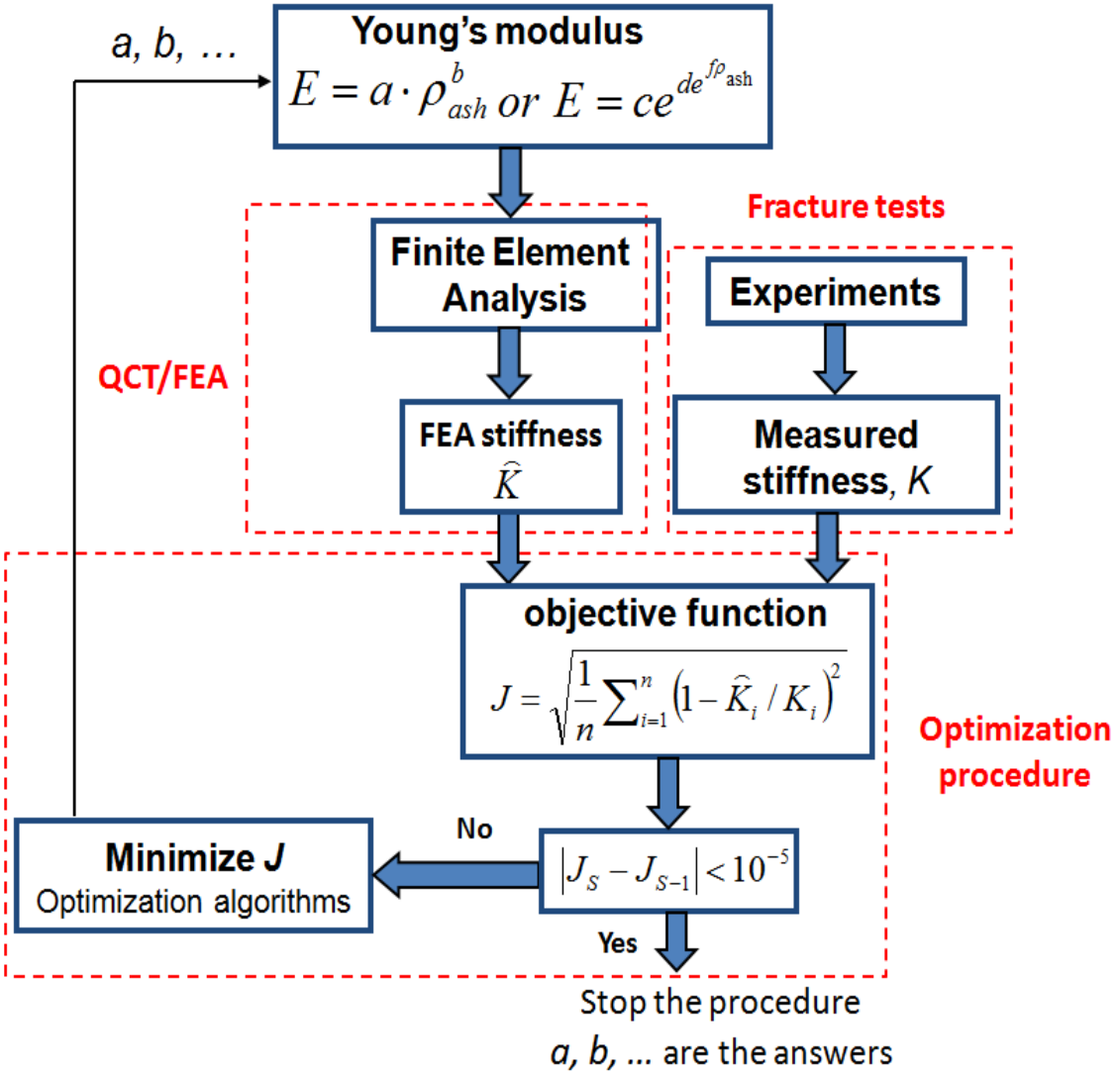

Figure 4.1. [5] Flowchart of the optimization procedure used to identify the unknown coefficients in the bone density-elasticity relationships; an objective function was formed between the experimental (K) and FE estimated stiffness ($\hat{K}$) results. Optimization algorithms were used to find the optimal coefficients in the density-elasticity relationships in FE models by minimizing the objective function *J*. When the change in the objective function *J* between two consecutive iterations was less than the acceptable tolerance10^{-5}, the optimization procedure stopped and the last set of constants was reported as the optimal coefficients. (Used with permission of Mayo Foundation for Medical Education and Research, all rights reserved).

[5] Revised from a figure prepared by Dan Dragomir-Daescu, Sean McEligot, Alex Cong, Jorn op den Buijs

The femora were randomly divided into two groups of 35 individuals. The first group, considered as training set, was used to identify the unknown coefficients in the density-elasticity relationships. The optimal elastic modulus relationships were then cross validated over the femora in the second group, called validation set.

The Downhill simplex method (Nelder-Mead simplex optimization algorithm) [132] was used for identifying the two unknown coefficients *a* and *b* in the power density-elastic modulus relationship (Eq. 1). The initial values of 8050 and 1.16 were selected for *a* and *b*, respectively, from a previous study [67].

4.4.1. Simplex search algorithm

Simplex search algorithm (SSA) is a well-known optimization method for finding a local minimum of multi-variable unconstrained functions. It is a direct search process which does not use any analytical or numerical gradient, making it suitable for problems with discrete, discontinuous, or even non-smooth functions. The method is simple to apply and is, therefore, used widely in many fields of technology and science such as medicine and chemistry.

If *n* is the length of the variables vector of an objective function, a simplex characterized by *n+1* vertices (each vertex has a length of *n*) in *n*-dimensional space is used to minimize the function [133]. For example, in 2D space, the simplex is a triangle; and in 3D space, it is a tetrahedron. A new point is generated at each step of the search. The function value at the new generated point is compared to the values of the function at the current vertices of the simplex, and the worst vertex, where the function is largest, is replaced with the new point. The process is continued and the function values at the vertices of the simplex become smaller and smaller. The size of the simplex is reduced until the desired variables are found [134]. The steps of the most common version of the algorithm are as follows [135]:

I. Reflection: calculating reflection point x_r as follows:

$$x_r = x_m + \rho(x_m - x_{n+1})$$

- Forming a new simplex by replacing the worst point x_{n+1} with the reflected point x_r and going to step II, if $f(x_1) \leq f(x_r) < f(x_n)$.

II. Expansion: computing the expansion point x_e as follows, if the reflected point is even better than the best point, i.e. $f(x_r) < f(x_1)$:

$$x_e = x_m + \chi(x_m - x_{n+1})$$

- Forming a new simplex by replacing the worst point x_{n+1} with the expanded point x_e and going to step II, If $f(x_e) < f(x_r)$, otherwise replacing the worst point x_{n+1} with the reflecting point x_r and going to step II.
- Going to the next step, if $f(x_r) \geq f(x_n)$.

III. Contraction: calculating the contraction point x_c as follows:

$$x_c = x_m + \gamma(x_m - x_{n+1})$$

- Generating a new simplex by substituting the worst point x_{n+1} with the contracted point x_c and going to step II, if $f(x_c) < f(x_{n+1})$, otherwise going to the next step.

IV. Shrinkage: replacing all the points except the best point with the following points and going to step II:

$$x_i = x_1 + \sigma(x_i - x_1) \qquad i = 2, 3, \cdots, n+1$$

where ρ, χ, γ, and σ are the reflection, expansion, contraction, and shrinkage coefficients, respectively, with the following default values:

$$\rho = 1, \chi = 2\ , \gamma = -0.5, \sigma = 0.5$$

Figure 4.2 illustrates the steps of the algorithm for a 2D problem.

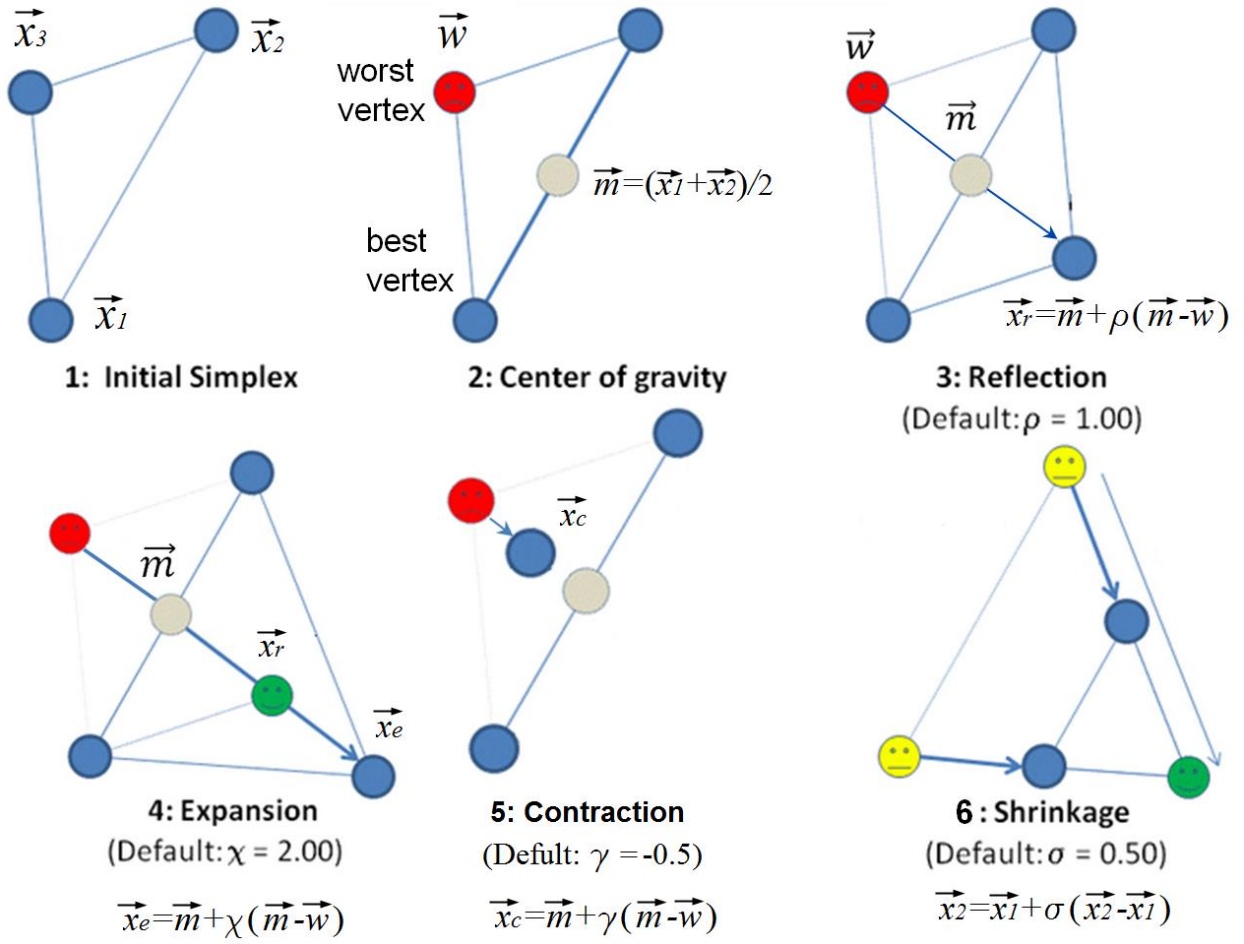

Figure 4.2. Main steps in the Nelder-Mead simplex optimization algorithm for a 2D problem. (Revised from http://capsis.cirad.fr/capsis/documentation/optimisation).

4.4.2. Genetic algorithm

Genetic algorithm (GA) was employed to find the three unknown coefficients *c*, *d* and *f* in the sigmoid density-elasticity relationship (Eq. 2). This is a search method for solving both constrained and unconstrained optimization problems by employing a selection procedure which simulates the biological evolution [136]. A population of candidate solutions (called creatures, or individuals) to the optimization problem is evolved continuously toward optimal solutions. At each iteration, the GA chooses individuals randomly from the recent population and employs them as parents to create the offspring for the following generation. The optimization process is

terminated when either the change in the objective function is less than the acceptable error for two consecutive iterations, or a maximum number of generations had been exceeded [137].

The main steps of GA to find the solutions of a problem are as follows [138]:

I. Creating a random initial population of individuals

II. Evaluating the fitness score of each individual in the population

III. Generating a new population using the individuals of the current population; the following sub-steps are repeatedly performed until the new population is generated:

- Selection: selecting individuals, called parents, according to their fitness scores (individuals with greater fitness scores have a higher chance to be selected)
- Crossover: creating population of children (offspring) by combining two parents
- Mutation: generating population of children by making random changes to a single parent
- Replacement: Substituting the recent population with the children population

IV. Termination: stopping the procedure if the termination criterion is satisfied.

Figure 4.3 depicts the steps employed in the GA procedure to identify the unknown coefficients. The termination criterion and the maximum optimization iterations were set to 10^{-5} and 200, respectively. The coefficients d and f in the sigmoid density-elasticity relationship should be negative. The GA was, therefore, used to allow for putting some constraints on these coefficients. The following constraints, selected from a previous study [67], were used to limit the search domain for accelerating the identification process:

$$\begin{aligned} [c]&: \{x \epsilon R | 10000 \leq c \leq 25000\} \\ [d]&: \{x \epsilon R | 0 < d \leq -10\} \\ [f]&: \{x \epsilon R | 0 < f \leq -5\} \end{aligned} \tag{4}$$

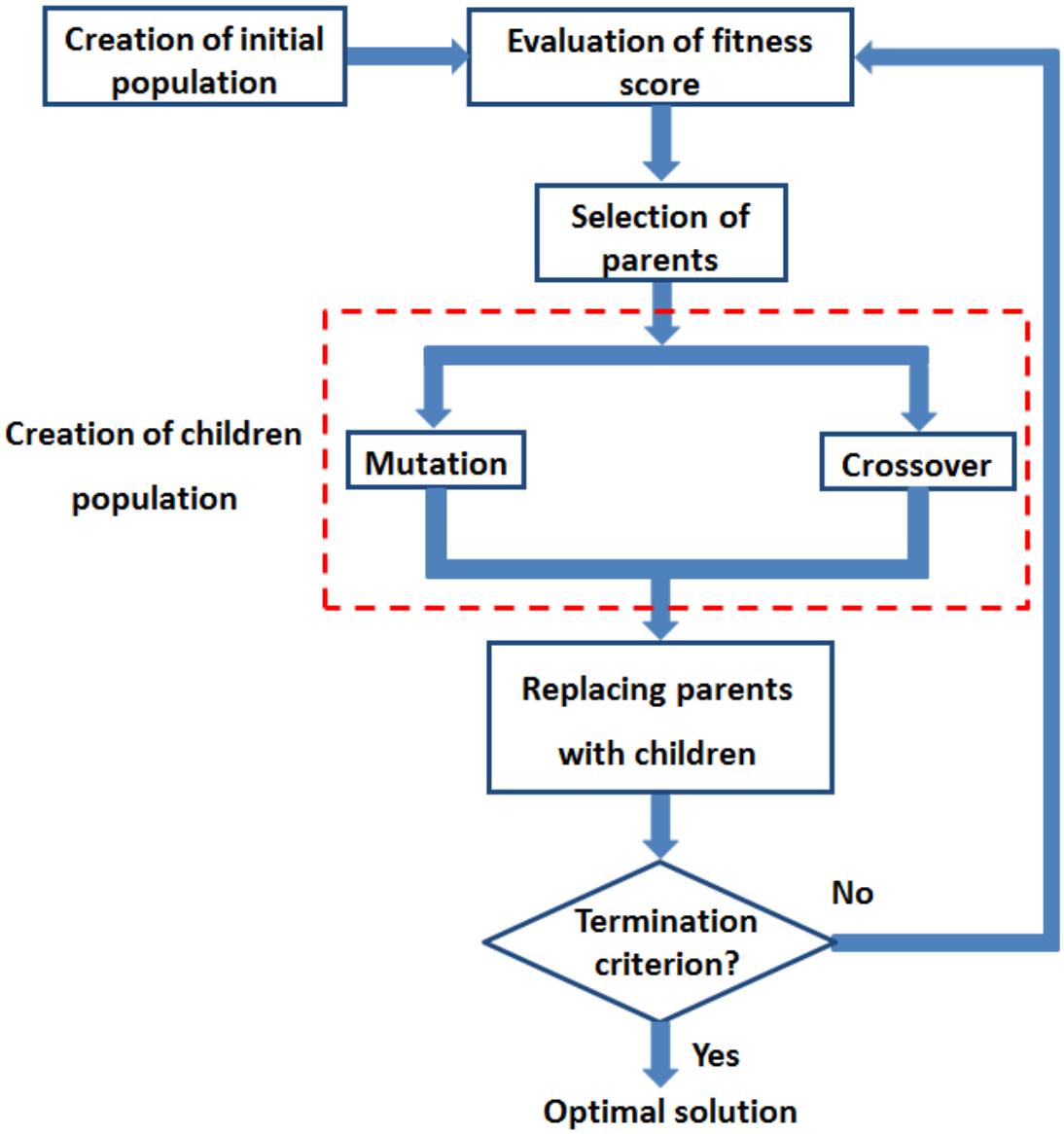

Figure 4.3. Steps used in GA procedure to search for the optimal parameters in the sigmoid function. (Used with permission of Mayo Foundation for Medical Education and Research, all rights reserved).

The performance of the optimal bone density-elasticity relationships obtained in the current study was evaluated compared to some of the commonly used bone density-elasticity relationships. To this end, five previously reported relationships [64-68] were applied to the FE models of the training and the validation femora, and the simulations were repeated under the same displacement loading of 0.6 *mm*. Two metrics were measured for each material model to

evaluate its performance: 1) the slope of the regression line between the FE estimated and the experimental stiffness values, and 2) their coefficient of determination R^2 compared to desired line $Y = X$, where Y denotes the estimated stiffness by FEA, and X denotes the measured stiffness by experiments.

4.5. Statistical Analysis

Several statistical analyses were used to compare different data sets. Regression analysis was used to examine the correlation between the FE estimated and experimental stiffness values for the training and validation femoral sets. Repeated measure analysis of variance (RM-ANOVA) checked the difference between the FE predicted stiffness resulted from the optimal density-elasticity relationships obtained in the current study and some of the previously proposed relationships. All of the statistical analyses were performed in MINITAB 16 (Minitab Inc., PA, USA). The statistical significance value (α) was set to 0.05 for all of the statistical analyses.

4.6. Results of Inverse Finite Element Analysis

Table 4.2 shows the characteristics and the experimental stiffness values of the femora in the training and in the validation sets.

Table 4.2. Characteristics and experimental stiffness values of training and validation femora. (Used with permission of Mayo Foundation for Medical Education and Research, all rights reserved).

	Training femora		Validation femora	
	Mean ± SD	Range	Mean ± SD	Range
Age (year)	72 ± 12	54-94	71 ± 16	37-99
aBMD (g/cm^2)	0.72 ± 0.18	0.42-1.10	0.73 ± 0.21	0.37-1.36
Exp. Stiffness (kN/mm)	1.4 ± 0.5	0.6-2.7	1.4 ± 0.6	0.5-3.0

The Nelder-Mead optimization algorithm for identifying the power density-elasticity relationship converged after 83 iterations, with the major decrease in the objective function from

0.318 to 0.255 within the first 10 iterations (Figure 4.4). The objective function at iteration 83 was 0.247, with a change less than the convergence criterion, 10^{-5}, compared to the previous iteration. The optimization process, therefore, terminated. The optimal values of the power law coefficients *a* and *b* were 11644 and 1.31, respectively. To assure that the obtained coefficients were the results of the global minimum of the objective function, the optimization process was repeated using another set of initial values (a = 4000 and b = 4) far from the first initial value set. The new initial values led to the same results as the previous ones. This showed that the obtained coefficients were the results corresponding to the global minimum of the objective function.

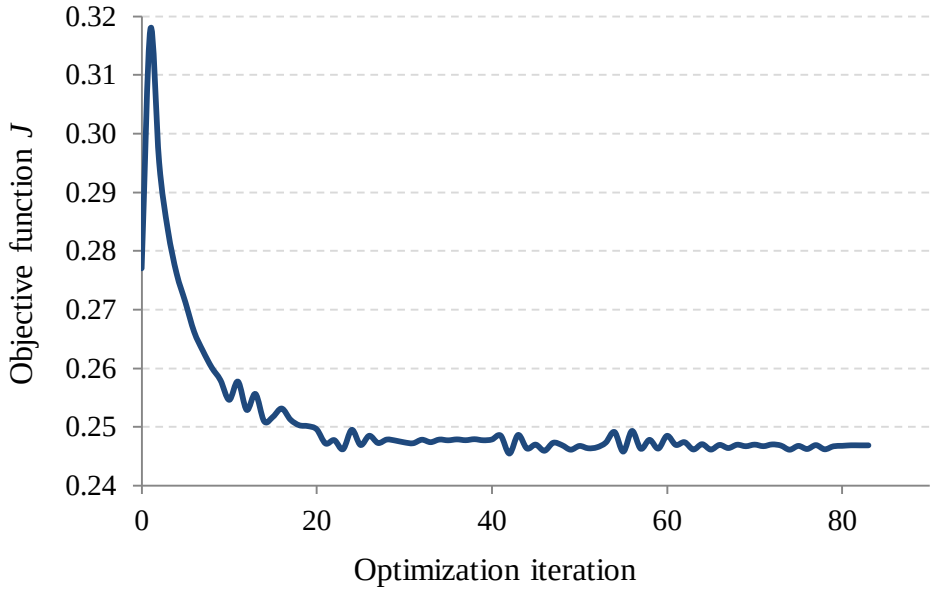

Figure 4.4. Variation of the objective function versus the optimization iteration during the parameter identification process for the power elastic-density relationship; after 83 iterations, the change in the objective function was less than the convergence criterion, 10^{-5}. (Used with permission of Mayo Foundation for Medical Education and Research, all rights reserved).

The obtained density-elasticity relationship was then applied to FE models of the validation femora. Figure 4.5 shows the FE estimated stiffness versus experimental stiffness values for both training and validation femoral sets. The coefficient of determination R^2 of the

estimated stiffness values compared to the desired line $Y = X$ was 0.67 and 0.72 for the training and the validation femora, respectively.

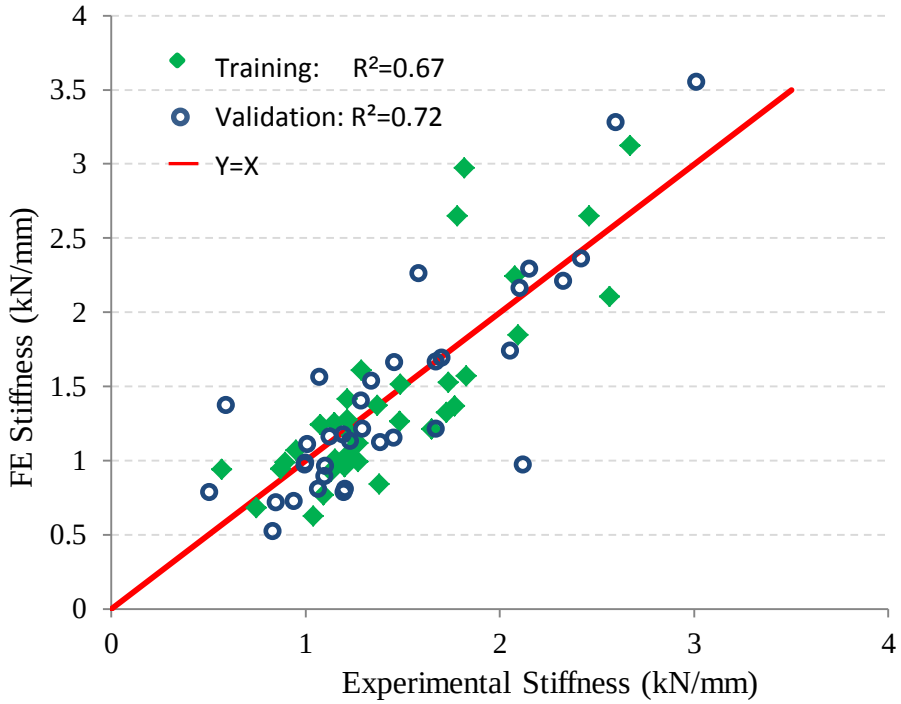

Figure 4.5. Variation of the FE estimated stiffness values versus experimental stiffness for the training and the validation femora using the optimal power density–elastic modulus relationship ($E = 11663\rho_{ash}^{1.31}$); the coefficient of determination R^2 was determined compared to the desired line $Y = X$. (Used with permission of Mayo Foundation for Medical Education and Research, all rights reserved).

Figure 4.6 depicts von Mises, shear, and maximum principal strain and stress contour plots throughout a typical femur under displacement loadings of 0.6 *mm*. As illustrated, the main deformation occurred in the proximal part of the femur composed of the head, neck, and greater trochanter. The shaft did not contribute significantly in the global deformation as it consisted of a thick cortex of stiff cortical bone.

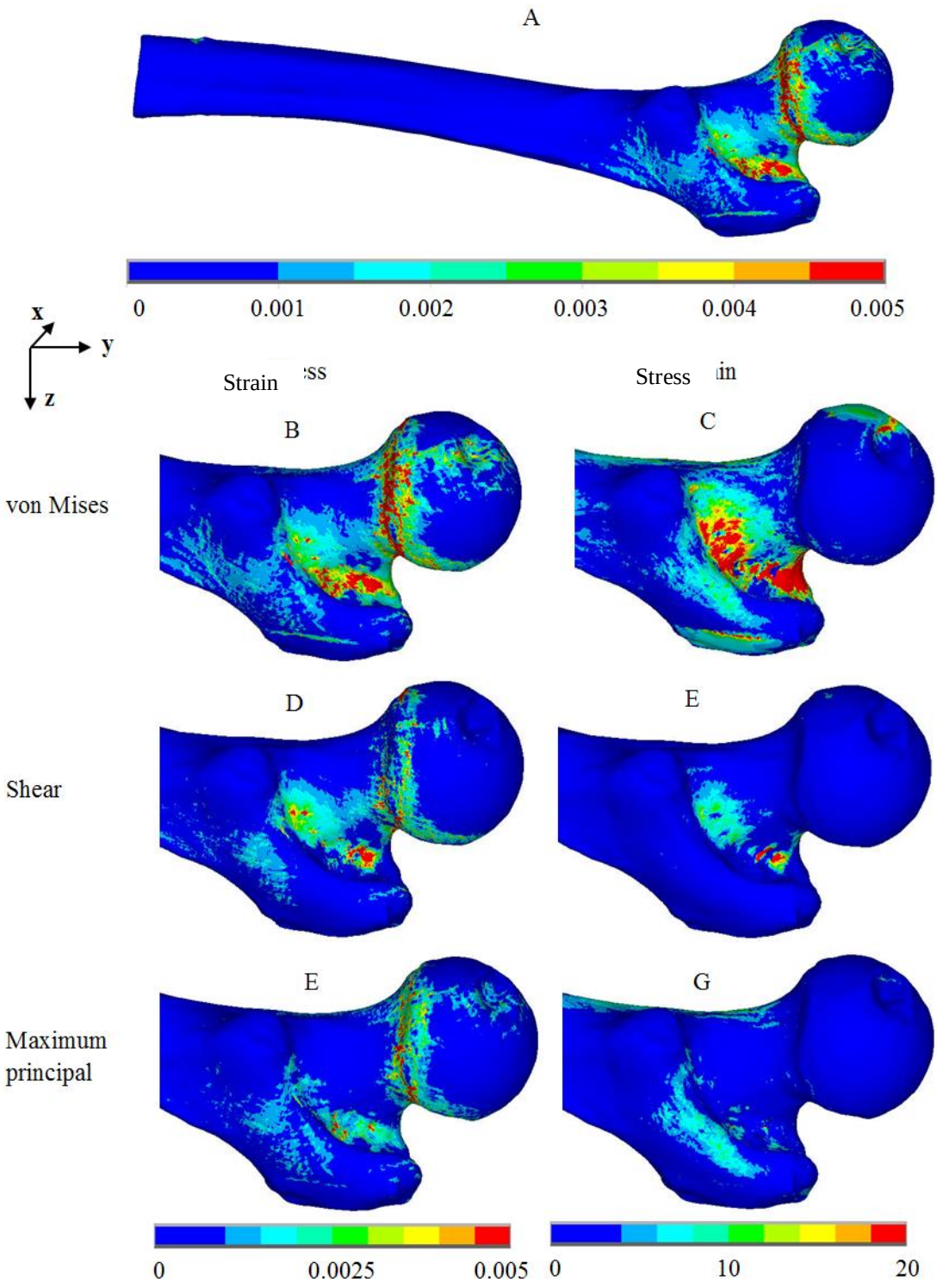

Figure 4.6. Stress (*MPa*) and strain contour plots of a typical femur under displacement loading of 0.6 *mm* in z direction; A) von Mises strain throughout the femur, B) von Mises strain, C) von Mises stress, D) Shear strain ε_{yz}, E) Shear stress σ_{yz}, F) Maximum principal strain, and G) Maximum principal stress in the proximal part. (Used with permission of Mayo Foundation for Medical Education and Research, all rights reserved).

For the sigmoid density-elastic modulus relationship, the GA optimization process converged after 109 iterations with the objective function value of 0.251. The optimal coefficients *c*, *d*, and *f* were 18838.0, -6.0, and -3.5, respectively. Figure 4.7 shows the variation of the objective function versus iterations in the GA optimization.

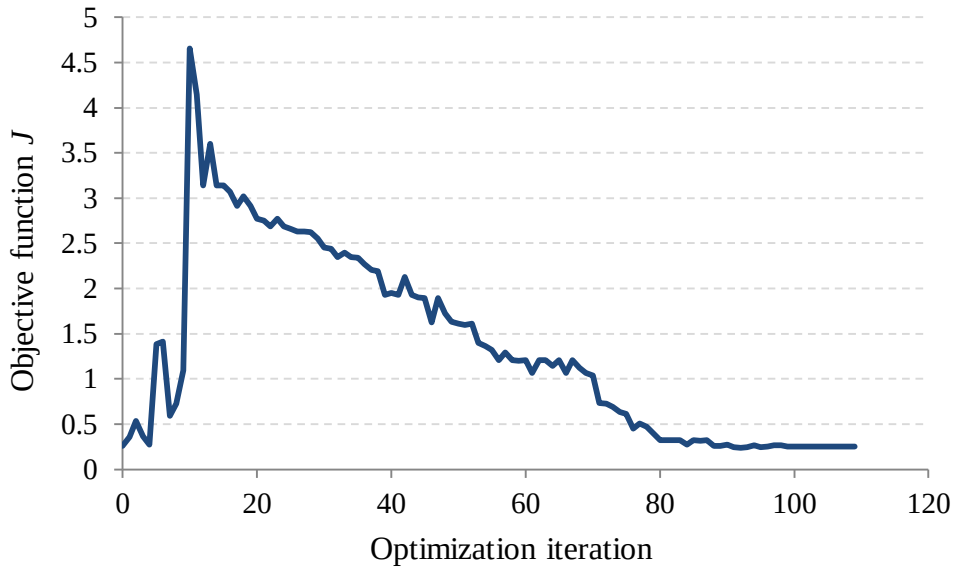

Figure 4.7. Variation of the objective function versus the GA optimization iterations in the parameter identification process for the sigmoid elastic-density relationship; the optimization process converged after 109 iterations. (Used with permission of Mayo Foundation for Medical Education and Research, all rights reserved).

Using the obtained sigmoid density-elastic modulus relationship, Figure 4.8 indicates the FE predicted stiffness versus the experimental stiffness for the training and the validation femora. The coefficient of determination compared to the line $Y = X$ was 0.67 for the training set and was 0.74 for the validation femora. Figure 4.9 illustrates the variation of the FE estimated stiffness versus the experimental stiffness for the training femora using different material models. RM-ANOVA revealed that the stiffness values resulting from the relationships obtained in the current study were significantly different from the stiffness values obtained from all the previous relationships except for the relationship proposed by Morgan et al. [66].

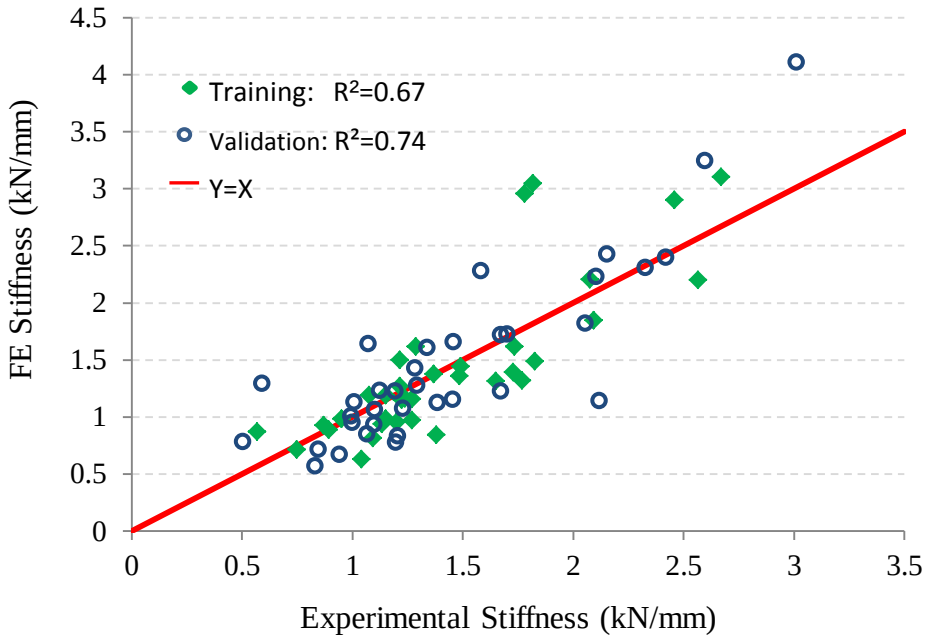

Figure 4.8. FE estimated stiffness versus experimental stiffness values for the training and the validation femora using the sigmoid density–elastic modulus relationship ($E = 18838e^{-6e^{-3.5\rho_{ash}}}$); the coefficient of determination R^2 compared to line $Y = X$ was 0.67 and 0.74 for the training and the validation femora, respectively. (Used with permission of Mayo Foundation for Medical Education and Research, all rights reserved).

Table 4.3 shows the slope of the regression line between the FE estimated and the experimental stiffness values and their coefficient of determination with respect to the line $Y = X$ for different density-elasticity relationships. The slope of the regression lines of the two models proposed in the current study were almost one, showing the accuracy of the prediction of these models. Figure 4.10 shows the variation of the bone elastic modulus (E, *GPa*) obtained from different relationships versus the bone ash density (ρ, g/cm^3). As depicted, the differences between all the proposed models were significant. Any conclusion about the accuracy of the relationships based on the illustration, however, is difficult. The two optimized material models of the current study showed the best fit to the experimental measurements both in the training and the validation sets, as anticipated.

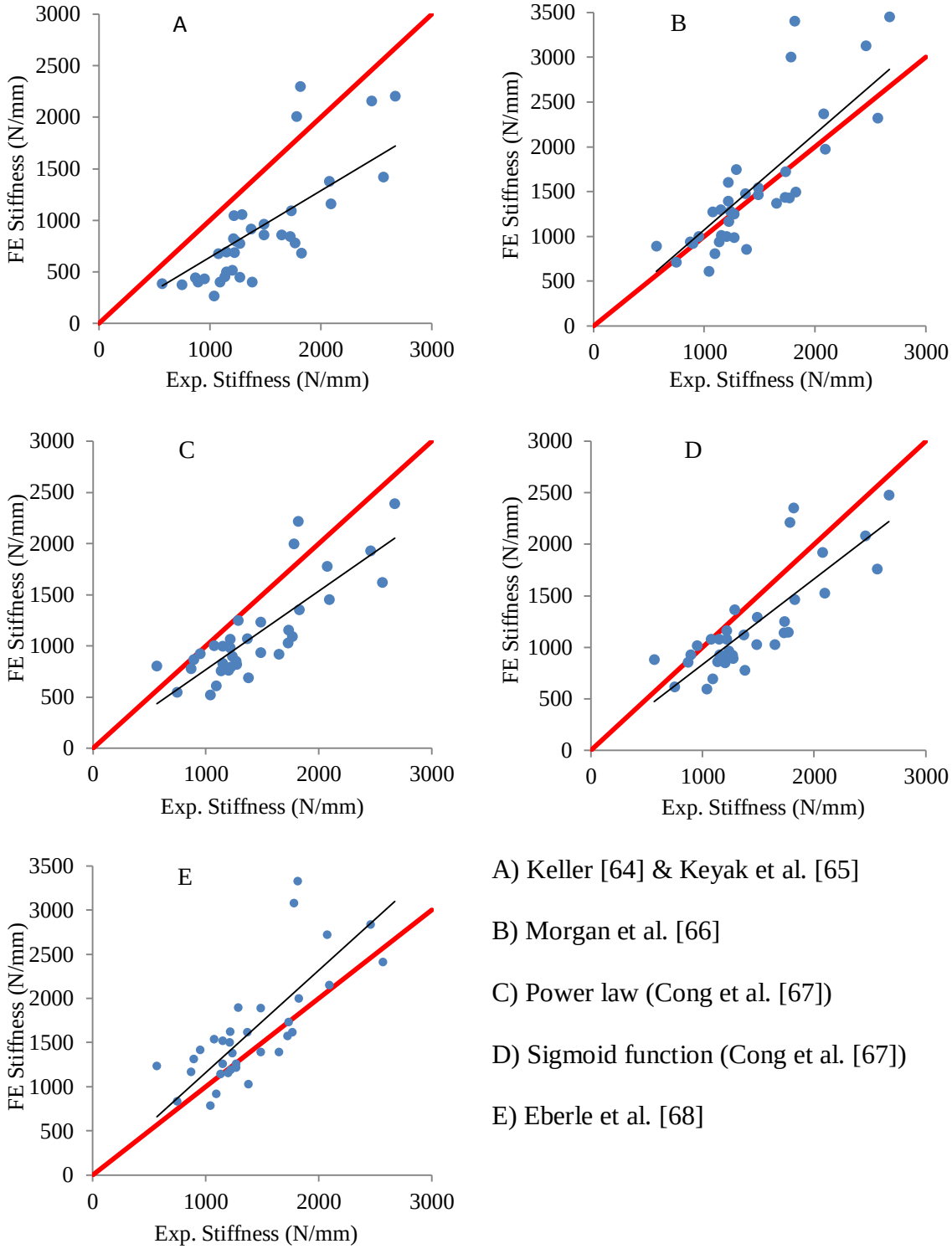

A) Keller [64] & Keyak et al. [65]

B) Morgan et al. [66]

C) Power law (Cong et al. [67])

D) Sigmoid function (Cong et al. [67])

E) Eberle et al. [68]

Figure 4.9. FE estimated stiffness versus experimental stiffness for the training femora using different material models; the red line is desired line $Y = X$. The black lines are regression lines with zero intercept to pass through the origin. (Used with permission of Mayo Foundation for Medical Education and Research, all rights reserved).

Table 4.3. Slope of the regression line between the FE estimated and the experimental stiffness values and their coefficient of determination in respect to line $Y = X$ for different density-elasticity relationships. (Used with permission of Mayo Foundation for Medical Education and Research, all rights reserved).

Density-elasticity relation	Reference	Training femora		Validation femora	
		Slope	R^2	Slope	R^2
$E = 11644\rho_{ash}^{1.31}$	Current study	0.99	0.67	1	0.72
$E = 18838e^{-6e^{-3.5\rho_{ash}}}$	Current study	1.01	0.67	1.04	0.74
$E = 33900\rho_{ash}^{2.2}$ $\rho_{ash} \leq 0.27$ $E = 10200\rho_{ash}^{2.01}$ $\rho_{ash} \geq 0.6$ $E = 5307\rho_{ash} + 469$ $other\ \rho_{ash}$	Keller [64]& Keyak et al. [65]	0.64	-0.43	0.69	0.06
$E = 6850\rho_{app}^{1.49}$	Morgan et al. [66]	1.07	0.64	1.1	0.7
$E = 8050\rho_{ash}^{1.16}$	Cong et al. [67]	0.77	0.07	0.76	0.17
$E = 15000e^{-4.9e^{-3.6\rho_{ash}}}$	Cong et al. [67]	0.83	0.37	0.84	0.50
$E = 12486\rho_{qCT}^{1.16}$	Eberle et al. [68]	1.16	0.52	1.17	0.57

Compared to the results of the power relationship in the current study, Morgan et al.'s relationship [66] seems stiffer through the whole range of density. A similar impression can be given in the comparison of the constants of the two power relationships; both constants of the power relationship obtained from the current study were lower than those in the study of Morgan et al. [66], implying that the later overestimated the moduli of the bone. However, the correlations of their relationship were 64% and 70% for the training and the validation sets, respectively, showing the closest agreement with the results of the current study.

Figure 4.10B is a subset of Figure 4.10A in a smaller range of density up to 0.5 g/cm^3. It brings about an interesting hypothesis in that for this range of densities, the model presented by Morgan et al. [66] shows the closest agreement with the power model presented in the current study.

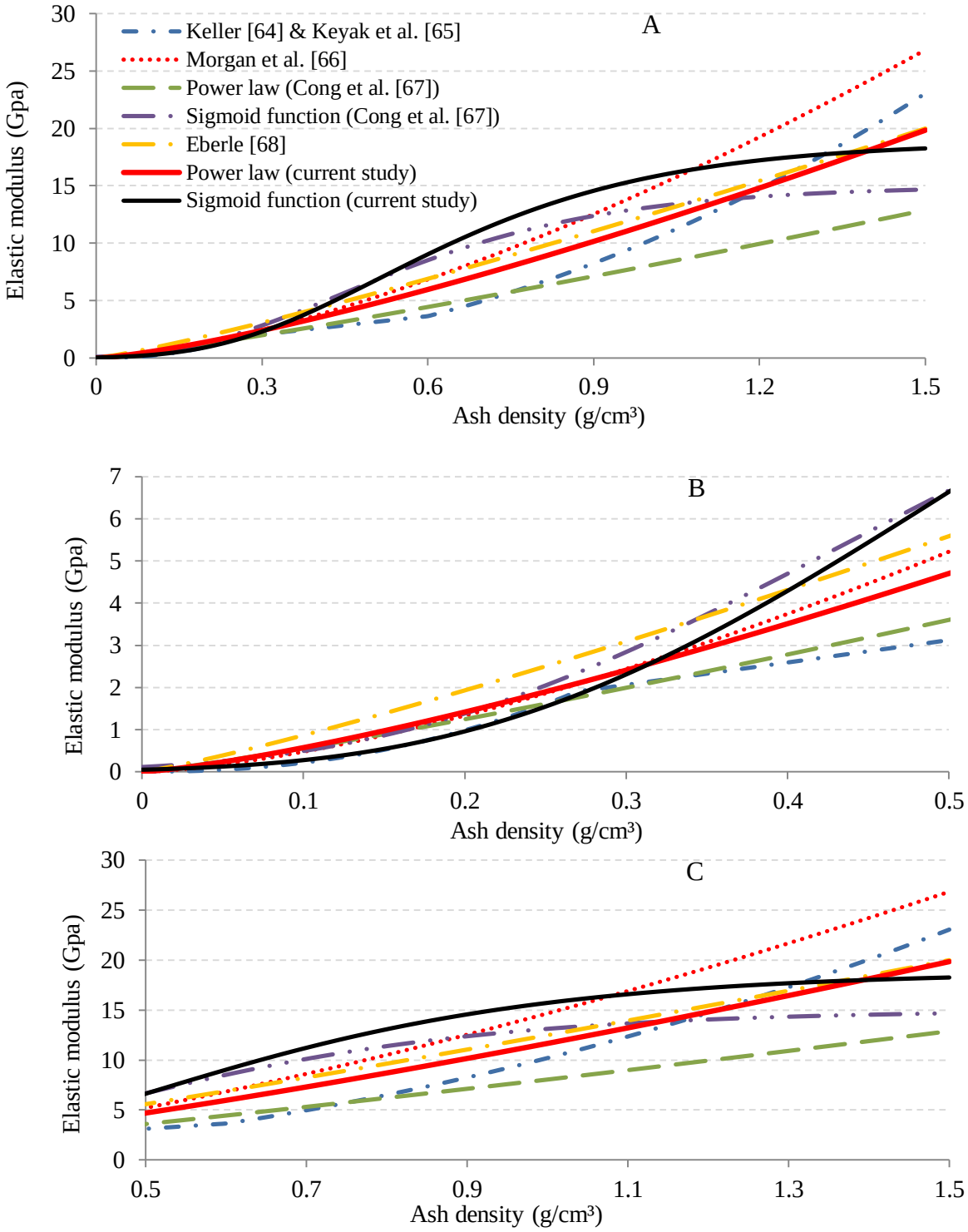

Figure 4.10. Variation of the bone elastic modulus (*GPa*) obtained from different material models versus the bone ash density (g/cm^3); for A) all densities, B) densities lower than 0.5 g/cm^3, and C) densities greater than 0.5 g/cm^3. (Used with permission of Mayo Foundation for Medical Education and Research, all rights reserved).

The two models predict the response of the trabecular bone accurately. Surprisingly enough, more than 85% of the bone volume belongs to the range of densities of up to 0.5 g/cm^3. The contribution of this part in the stiffness is, however, dominant as compared with the rest of the bone with the densities ranging from 0.5 to 1.5 g/cm^3. The second closest model to the experimental data, as well as the results of the current study, is the model presented by Eberle et al. [68] with the correlations of 52 and 57%, respectively, for the training and the validation femora. For the bone densities of up to 0.5 g/cm^3, Eberle's et al. model [66] showed a relatively larger discrepancy in elastic modulus to the power law model of the current study. For higher densities, however, the prediction was more accurate. Their experiments were on the whole femora in a stance-like configuration, while the current study accounted for a fall on the hip scenario. It may explain the over prediction of the bone response by their model. The sigmoid function presented by Cong et al. [67] showed weaker correlations of 37 and 50% for both femoral sets.

Although a strain-based failure criterion was employed in the current study, investigating the stress values predicted by different material models could reveal useful information. At the tissue level in the elastic region, stress distributions were highly influenced by density in different models. Using different density-elasticity relationships, Figure 4.11 shows the von Mises stress (*MPa*) estimations at three different sites inside the neck with the densities of 0.24, 0.7, and 1.21 g/cm^3. As clearly depicted, the different models predicted different stresses for the same site of the bone. Figure 4.11A presents the stress values at the location with the density of 0.24 g/cm^3 which corresponds to the trabecular bone. The model of Eberle et al. [68] predicted the highest stress values while the results of the sigmoid function (current study) showed the lowest. While those local stresses may not affect the stiffness of the whole femur, post-yield

response of the bone can be dictated by such stress localization. Figures 4.11B and C, on the other hand, predicts the highest value of von Mises stresses for the sigmoid function of the current study and the model presented by Morgan et al. [66], respectively. As one of the aims of the QCT/FEA is to predict the fracture type and the area of fracture initiation, such different patterns in the distribution of stresses throughout the bone may contribute to predicting failure at undesirable sites of the bone.

Figure 4.12 shows the variation of trochanteric force (*N*) versus head displacement (*mm*) for a typical femur using different material models. As illustrated, the power and the sigmoid relationships obtained in the current study and the Morgan et al.'s model [66] resulted in very similar elastic deformations as the experimental data. The other material models underestimated, or overestimated, the elastic deformation.

4.7. Discussions and Conclusions

Material properties of the bone dictate the accuracy of the QCT/FEA in prediction of the responses of the tissue from elastic to failure. In the current study, an inverse computational-experimental approach was employed to a large sample size of female femora with a variety of ages and aBMD representative to identify the bone density-elasticity relationships. The experimental setup mimicked proximal femoral fractures in a fall on the hip. The obtained elastic modulus relationships were then cross-validated on another large and varied femoral set.

The coefficient of correlation for the cross-validation femoral set was higher than the ones of the training femora for both obtained power and sigmoid density-elasticity relationships. This confirmed the robustness of the identified elastic modulus relationships because the validation set was an independent representative of the population. Statistical analyses did not

show any significant difference between the experimental and FE estimated stiffness values (p = 0.65).

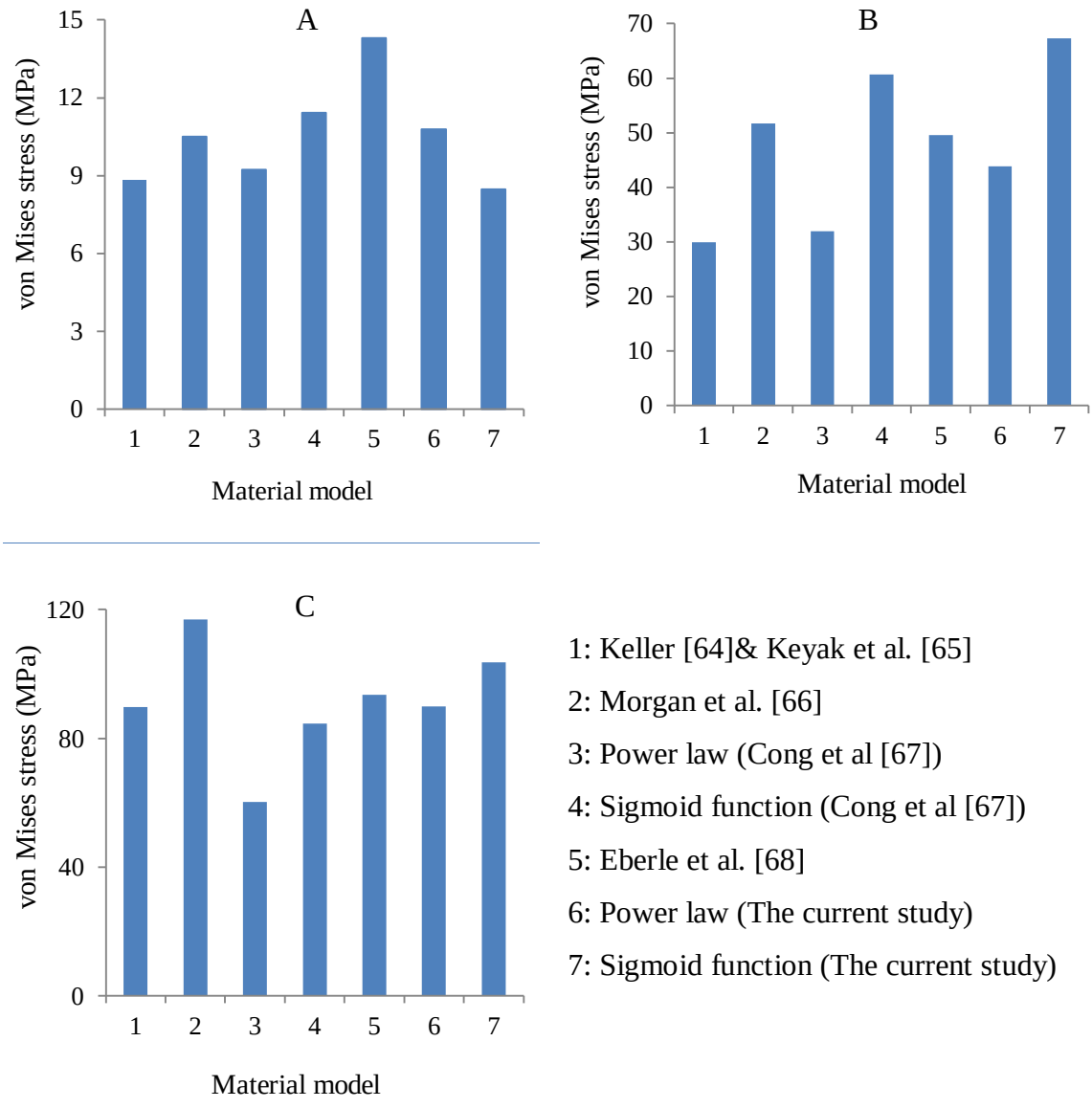

Figure 4.11. von Mises stress predictions at a strain level of 0.6% using different material models at different location inside the femoral neck with the densities of A) 0.27, B) 0.7, and C) 1.2 g/cm^3. (Used with permission of Mayo Foundation for Medical Education and Research, all rights reserved).

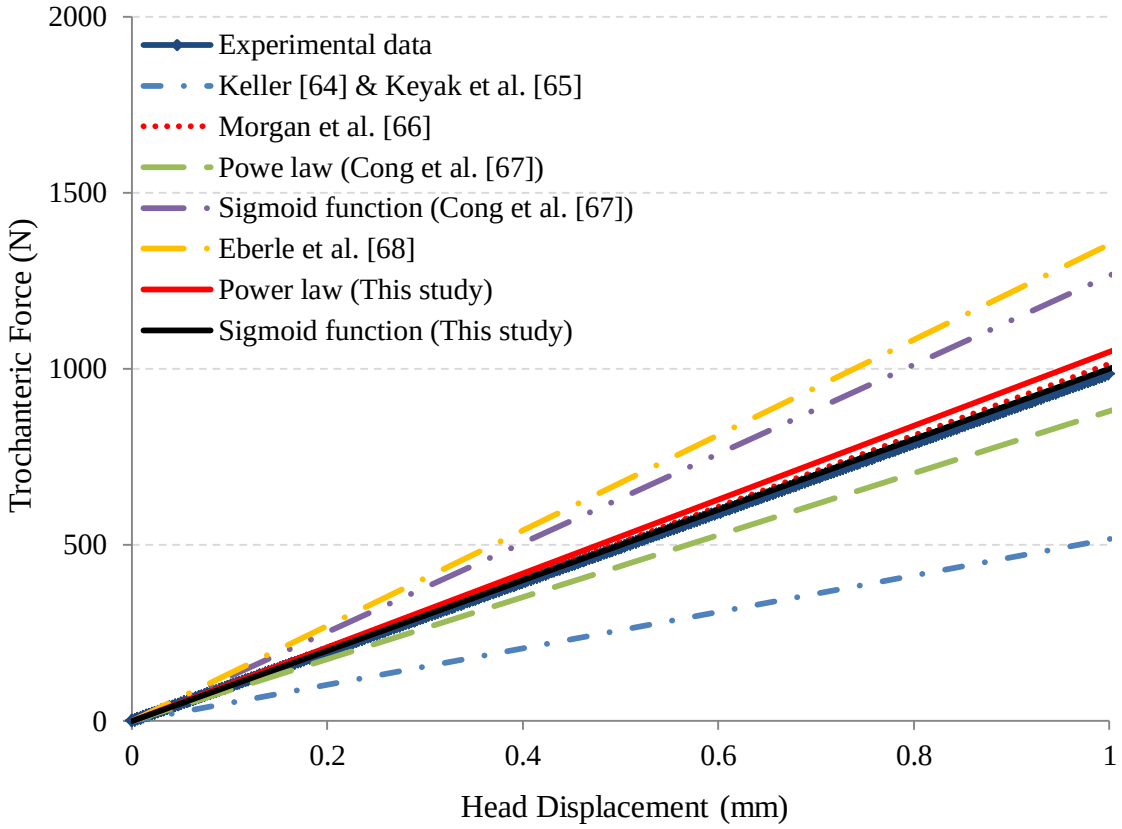

Figure 4.12. Variation of trochanteric force (*N*) versus head displacement (*mm*) for a typical femur using different material models. (Used with permission of Mayo Foundation for Medical Education and Research, all rights reserved).

In terms of stiffness, both power and sigmoid relationships of the current study resulted in acceptable agreement with the experimental data, having the correlation coefficient of more than 0.67. More importantly, the slope of the regression lines was almost one for both models (Table 4.3). It is noteworthy to mention that while the power as well as the sigmoid relationships showed very close performance to explain the global response of the bone in the elastic region, there were intrinsic differences between the two models at the tissue level. The sigmoid relationship assigned a different modulus pattern to the material bins defined in the FEA models; in the areas with small and high densities, the rate of change in the moduli of the materials were very small, while in the locations with the densities between about 0.3 and 0.7 g/cm^3, the rate of change became the highest. This pattern created a large gap between the sigmoid and power

relationships to explain stress distribution throughout the bone. For instance, the elastic modulus of the locations with the density of 0.8 g/cm^3 was calculated as 8.85 and 13.25 *GPa* based on power and sigmoid relationships, respectively. The prediction of the two models, in terms of mechanical parameters such as stresses and strains, in those specific locations led to 50% difference which was significant. This could be important in the post-yield behavior of the bone as well as in the prediction of ultimate strength.

The current study also revealed the fact that during a fall on the hip, the local deformation of the femoral neck plays an important role in the global stiffness. The majority of this region is made of soft and trabecular tissues with the densities in the range of up to 0.5 g/cm^3. In the characterization of density-elasticity relationships, they should, therefore, be treated carefully. The reason that the Morgan et al.'s [66] relationship resulted in stiffness estimations having a good correlation with the experimental data lies in to the fact that their coupon specimens were harvested from the neck region of the femora.

Applying the results of the current ex-vivo study to in-vivo is limited as the bone surrounded in a complicated muscular and ligamentous system is different from the experimental setup used in the current study. Moreover, during a fall on the hip, the femur does not have direct contact with the ground, as a layer of soft tissue helps attenuate the level of transferred load to the bone. Therefore, the application of the obtained density-elasticity relationships should be carefully used in FE models of bones in-vivo.

CHAPTER 5. OPTIMIZED EVALUATION OF YIELD AND POST-YIELD PROPERTIES OF FEMALE FEMORA USING INVERSE FINITE ELEMENT ANALYSIS

This chapter is about a computational-experimental study that was employed to investigate the failure and damage behavior of female femoral bones under a complex loading scenario. Both ductile and brittle material behaviors were assumed separately for the bone tissue in the FE modeling of a set of femora simulating a fall on the hip loading configuration. Genetic algorithm integrated with an IFEA was employed to find the unknown coefficients in the yield and post-yield material models by matching the FE estimated results to their experimental counterparts. Finally, the performance of the ductile and brittle material models for use in the subject-specific modeling of femora was evaluated.

5.1. Introduction

The mechanical properties of the bone tissue can be classified into three main categories as elastic, plastic, and damaged. From biological and clinical points of view, the ability to predict damage in tissues is of great significance. In this regard, accurate definition of yield and post-yield behaviors in plastic regions of the tissue plays an important role in understanding the process of damage. Due to difficulties in performing experimental and computational studies, however, post-yield characterization of femoral bones has been a challenging issue for years. There has been a wealth of published data in the literature for several decades that addresses bone fracture. McElhaney [139] performed experimental studies on human and bovine bone coupons to measure the mechanical properties of the bone up to fracture with the emphasis on the effect of load speed. Carter and Hayes [110] conducted several destructive experiments on the bones of the same species as in the study of McElhaney [139] and measured the stiffness and

strength of the bone. Keller [64] carried out a large number of experiments on small human bone samples at different sites of the bone showing that the compressive material properties of the bone can be best explained by ash density.

The advent of computers helped researchers vastly employ numerical methods to gain additional insight into the mechanics of bone fracture by being able to perform subject-specific simulations and macro-to-nano analyses. Several models, from simplistic to complex, explain plastic deformation of the bone as well as its damage. von Mises yield stress criterion, and then plastic flow, was employed on cadaveric femora in a stance-like loading configuration using QCT/FEA showing that this method can potentially be a good predictor of femoral fracture risk [86, 140, 141]. Despite utilizing simplistic nonlinear constitutive equations, the results showed a close agreement with the experiments. Keyak et al. [142] proposed von Mises stress to define the yield criterion. The plastic region was defined as a function of ash density. In the post-damage region, the moduli of the elements were degraded to a density-dependent constant stress value.

Using high-resolution FEA, Niebur et al. [143] proposed a bilinear constitutive equation with asymmetric yield strain in tension and compression. They assumed similar yield strains for both cortical and trabecular bones, and used minimum and maximum principal strains as yield criteria under compression and tension, respectively. Imai et al. [144] combined a maximum principal strain failure criterion with a Drucker–Prager yield surface to estimate the mechanical behavior of the vertebral body. When the Drucker-Prager equivalent stress exceeded a specific value, the material yielded. The fracture was also expressed based on the minimum principal strain of 10,000 micro-strain. To define those thresholds, they employed a bilinear elastoplastic constitutive law with a tangential modulus of 5% of the elastic modulus. This model was later used by Bessho et al. [94] for femora in a stance-like loading configuration. Koivumaki et al.

[60] used similar Drucker-Prager equivalent stress as a yield criterion for femora in a sideways fall loading configuration. They considered maximum principal stress and minimum principal strain as fracture criteria in tension and compression, respectively. The advantage of using principal stresses and strains is the ability to include tensile/compressive asymmetry.

Keaveny et al. [145] and Keaveny et al. [146] applied a cast iron material model to simulate the bone mechanical behavior, allowing distinction of yield properties in tension and compression. Dragomir-Daescu et al. [54] used a power law to characterize the yield strain of the bone based on von Mises strain. They concluded that using this failure criterion, the QCT/FEA method is potentially capable of predicting femoral stiffness, fracture load, and fracture pattern. Hambli et al. [112] used a maximum equivalent strain as a yield criterion and a quasi-brittle damage model for proximal femora in a stance-like loading configuration. These simple constitutive models led to a fair estimation of fracture loads and, to some extent, fracture patterns.

The sophisticated bone material models, which mostly use an eccentric ellipsoid shape yield surface, describe the yield behavior of porous materials well [147, 148]. Zysset and Rincón [149] proposed a piece-wise Hill criterion for the bone tissue. Afterwards, Rincon and Zysset [150] fitted this model to experimental data. Wolfram et al. [151] used a fabric-dependent Tsai–Wu yield surface for the bone and identified its material parameters. More recently, a crushable foam plasticity model, as a simplified approximation of the Tsai–Wu yield surface, was proposed by Kinzl et al. [78]. The sophisticated material models have the following disadvantages:

I. Application of these models on QCT/FEA models is complicated. Most of these models are not available in commercial FE software,

II. There are usually several coefficients in these models which need to be identified. The identification of these unknown constants using experimental results is complicated,

III. These material models are usually anisotropic. In order to find anisotropic directions for each element in a bone FE model, the model needs to be developed from micro-CT scans showing the material directions in the trabecular bone. The resulted FE models would have millions of elements which are not computationally affordable for clinical applications.

Despite a great deal of valuable effort, the literature still lacks a robust, accurate, and at the same time, simple model to estimate the mechanical behavior of femora in a sideways fall impact. Further investigations are certainly required to address the post-yield response of the bone. The current study investigated the response of femoral bones from the initiation of failure to complete fracture. Both assumptions of ductility as well as brittleness were considered and their yield and post-yield behaviors were determined accordingly by employing IFEM. The results of the QCT/FEA method were also compared with their experimental counterparts.

5.2. Bone Ductility and Brittleness

Accurate definition of the post-yield behavior of the bone lies in understanding the mechanism of fracture. There is no general agreement on how a bone undergoes failure. While one hypothesis explains plastic deformation as the main reason of fracture [4, 152], some researchers postulate that the bone is a quasi-brittle material in nature and fails abruptly after reaching up to the yield point [61].

In practice, the bone has an intricate anatomy, materially, and cannot be simply categorized into the brittle or ductile fracture behavior. Figure 5.1 demonstrates two different experimental data that can be described differently. Figure 5.1A depicts the bone that undergoes

no plasticity up to ultimate strength and then large displacement up to final damage. The yield point is not easily distinguishable and it fails abruptly when its linear region ends. This fracture can be considered as brittle. Figure 5.1B, on the other hand, illustrates a bone that experiences relatively high plastic deformation in its response and it undergoes a gradual failure. The ultimate strength occurs after the head displacement of around 9 *mm*, a large part of which is in plastic region. This bone acts as a ductile material.

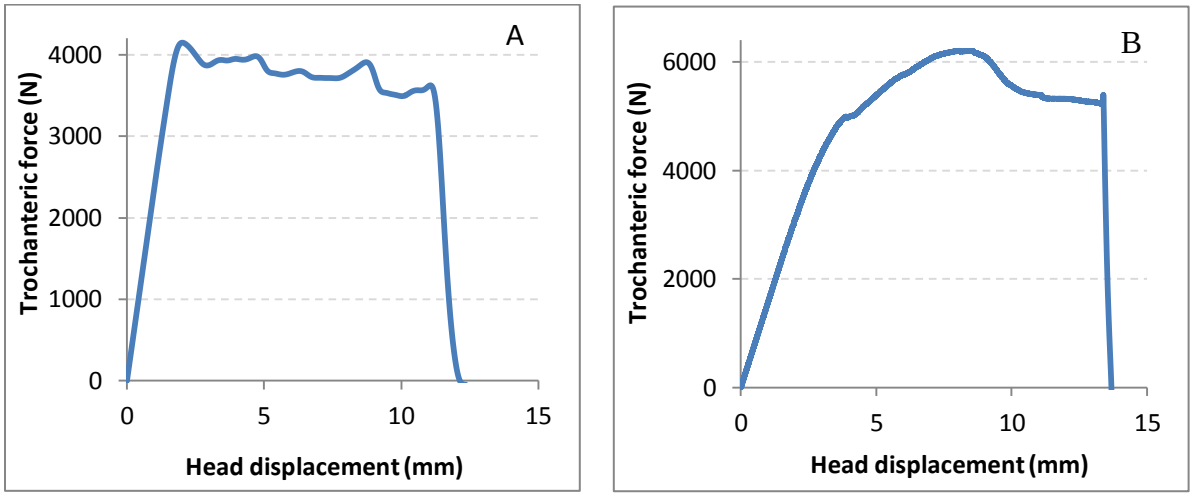

Figure 5.1. Experimental force-displacement data for two different bones showing (A) brittleness and (B) ductility in their responses. (Used with permission of Mayo Foundation for Medical Education and Research, all rights reserved).

In the fracture experiments explained in chapter 2, there are several bones that can be categorized in between these two different failure types and are therefore difficult to be explicitly explained. Undoubtedly, one single model cannot be employed to address such different post-yield phenomena. In the current research, both material behaviors were studied separately and the constants of interest were determined and compared (Figure 5.2). To consider the bone as a brittle material in which the damage occurs at the onset of yield point without plasticity, the following simple model, as illustrated in Figure 5.2A, can be implemented. As soon as an element in the FE simulations yields, it is deactivated with reducing its modulus to a very small

value (0.01 *MPa*). Deactivated elements cannot bear any stress while deforming, and all the stresses and strains are eliminated from its history. This model is computationally affordable and applicable for clinical purposes as the material model is linear.

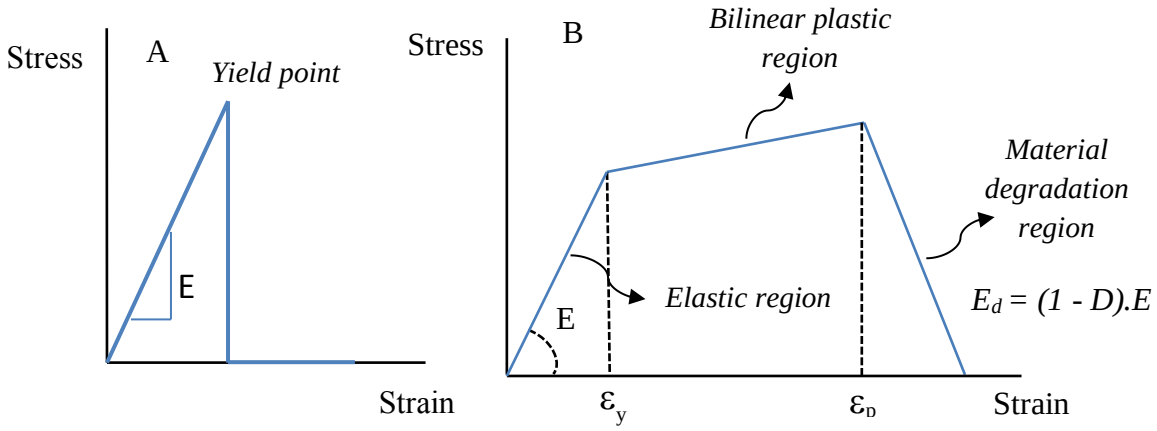

Figure 5.2. Schematic fracture models for the bones that considered as (A) brittle and (B) ductile materials.

On the other hand, to model the material undergoing a considerable amount of plasticity a bilinear constitutive equation can be utilized [94, 144]. Yielding occurs at a specific strain or stress threshold level, and then as the deformation continues to the damage threshold, after which the material degrades. In the current study, a linear isotropic damage model was considered to represent the material degradation at the end of the plastic region [153]. During the material degradation phase, the elastic modulus of the material (E, *MPa*) decreased linearly by a damage coefficient of *D* [61]. In the damaging phase, the relationship between stress (σ, MPa) and strain (ε) is expressed by the following equation:

$$\sigma = E_d \varepsilon \tag{1}$$

$$E_d = (1 - D).E\,, \quad 0 \leq D \leq 1$$

where E_d (MPa) is the modulus of the material during the damaging phase, $D = 0$ represent the undamaged material, and $D = 1$ express the fully fractured material which cannot bear any load. Figure 5.2B shows a stress-strain curve, representing three distinct material models (elastic, plastic, and damage) for a typical material. Different assumptions have been made in prior studies to explain the post-yield behavior (from the onset of yield to fracture). Some have assumed that the post-yield strain (ε_p- ε_y) is density dependent [65, 142] while many have shown that the post-yield strain is a constant parameter [94, 144]. In the current study, the post-yield strain and the damage coefficient were assumed as constant values of 0.0015 [94] and 0.99 [61], respectively.

5.3. Yield Criterion Optimization Procedure Using IFEM

A set of nine cadaveric female femora (age: 58 ± 10; neck aBMD: 0.82 ± 0.27; 3 of normal, 3 osteopenic, and 3 osteoporotic based on neck aBMD) was selected for the purpose of optimization. The experimental yield force was determined from the force-displacement data for each femur (chapter 2). An isotropic von Mises strain-based criterion was employed to represent the onset of yielding in FE models. The optimal density-elasticity relationships presented in the previous chapter were employed to assign elastic modulus to the FE models. The following power law was assumed to define the threshold of yield criterion as a function of bone ash density [54]:

$$\varepsilon_y = f\rho_{ash}^{g} \tag{2}$$

where f and g are unknown constant coefficients. Similar to the derivation of the elastic material constants explained in chapter 4, an IFEM integrated with a GA procedure was employed to identify the unknown coefficients in the yield criteria. Figure 5.3 demonstrates how the algorithm searches for the optimum values of interest, f and g.

At each iteration, the force of estimated yield point ($\bar{F}$) was compared with that of experimental results (F) to form the objective function.

$$J = \sqrt{\frac{1}{n}\sum_{i=1}^{n}\left(1 - \frac{\bar{F}_i}{F_i}\right)^2} \quad (3)$$

The large difference between the optimization of yield point with that of elastic modulus was the computational cost of the process as the number of FE steps was larger and, more importantly, nonlinearity was included. In addition to the time consumption, the nonlinearity in the bilinear model could have caused convergence issues. The obtained bone density-yield strain relationship was then cross-validated on another set of nine female femora.

5.4. Results of Post-Yield Optimization

5.4.1. Bone as a ductile material

Using the ductile material model in the FE models, the GA procedure for identifying the density-yield strain criterion relationship (Eq. 2) converged after 66 iterations. The major decrease in the objective function occurred within the first 15 iterations from 0.335 to 0.275 (Figure 5.4). The objective function at iteration 66 was 0.270, with a change less than the convergence criterion, 10^{-5}, compared to the previous iteration. The optimization process was, therefore, terminated. The optimal values of the coefficients f and g in Eq. 2 were 0.008 and -0.7, respectively. Figure 5.5 depicts the FE estimated yield force versus the experimental yield force for both the training and validation femoral sets. The coefficient of determination R^2 of the estimated yield forces compared to the desired line $Y = X$ was 0.96 and 0.98 for the training and validation femora, respectively.

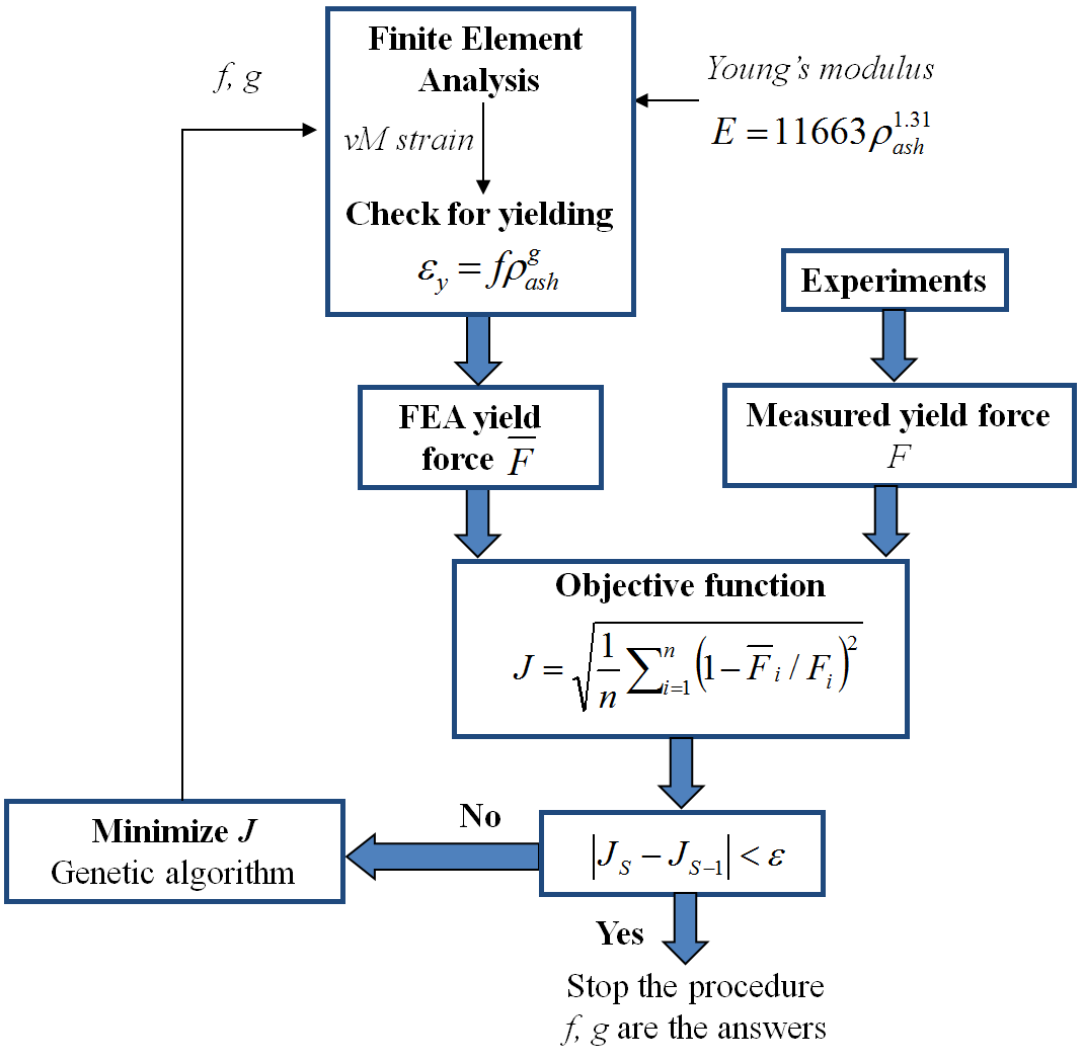

Figure 5.3. Flowchart of the optimization procedure used to identify the unknown coefficients in the bone density-yield strain relationship; GA was used to find the optimal coefficients in the yield strain relationship used in FE models by minimizing the objective function J between the experimental (F) and FE estimated yield forces ($\bar{F}$). (Used with permission of Mayo Foundation for Medical Education and Research, all rights reserved).

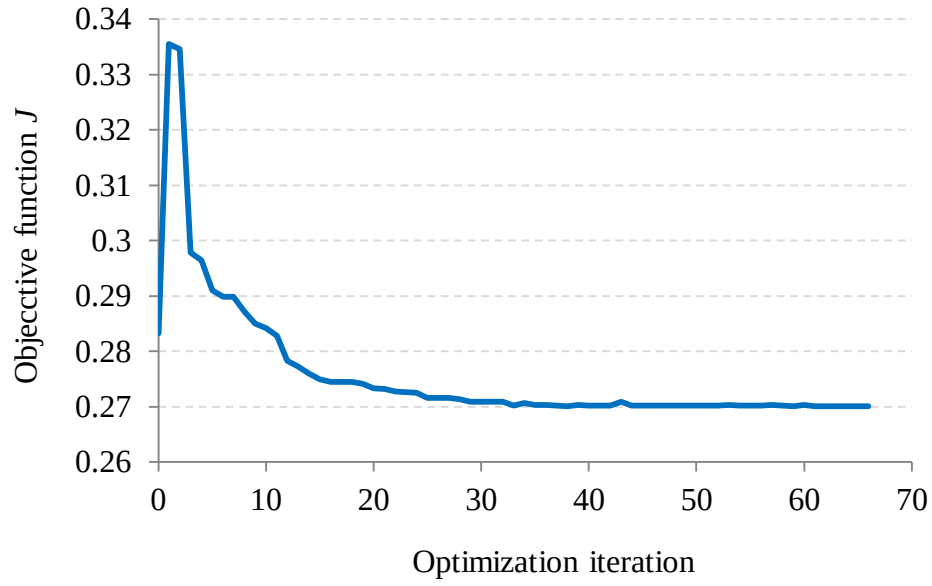

Figure 5.4. Variation of the objective function versus the optimization iterations in the parameter identification process for the density-yield strain relationship; the optimization process converged after 66 iterations. (Used with permission of Mayo Foundation for Medical Education and Research, all rights reserved).

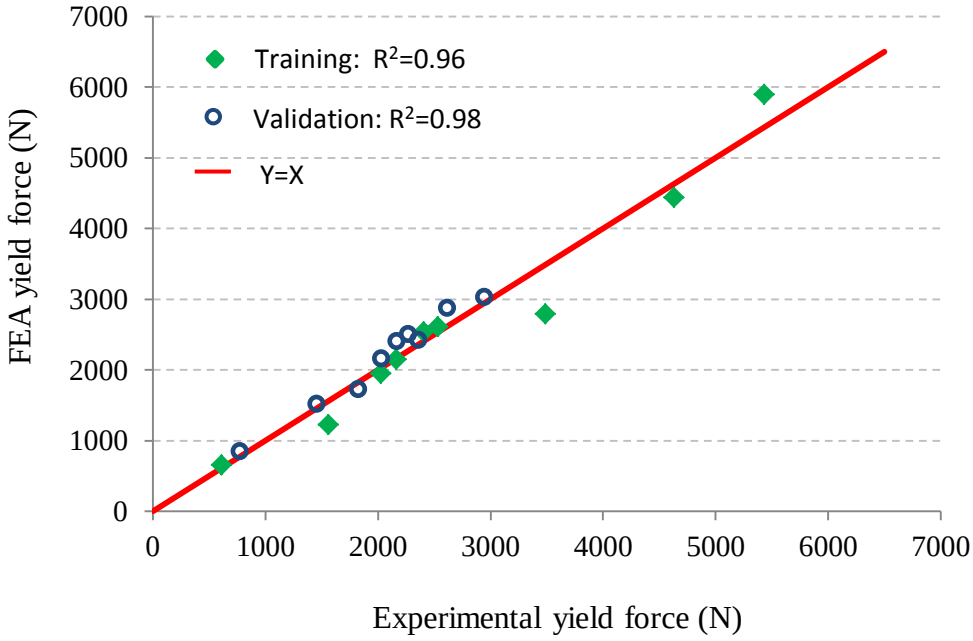

Figure 5.5. Variation of the FE estimated yield force versus experimental yield force for nine femora using the optimal density-yield strain relation ($E = 0.008\rho_{ash}^{-0.7}$); the coefficient of determination R^2 with respect to desired line $Y = X$ was 0.96 and 0.98 for training and validation femora, respectively. (Used with permission of Mayo Foundation for Medical Education and Research, all rights reserved).

In this chapter the term "yield" refers to the transition of material deformation from elastic to plastic, while the term "fracture" indicates the final rupture of the bone. Computational and experimental results of a typical femur, indicating the location of yielding initiation and growth through the neck, are shown in Figure 5.6. At the onset of yield (Figure 5.6A), about 700 elements (3% of the neck volume) yielded resulting in 2% deviation of the force-displacement curve from the straight line. Surprisingly, about two thirds of the elements that initially yielded underwent fracture as a result of which they got inactivated by ANSYS. They had no contribution, therefore, to the stiffness of the structure afterward. As the deformation continued, more elements were yielding and then fractured (Figure 5.6C). At the instant of experimental fracture, more than 2100 elements (10% of the neck volume) underwent yielding of witch the majority fractured (more than 7% of the neck volume). As depicted, the fractured region was all around the neck which was under compression. The fractured region also belonged to the cortical part of the bone as the most dense and stiff area. This type of fracture led to sinking of the head and the superior neck region into the greater trochanter of the femur. Figure 5.6D also illustrates, experimentally, the sinking event that confirmed the prediction of the computational analysis. As depicted in Figure 5.6C, the fatal fracture occurred on top of the neck under tensile loading. At this stage, the whole neck was broken abruptly.

Figure 5.7 shows different strain contours in the areas of interest. Yielding in elements occurred when the von Mises strain values exceeded the threshold defined by Eq. 2. After undergoing a constant value of strain, the yielded elements experienced fracture until the structure collapsed. The strain contours at the fracture displacement of 2.4 *mm* contained fewer elements with high strain values (shown in red color in Figure 5.7), because the software had already deactivated the elements fractured in previous simulation steps. In terms of von Mises,

first principal, and shear strains, similar patterns could be predicted in Figure 5.7. Likewise, the stress contours of the femur at the same displacements are illustrated (Figure 5.8).

From the displacement of 1.3 to 1.5 *mm*, the areas with high stresses (shown by red color in the contour plots) became larger contributing to more elements yielding. Comparing the contours from the displacement of 1.5 to 2.4 *mm*, some of the high-stress areas fractured and were deactivated by the software, thus their stresses reduced to a very small value (blue color in Figure 5.7).

5.4.2. Bone as a brittle material

By implementing a similar procedure as used for the ductile material, the set of nine training femoral FE models were employed to determine the coefficients of yield criteria (Eq. 2) and to simulate the behavior of bones as brittle materials. In this algorithm, instead of yield forces, the estimated ultimate forces were used in the objective function. The obtained density-yield strain relationship was then cross-validated on the validation femoral set. The coefficients of the relationship were as f = 0.01, and g = -0.5. Figure 5.9 shows the FE estimated ultimate forces versus experimental ultimate forces for both the training and the validation femoral sets. The coefficient of determination R^2 of the estimated ultimate force compared to the desired line $Y = X$ was 0.86 and 0.85 for the training and the validation femora, respectively.

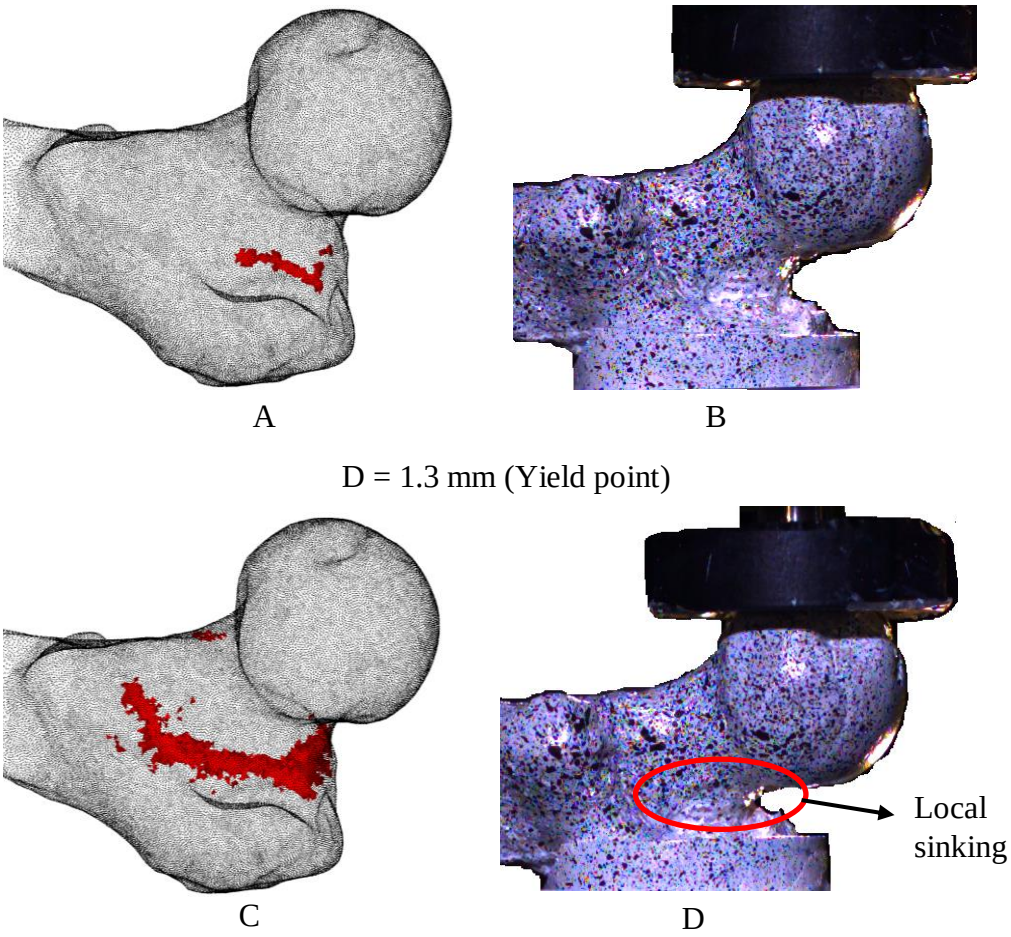

Figure 5.6. Yielded elements in a typical femoral FE model using bilinear (ductile) material model at the onset of yielding and fracture and corresponding experimental illustrations; A, C) yielded elements predicted in FEA, B, D) their corresponding experiments, and E) the number of yielded and fractured elements versus displacement loading. (Used with permission of Mayo Foundation for Medical Education and Research, all rights reserved).

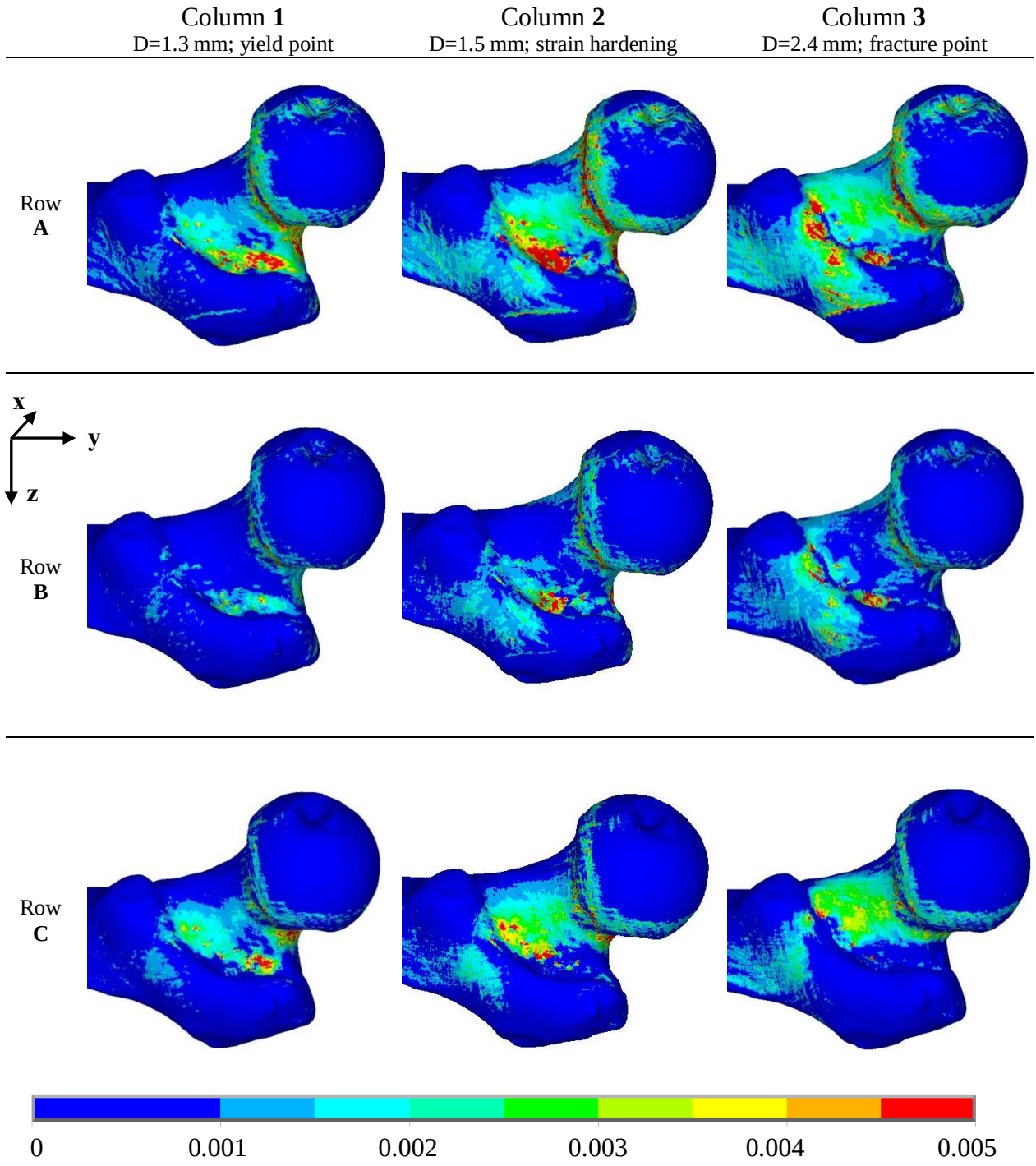

Figure 5.7. Strain contour plots in a typical femoral model using bilinear material model at the onset of yielding, strain hardening, and fracture; Rows A, B, and C correspond to von Mises (ε_{vm}), maximum principal (ε_{max}), and shear (ε_{yz}) strains. (Used with permission of Mayo Foundation for Medical Education and Research, all rights reserved).

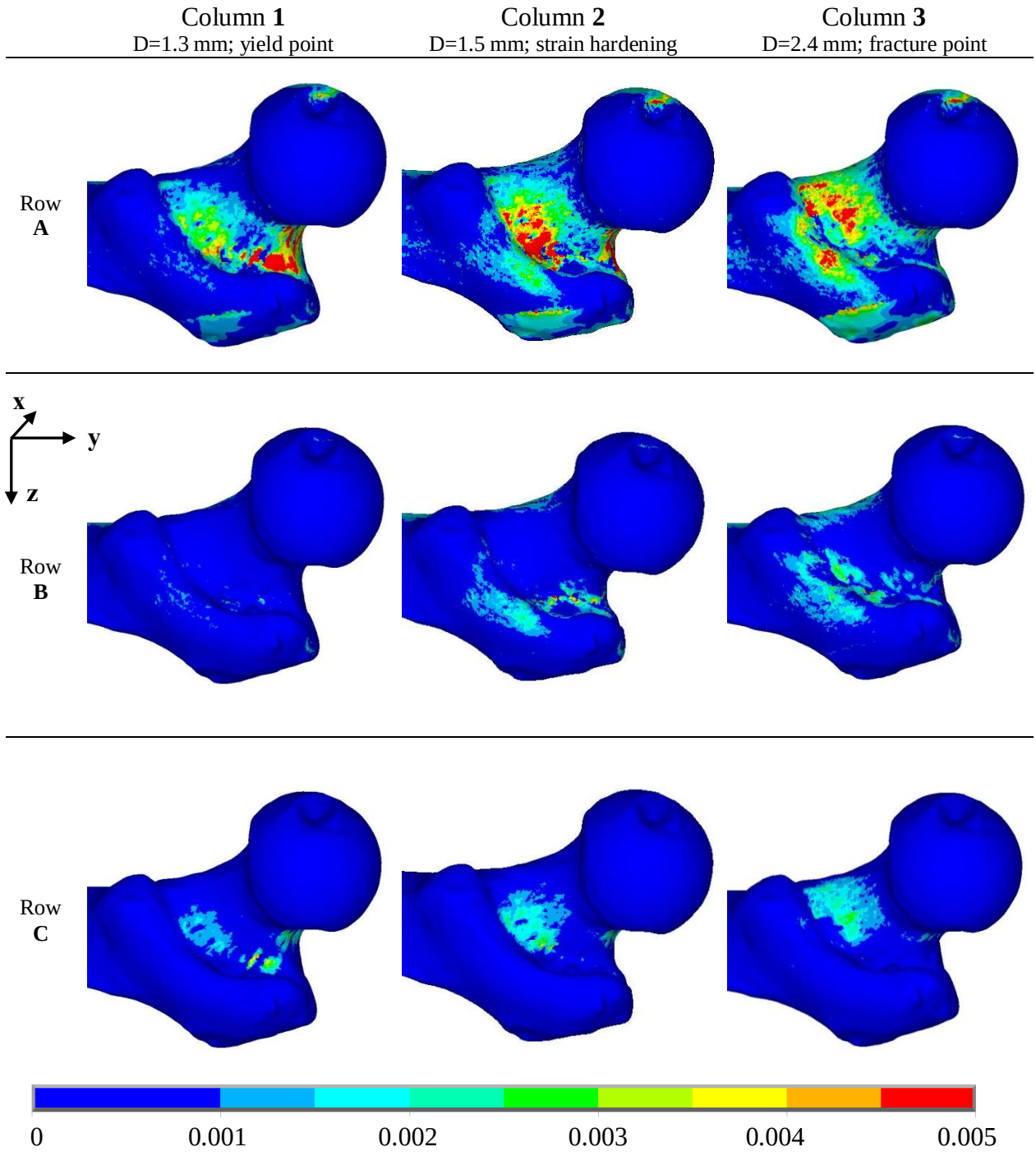

Figure 5.8. Stress contour plots in a typical femoral model using bilinear material model at the onset of yielding, strain hardening, and fracture; Rows A, B, and C correspond to von Mises (σ_{vm}, *MPa*), maximum principal (σ_{max}), and shear (σ_{yz}) stresses. (Used with permission of Mayo Foundation for Medical Education and Research, all rights reserved).

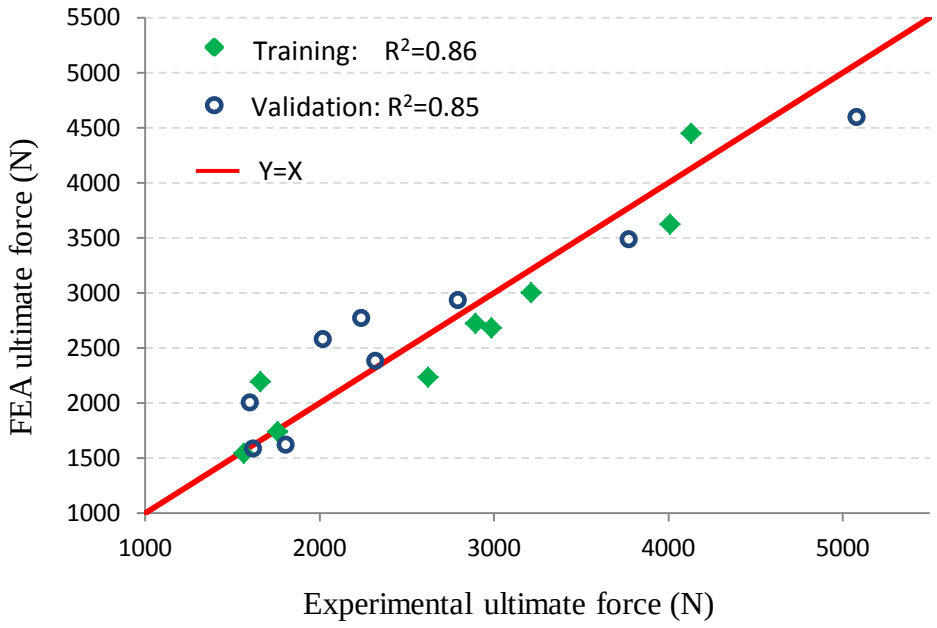

Figure 5.9. Variation of the FE estimated ultimate force versus experimental ultimate force for training and validation femora using the optimal density-yield strain relation ($\varepsilon_y = 0.01\rho_{ash}^{-0.5}$); the coefficient of determination R^2, with respect to desired line $Y = X$, was 0.86 and 0.85 for training and validation femora, respectively. (Used with permission of Mayo Foundation for Medical Education and Research, all rights reserved).

This material model was easy to implement and computationally affordable as the whole process was linear. It was also not necessary to run the FE models after the bones experienced ultimate forces that eased the concern of convergence issues and as soon as the force began to reduce, the simulation could stop.

Figure 5.10 shows the number of fractured elements vs displacement of the femoral head for both material models. At the displacement 1 *mm*, the element began to fracture. As depicted, up to the displacement of 1.5 *mm*, for this specific femur, the number of fractured elements was very small. Thereafter, the number of fractured elements in the brittle material model was, however, exponentially increased. This was logical as the process of damaging in brittle materials occurred far faster than ductile materials. In the ductile model, however, the rate of elements damaging had almost a constant pattern up to the final fracture.

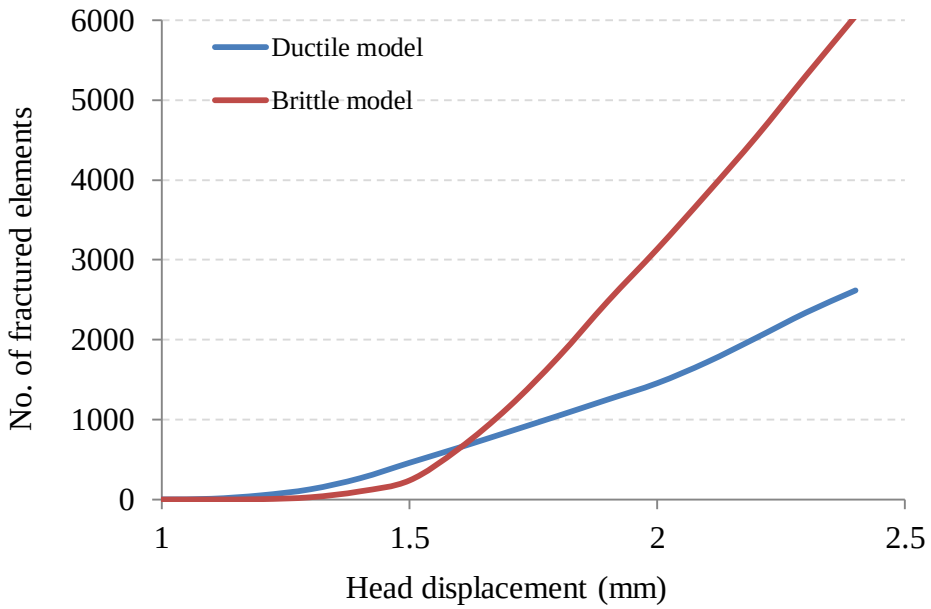

Figure 5.10 Number of fractured elements in a femoral FE model using two material models. (Used with permission of Mayo Foundation for Medical Education and Research, all rights reserved).

Figure 5.11 compares the performance of the ductile and the brittle models along with the experiment. Both the proposed material models reasonably predicted the fracture force. However, the ductile model showed a closer agreement in terms of displacement to fracture. The energy to fracture could also be more accurately determined with the ductile model. The bilinear model, which brought nonlinearity to the FEA, required smaller step size, however, and was also sensitive to the element type and size that needed to be carefully treated in the modeling process.

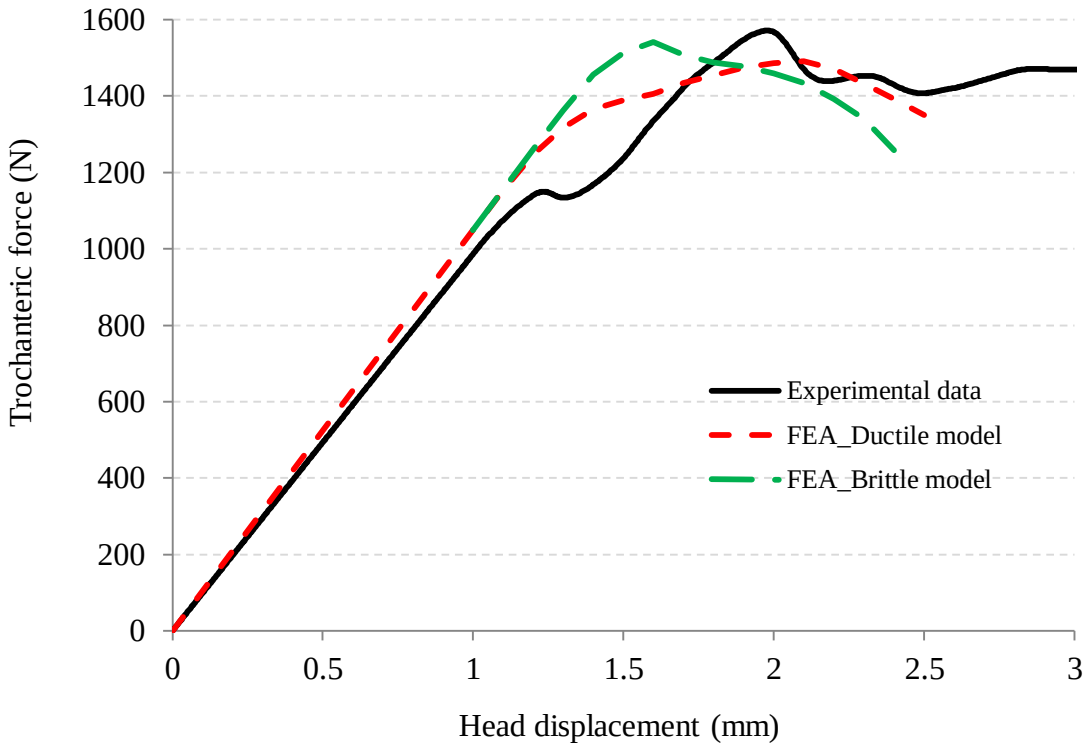

Figure 5.11. Experimental and FE estimated force-displacement data for a femur; optimal density-yield strain relationships for ductile and brittle material models were employed separately in the FE modeling. (Used with permission of Mayo Foundation for Medical Education and Research, all rights reserved).

For this specific femoral data, the linear brittle model under-predicted the fracture displacement of the bone and, consequently, under-predicted the energy of the fracture load. In practice, however, it is more desirable to anticipate the fracture force than the displacement in a fall event because of the fact that this is the force that breaks the bone. Based on the fracture force, the two models showed similar predictive performance. However, the computational time of the two material models was quite different; it took about 7.5 hours to run a simulation using the ductile material model while the same FE model employing the linear brittle material model took about 3 hours to run for the same number of loading steps. This numerically affordable characteristic of the brittle model was of clinical interest.

5.5. Conclusion

The objective of the current study was to characterize the yield and post-yield behavior of female femora in a fall on the hip loading configuration. Both ductile and brittle material models were applied separately on the FE models simulating the fracture experiments. A GA optimization process was used to identify the unknown coefficients in the power density-yield strain relationship by minimizing the error function between the FE estimated and experimental force results. Although both ductile and brittle material models predicted the fracture force properly, the ductile model showed a closer agreement in terms of displacement and energy to fracture. In terms of technical issues, such as computational time and convergence rate, the linear model was more efficient and applicable for clinical use. The rate of element deactivation to simulate material degradation was initially higher in the bilinear model. After the displacement of 1.5 *mm* (FE fracture force for brittle model), however, the rate of degradation in the linear model increased dramatically.

CHAPTER 6. CONCLUSIONS AND RECOMMENDATIONS FOR FUTURE RESEACH

6.1. Summary and Conclusions

A numerical-experimental study was conducted to characterize the inhomogeneous mechanical properties of female bones. One hundred-four fresh-frozen cadaveric femora were previously tested, at Mayo Clinic, to fracture in a fall on the hip loading configuration. The force-displacement data were recorded for each femur. FE models of the femora were developed from the QCT scans, captured before the experiments. A mesh sensitivity analysis was carried out to determine the optimal mesh size, considering the accuracy as well as the numerical cost of FE simulations which mimicked the fracture tests. The analysis was performed on a relatively large sample size of 24 femora. The optimum mesh sizes were found to be around 1.5 *mm* for the head and neck regions, 2.5 *mm* for the subtrochanteric area, and 4.0 *mm* for the shaft.

As the main core of the current study, mechanical properties of the bone were examined in chapter 5 and 6. The focus of the current study was the elastic behavior of the femoral bones as well as their yield and post yield behavior. A set of 35 female femora was randomly selected to obtain optimal elastic properties of such bones. Two different density-elasticity relationships were selected and separately implemented. A combination of several software programs was employed to integrate optimization tools used to identify the unknown coefficients of the density-elasticity relationships. The process was controlled by a sophisticated in-house code in TCL, developed at Mayo Clinic. The performance of the optimal density-elasticity relationships on another set of 35 femora was as good as on the first set. This showed the robustness of the relationships. Interestingly enough, the softer materials of the bone with the densities up to 0.5 g/cm^3 played an important role in the global response of the femur, as more than 70 percent of the bone in the head and neck region belonged to this range of densities. Comparing the results

of the current study with those presented in the study by Morgan et al. [66] showed that coupon tests might be used to characterize the elasticity of femoral bones, provided the samples are excised from the neck region. Comparing the FE estimated results obtained from the density-elasticity relationships proposed by Keller [64] and Keyak et al. [65] with the experimental results in the current study, showed that the mechanical properties of the bone are site-dependent. This finding was in agreement with the conclusion of the study conducted by Morgan et al. [66].

In chapter 5, the suitability of a bilinear material model and a linear material model was tested. The bilinear material model was applied to a set of 9 femoral FE models to simulate the bone plasticity. This addressed the hypothesis that bones undergo plasticity before a final fracture. The linear material model was then applied to the set of 9 femoral models to show the brittleness in the bone response. In both material models, the elements at the onset of fracture were deactivated to have no further influence on the deformation. The same optimization procedure was employed to identify the unknown coefficients in the bone density-yield strain relationship using the FE estimated and experimental fracture forces. The results of both material models showed acceptable correlations with their experimental counterparts. The linear model showed better performance, however, for clinical purposes in terms of applicability and computational cost.

6.2. Recommendations for Future Research

The current study covered the characterization of mechanical properties of bones from the elastic to the damage regions, in order to address the application of FE analysis in fracture and failure mechanics of bones. There are several limitations that should be investigated in the future studies:

1. The main issue with the current study was the use of cadaveric femoral bones. The mechanical properties of bones from in-vivo to in-vitro can be degraded significantly. The results of mechanical characterization in the current study may not, therefore, be applicable to all situations. Additional research should be conducted on the transition from cadaveric mechanical properties to patients.
2. Issues such as beam hardening arising from CT scanning if the bone is scanned without the surrounding soft tissues can affect the determination of bone density and, consequently, of material properties. Moreover, the difference of contrast in CT scans of an in-vivo bone compared to a cadaveric bone affects the segmentation process and consequently the geometry of the reconstructed bone model. Therefore, further investigation should be carried out to correlate in-vivo to in-vitro CT data.
3. Using the proposed elastic properties, the FE estimations showed a good correlation of about 70% with experimental results. Some researchers believe that improvement in this area could be made if the bone material properties are considered anisotropic [68, 114] Further investigations are required in this regard.
4. Mechanical properties of the bone are strain-rate dependent. However, in the current study the bone was considered as a time-independent material due to difficulties in modeling the time-dependency of its material properties. Future studies should be focused on identifying a strain-rate dependent constitutive material equation for femoral bones to improve the accuracy of the QCT/FEA models.
5. During a fall on the hip, the femur does not have direct contact with the ground, as a layer of soft tissue helps attenuate the level of transferred load to the bone. Future

studies should address the influence of soft tissue to more accurately estimate loading to the bone.

REFERENCES

[1] Cowin SC. Bone mechanics handbook. 2001.

[2] Ritchie RO. How does human bone resist fracture? Annals of the New York Academy of Sciences 2010;1192:72-80.

[3] Nalla RK, Kinney JH, Ritchie RO. Mechanistic fracture criteria for the failure of human cortical bone. Nature materials 2003;2:164-8.

[4] Ritchie RO, Buehler MJ, Hansma P. Plasticity and toughness in bone. Phys Today 2009;62:41-7.

[5] Taylor D, Hazenberg JG, Lee TC. Living with cracks: damage and repair in human bone. Nature materials 2007;6:263-8.

[6] Nalla R, Stölken J, Kinney J, Ritchie R. Fracture in human cortical bone: local fracture criteria and toughening mechanisms. Journal of biomechanics 2005;38:1517-25.

[7] Peterlik H, Roschger P, Klaushofer K, Fratzl P. From brittle to ductile fracture of bone. Nature materials 2005;5:52-5.

[8] Zimmermann EA, Launey ME, Barth HD, Ritchie RO. Mixed-mode fracture of human cortical bone. Biomaterials 2009;30:5877-84.

[9] Unnanuntana A, Gladnick BP, Donnelly E, Lane JM. The assessment of fracture risk. The Journal of Bone & Joint Surgery 2010;92:743-53.

[10] Baim S, Leslie WD. Assessment of fracture risk. Current osteoporosis reports 2012;10:28-41.

[11] Wang R, Gupta HS. Deformation and fracture mechanisms of bone and nacre. Annual Review of Materials Research 2011;41:41-73.

[12] Cummings SR, Browner W, Cummings S, Black D, Nevitt M, Genant H, et al. Bone density at various sites for prediction of hip fractures. The Lancet 1993;341:72-5.

[13] Hui SL, Slemenda CW, Johnston Jr CC. Age and bone mass as predictors of fracture in a prospective study. Journal of clinical investigation 1988;81:1804.

[14] Cummings SR, Nevitt MC, Browner WS, Stone K, Fox KM, Ensrud KE, et al. Risk factors for hip fracture in white women. New England journal of medicine 1995;332:767-74.

[15] De Laet C, Kanis J, Odén A, Johanson H, Johnell O, Delmas P, et al. Body mass index as a predictor of fracture risk: a meta-analysis. Osteoporosis International 2005;16:1330-8.

[16] Robbins JA, Schott AM, Garnero P, Delmas PD, Hans D, Meunier PJ. Risk factors for hip fracture in women with high BMD: EPIDOS study. Osteoporosis Int 2005;16:149-54.

[17] Sambrook PN, Flahive J, Hooven FH, Boonen S, Chapurlat R, Lindsay R, et al. Predicting Fractures in an International Cohort Using Risk Factor Algorithms Without BMD. Journal of Bone and Mineral Research 2011;26:2770-7.

[18] Wainwright SA, Marshall LM, Ensrud KE, Cauley JA, Black DM, Hillier TA, et al. Hip fracture in women without osteoporosis. J Clin Endocr Metab 2005;90:2787-93.

[19] Schuit S, Van der Klift M, Weel A, De Laet C, Burger H, Seeman E, et al. Fracture incidence and association with bone mineral density in elderly men and women: the Rotterdam Study. Bone 2004;34:195-202.

[20] Currey JD. Bones: structure and mechanics: Princeton University Press; 2002.

[21] Bronner F, Farach-Carson MC, Roach HI. Bone-metabolic Functions and Modulators: Springer; 2012.

[22] Quarles LD. Endocrine functions of bone in mineral metabolism regulation. The Journal of clinical investigation 2008;118:3820-8.

[23] Fernández KS, de Alarcón PA. Development of the Hematopoietic System and Disorders of Hematopoiesis that Present During Infancy and Early Childhood. Pediatric clinics of North America 2013;60:1273-89.

[24] Olszta MJ, Cheng X, Jee SS, Kumar R, Kim Y-Y, Kaufman MJ, et al. Bone structure and formation: A new perspective. Materials Science and Engineering: R: Reports 2007;58:77-116.

[25] Rho J-Y, Kuhn-Spearing L, Zioupos P. Mechanical properties and the hierarchical structure of bone. Medical engineering & physics 1998;20:92-102.

[26] Steele DG. The anatomy and biology of the human skeleton: Texas A&M University Press; 1988.

[27] Augat P, Schorlemmer S. The role of cortical bone and its microstructure in bone strength. Age and ageing 2006;35:ii27-ii31.

[28] Keaveny TM, Morgan EF, Niebur GL, Yeh OC. Biomechanics of trabecular bone. Annual review of biomedical engineering 2001;3:307-33.

[29] Netter FH, Crelin ES, Kaplan FS, Woodburne RT. Musculoskeletal System: A Compilation of Paintings. Anatomy, Physiology, and Metabolic Disorders; Russell T. Woodburne, Edmund S. Crelin and Frederick S. Kaplan, Consulting Editors; Regina V. Dingle, Managing Editor: Ciba-Geigy Corporation; 1987.

[30] WHO. Prevention and management of osteoporosis: report of a WHO scientific group: Diamond Pocket Books (P) Ltd.; 2003.

[31] Teitelbaum SL. Bone resorption by osteoclasts. Science 2000;289:1504-8.

[32] Caetano-Lopes J, Canhao H, Fonseca JE. Osteoblasts and bone formation. Acta reumatológica portuguesa 2006;32:103-10.

[33] Hadjidakis DJ, Androulakis II. Bone remodeling. Annals of the New York Academy of Sciences 2006;1092:385-96.

[34] Manolagas SC. Birth and death of bone cells: basic regulatory mechanisms and implications for the pathogenesis and treatment of osteoporosis 1. Endocrine reviews 2000;21:115-37.

[35] Feng X, McDonald JM. Disorders of bone remodeling. Annual review of pathology 2011;6:121.

[36] Hernlund E, Svedbom A, Ivergård M, Compston J, Cooper C, Stenmark J, et al. Osteoporosis in the European Union: medical management, epidemiology and economic burden. Archives of osteoporosis 2013;8:1-115.

[37] Cummings SR, Melton LJ. Epidemiology and outcomes of osteoporotic fractures. The Lancet 2002;359:1761-7.

[38] Johnell O, Kanis J. An estimate of the worldwide prevalence and disability associated with osteoporotic fractures. Osteoporosis International 2006;17:1726-33.

[39] Cooper C, Cole Z, Holroyd C, Earl S, Harvey N, Dennison E, et al. Secular trends in the incidence of hip and other osteoporotic fractures. Osteoporosis International 2011;22:1277-88.

[40] Health UDo, Services H. Bone health and osteoporosis: a report of the Surgeon General. Rockville, MD: US Department of Health and Human Services, Office of the Surgeon General; 2004.

[41] Magaziner J, Hawkes W, Hebel JR, Zimmerman SI, Fox KM, Dolan M, et al. Recovery from hip fracture in eight areas of function. The Journals of Gerontology Series A: Biological Sciences and Medical Sciences 2000;55:M498-M507.

[42] Cooper C, Campion G, Melton Iii L. Hip fractures in the elderly: a world-wide projection. Osteoporosis International 1992;2:285-9.

[43] Torio CM, Andrews RM. National inpatient hospital costs: the most expensive conditions by payer, 2011. 2013.

[44] Deprey SM. Descriptive analysis of fatal falls of older adults in a Midwestern county in the year 2005. Journal of geriatric physical therapy 2009;32:23-8.

[45] Hayes WC, Myers ER, Morris JN, Gerhart TN, Yett HS, Lipsitz LA. Impact near the hip dominates fracture risk in elderly nursing home residents who fall. Calcified tissue international 1993;52:192-8.

[46] Marks R, Allegrante JP, Ronald MacKenzie C, Lane JM. Hip fractures among the elderly: causes, consequences and control. Ageing research reviews 2003;2:57-93.

[47] Parkkari J, Kannus P, Palvanen M, Natri A, Vainio J, Aho H, et al. Majority of hip fractures occur as a result of a fall and impact on the greater trochanter of the femur: a prospective controlled hip fracture study with 206 consecutive patients. Calcified tissue international 1999;65:183-7.

[48] Jordan K, Cooper C. Epidemiology of osteoporosis. Best Practice & Research Clinical Rheumatology 2002;16:795-806.

[49] Bonnick SL. Dual-energy x-ray absorptiometry: interpreting reports and serial measurements. Clinical obstetrics and gynecology 2013;56:677-85.

[50] WHO. Assessment of fracture risk and its application to screening for postmenopausal osteoporosis: report of a WHO study group [meeting held in Rome from 22 to 25 June 1992]. 1994.

[51] Kanis JA. Diagnosis of osteoporosis and assessment of fracture risk. The Lancet 2002;359:1929-36.

[52] Lochmüller EM, Müller R, Kuhn V, Lill CA, Eckstein F. Can novel clinical densitometric techniques replace or improve DXA in predicting bone strength in osteoporosis at the hip and other skeletal sites? Journal of bone and mineral research 2003;18:906-12.

[53] Wakao N, Harada A, Matsui Y, Takemura M, Shimokata H, Mizuno M, et al. The effect of impact direction on the fracture load of osteoporotic proximal femurs. Medical engineering & physics 2009;31:1134-9.

[54] Dragomir-Daescu D, Op Den Buijs J, McEligot S, Dai Y, Entwistle RC, Salas C, et al. Robust QCT/FEA models of proximal femur stiffness and fracture load during a sideways fall on the hip. Annals of biomedical engineering 2011;39:742-55.

[55] Mccreadie BR, Goldstein SA. Biomechanics of fracture: is bone mineral density sufficient to assess risk? Journal of bone and mineral research 2000;15:2305-8.

[56] Ahlborg HG, Johnell O, Turner CH, Rannevik G, Karlsson MK. Bone loss and bone size after menopause. New England journal of medicine 2003;349:327-34.

[57] Lotz J, Cheal E, Hayes W. Fracture prediction for the proximal femur using finite element models: part I—linear analysis. Journal of biomechanical engineering 1991;113:353-60.

[58] Langton C, Pisharody S, Keyak J. Comparison of 3D finite element analysis derived stiffness and BMD to determine the failure load of the excised proximal femur. Medical engineering & physics 2009;31:668-72.

[59] Juszczyk MM, Cristofolini L, Viceconti M. The human proximal femur behaves linearly elastic up to failure under physiological loading conditions. Journal of biomechanics 2011;44:2259-66.

[60] Koivumäki JE, Thevenot J, Pulkkinen P, Kuhn V, Link TM, Eckstein F, et al. Ct-based finite element models can be used to estimate experimentally measured failure loads in the proximal femur. Bone 2012;50:824-9.

[61] Hambli R, Allaoui S. A Robust 3D Finite Element Simulation of Human Proximal Femur Progressive Fracture Under Stance Load with Experimental Validation. Ann Biomed Eng 2013;41:2515-27.

[62] Yosibash Z, Trabelsi N, Milgrom C. Reliable simulations of the human proximal femur by high-order finite element analysis validated by experimental observations. Journal of biomechanics 2007;40:3688-99.

[63] Taddei F, Cristofolini L, Martelli S, Gill H, Viceconti M. Subject-specific finite element models of long bones: an in vitro evaluation of the overall accuracy. Journal of biomechanics 2006;39:2457-67.

[64] Keller TS. Predicting the compressive mechanical behavior of bone. J Biomech 1994;27:1159-68.

[65] Keyak J, Lee I, Skinner H. Correlations between orthogonal mechanical properties and density of trabecular bone: use of different densitometric measures. Journal of biomedical materials research 1994;28:1329-36.

[66] Morgan EF, Bayraktar HH, Keaveny TM. Trabecular bone modulus–density relationships depend on anatomic site. Journal of biomechanics 2003;36:897-904.

[67] Cong A, Buijs JOD, Dragomir-Daescu D. In situ parameter identification of optimal density–elastic modulus relationships in subject-specific finite element models of the proximal femur. Medical engineering & physics 2011;33:164-73.

[68] Eberle S, Göttlinger M, Augat P. Individual density–elasticity relationships improve accuracy of subject-specific finite element models of human femurs. Journal of biomechanics 2013;46:2152-7.

[69] Javid S, Kushvaha V, Karami G, McEligot S, Dragomir-Daescu D. Cadaveric Femoral Fractures in a Fall on the Hip Configuration. Mechanics of Biological Systems and Materials, Volume 4: Springer; 2014. p. 53-7.

[70] Courtney AC, Wachtel EF, Myers ER, Hayes WC. Age-related reductions in the strength of the femur tested in a fall-loading configuration. The Journal of bone and joint surgery American volume 1995;77:387-95.

[71] Ito M, Wakao N, Hida T, Matsui Y, Abe Y, Aoyagi K, et al. Analysis of hip geometry by clinical CT for the assessment of hip fracture risk in elderly Japanese women. Bone 2010;46:453-7.

[72] Courtney AC, Wachtel EF, Myers ER, Hayes WC. Effects of Loading Rate on Strength of the Proximal Femur (Vol 55, Pg 53, 1994). Calcified tissue international 1994;55:402-.

[73] Eckstein F, Wunderer C, Boehm H, Kuhn V, Priemel M, Link TM, et al. Reproducibility and side differences of mechanical tests for determining the structural strength of the proximal femur. Journal of bone and mineral research : the official journal of the American Society for Bone and Mineral Research 2004;19:379-85.

[74] Pinilla TP, Boardman KC, Bouxsein ML, Myers ER, Hayes WC. Impact direction from a fall influences the failure load of the proximal femur as much as age-related bone loss. Calcified tissue international 1996;58:231-5.

[75] Roberts BJ, Thrall E, Muller JA, Bouxsein ML. Comparison of hip fracture risk prediction by femoral aBMD to experimentally measured factor of risk. Bone 2010;46:742-6.

[76] Pulkkinen P, Jämsä T, Lochmüller E-M, Kuhn V, Nieminen M, Eckstein F. Experimental hip fracture load can be predicted from plain radiography by combined analysis of trabecular bone structure and bone geometry. Osteoporosis International 2008;19:547-58.

[77] Müller M. Müller AO Classification of Fractures–Long Bones. AO Publishing; 2004.

[78] Kinzl M, Wolfram U, Pahr D. Identification of a crushable foam material model and application to strength and damage prediction of human femur and vertebral body. Journal of the mechanical behavior of biomedical materials 2013;26:136-47.

[79] Dalle Carbonare L, Giannini S. Bone microarchitecture as an important determinant of bone strength. Journal of endocrinological investigation 2004;27:99-105.

[80] Nielsen SP. The fallacy of BMD: a critical review of the diagnostic use of dual X-ray absorptiometry. Clinical rheumatology 2000;19:174-83.

[81] Yang L, Peel N, Clowes JA, McCloskey EV, Eastell R. Use of DXA-Based Structural Engineering Models of the Proximal Femur to Discriminate Hip Fracture. Journal of bone and mineral research 2009;24:33-42.

[82] Gong H, Zhang M, Fan Y, Kwok WL, Leung PC. Relationships between femoral strength evaluated by nonlinear finite element analysis and BMD, material distribution and geometric morphology. Ann Biomed Eng 2012;40:1575-85.

[83] Schileo E, Taddei F, Malandrino A, Cristofolini L, Viceconti M. Subject-specific finite element models can accurately predict strain levels in long bones. Journal of biomechanics 2007;40:2982-9.

[84] Austman RL, Milner JS, Holdsworth DW, Dunning CE. The effect of the density–modulus relationship selected to apply material properties in a finite element model of long bone. Journal of biomechanics 2008;41:3171-6.

[85] Trabelsi N, Yosibash Z, Wutte C, Augat P, Eberle S. Patient-specific finite element analysis of the human femur—a double-blinded biomechanical validation. Journal of biomechanics 2011;44:1666-72.

[86] Keyak JH, Rossi SA, Jones KA, Skinner HB. Prediction of femoral fracture load using automated finite element modeling. Journal of biomechanics 1997;31:125-33.

[87] Schileo E, Dall'Ara E, Taddei F, Malandrino A, Schotkamp T, Baleani M, et al. An accurate estimation of bone density improves the accuracy of subject-specific finite element models. Journal of biomechanics 2008;41:2483-91.

[88] Bouxsein M, Myers E, Hayes W. Biomechanics of age-related fractures. Osteoporosis 2001;1:601-16.

[89] Eberle S, Göttlinger M, Augat P. An investigation to determine if a single validated density–elasticity relationship can be used for subject specific finite element analyses of human long bones. Medical engineering & physics 2013;35:875-83.

[90] Dall'Ara E, Luisier B, Schmidt R, Kainberger F, Zysset P, Pahr D. A nonlinear QCT-based finite element model validation study for the human femur tested in two configurations< i> in vitro</i>. Bone 2013;52:27-38.

[91] Haider IT, Speirs AD, Frei H. Effect of boundary conditions, impact loading and hydraulic stiffening on femoral fracture strength. Journal of biomechanics 2013;46:2115-21.

[92] Taddei F, Schileo E, Helgason B, Cristofolini L, Viceconti M. The material mapping strategy influences the accuracy of CT-based finite element models of bones: an evaluation against experimental measurements. Medical engineering & physics 2007;29:973-9.

[93] Helgason B, Perilli E, Schileo E, Taddei F, Brynjólfsson S, Viceconti M. Mathematical relationships between bone density and mechanical properties: a literature review. Clinical Biomechanics 2008;23:135-46.

[94] Bessho M, Ohnishi I, Matsuyama J, Matsumoto T, Imai K, Nakamura K. Prediction of strength and strain of the proximal femur by a CT-based finite element method. Journal of biomechanics 2007;40:1745-53.

[95] Burdick RK, Borror CM, Montgomery DC. Design and analysis of gauge R&R studies: Making decisions with confidence intervals in random and mixed ANOVA models: SIAM; 2005.

[96] Luo Y, Ferdous Z, Leslie WD. Precision study of DXA-based patient-specific finite element modeling for assessing hip fracture risk. International journal for numerical methods in biomedical engineering 2013;29:615-29.

[97] Lee YS, Mihata T, Oh JH. Anatomically reproducible assessment of volumetric bone mineral density—Based on clinical computed tomography. Journal of biomechanics 2013;46:767-72.

[98] Javid S, Karami G, Rezaei A, Azarmi F. Micromechanics of Unidirectional Viscoelastic Fibrous Composites-Homogenized vs Local Characterization. Journal of Multifunctional Composites 2013;1.

[99] Verhulp E, van Rietbergen B, Huiskes R. Comparison of micro-level and continuum-level voxel models of the proximal femur. Journal of biomechanics 2006;39:2951-7.

[100] Barnhart HX, Haber M, Song J. Overall concordance correlation coefficient for evaluating agreement among multiple observers. Biometrics 2002;58:1020-7.

[101] Carrasco JL, Jover L. Estimating the generalized concordance correlation coefficient through variance components. Biometrics 2003;59:849-58.

[102] Pettersen SH, Wik TS, Skallerud B. Subject specific finite element analysis of stress shielding around a cementless femoral stem. Clinical Biomechanics 2009;24:196-202.

[103] Shim VB, Pitto RP, Anderson IA. Quantitative CT with finite element analysis: towards a predictive tool for bone remodelling around an uncemented tapered stem. International orthopaedics 2012;36:1363-9.

[104] Tada S, Stegaroiu R, Kitamura E, Miyakawa O, Kusakari H. Influence of implant design and bone quality on stress/strain distribution in bone around implants: a 3-dimensional finite element analysis. The International journal of oral & maxillofacial implants 2002;18:357-68.

[105] Hirata Y, Inaba Y, Kobayashi N, Ike H, Fujimaki H, Saito T. Comparison of Mechanical Stress and Change in Bone Mineral Density Between Two Types of Femoral Implant Using Finite Element Analysis. The Journal of arthroplasty 2013;28:1731-5.

[106] Weis JA, Miga MI, Granero-Moltó F, Spagnoli A. A finite element inverse analysis to assess functional improvement during the fracture healing process. Journal of biomechanics 2010;43:557-62.

[107] Christen D, Webster DJ, Müller R. Multiscale modelling and nonlinear finite element analysis as clinical tools for the assessment of fracture risk. Philosophical Transactions of the Royal Society A: Mathematical, Physical and Engineering Sciences 2010;368:2653-68.

[108] Schileo E, Taddei F, Cristofolini L, Viceconti M. Subject-specific finite element models implementing a maximum principal strain criterion are able to estimate failure risk and fracture location on human femurs tested< i> in vitro</i>. Journal of biomechanics 2008;41:356-67.

[109] Helgason B, Taddei F, Pálsson H, Schileo E, Cristofolini L, Viceconti M, et al. A modified method for assigning material properties to FE models of bones. Medical engineering & physics 2008;30:444-53.

[110] Carter DR, Hayes WC. The compressive behavior of bone as a two-phase porous structure. The Journal of Bone & Joint Surgery 1977;59:954-62.

[111] Keyak JH, Falkinstein Y. Comparison of in situ and in vitro CT scan-based finite element model predictions of proximal femoral fracture load. Medical engineering & physics 2003;25:781-7.

[112] Hambli R, Bettamer A, Allaoui S. Finite element prediction of proximal femur fracture pattern based on orthotropic behaviour law coupled to quasi-brittle damage. Medical engineering & physics 2012;34:202-10.

[113] Espinoza Orías AA, Deuerling JM, Landrigan MD, Renaud JE, Roeder RK. Anatomic variation in the elastic anisotropy of cortical bone tissue in the human femur. Journal of the mechanical behavior of biomedical materials 2009;2:255-63.

[114] Rudy DJ, Deuerling JM, Espinoza Orías AA, Roeder RK. Anatomic variation in the elastic inhomogeneity and anisotropy of human femoral cortical bone tissue is consistent across multiple donors. Journal of biomechanics 2011;44:1817-20.

[115] Huang H-L, Tsai M-T, Lin D-J, Chien C-S, Hsu J-T. A new method to evaluate the elastic modulus of cortical bone by using a combined computed tomography and finite element approach. Computers in biology and medicine 2010;40:464-8.

[116] Foundation NO. America's Bone Health: The State of Osteoporosis and Low Bone Massin Our Nation. 2002.

[117] Kauer M, Vuskovic V, Dual J, Székely G, Bajka M. Inverse finite element characterization of soft tissues. Medical Image Analysis 2002;6:275-87.

[118] Lotz JC, Gerhart TN, Hayes WC. Mechanical properties of trabecular bone from the proximal femur: a quantitative CT study. Journal of computer assisted tomography 1990;14:107-14.

[119] Lotz JC, Gerhart TN, Hayes WC. Mechanical properties of metaphyseal bone in the proximal femur. Journal of biomechanics 1991;24:317-29.

[120] Snyder SM, Schneider E. Estimation of mechanical properties of cortical bone by computed tomography. Journal of Orthopaedic Research 1991;9:422-31.

[121] Hodgskinson R, Currey J. Young's modulus, density and material properties in cancellous bone over a large density range. Journal of Materials Science: Materials in Medicine 1992;3:377-81.

[122] Linde F, Hvid I, Madsen F. The effect of specimen geometry on the mechanical behaviour of trabecular bone specimens. Journal of biomechanics 1992;25:359-68.

[123] Anderson MJ, Keyak J, Skinner H. Compressive mechanical properties of human cancellous bone after gamma irradiation. J Bone Joint Surg Am 1992;74:747-52.

[124] Dalstra M, Huiskes R, Odgaard A, Van Erning L. Mechanical and textural properties of pelvic trabecular bone. Journal of biomechanics 1993;26:523-35.

[125] Goulet RW, Goldstein SA, Ciarelli MJ, Kuhn JL, Brown M, Feldkamp L. The relationship between the structural and orthogonal compressive properties of trabecular bone. Journal of biomechanics 1994;27:375-89.

[126] Keaveny TM, Pinilla TP, Crawford RP, Kopperdahl DL, Lou A. Systematic and random errors in compression testing of trabecular bone. Journal of Orthopaedic Research 1997;15:101-10.

[127] Li B, Aspden RM. Composition and mechanical properties of cancellous bone from the femoral head of patients with osteoporosis or osteoarthritis. Journal of bone and mineral research 1997;12:641-51.

[128] Ouyang J, Yang G, Wu W, Zhu Q, Zhong S. Biomechanical characteristics of human trabecular bone. Clinical Biomechanics 1997;12:522-4.

[129] Kopperdahl DL, Keaveny TM. Yield strain behavior of trabecular bone. Journal of biomechanics 1998;31:601-8.

[130] Ciarelli T, Fyhrie D, Schaffler M, Goldstein S. Variations in Three-Dimensional Cancellous Bone Architecture of the Proximal Femur in Female Hip Fractures and in Controls. Journal of bone and mineral research 2000;15:32-40.

[131] Kaneko TS, Bell JS, Pejcic MR, Tehranzadeh J, Keyak JH. Mechanical properties, density and quantitative CT scan data of trabecular bone with and without metastases. Journal of biomechanics 2004;37:523-30.

[132] Klein K, Neira J. Nelder-Mead simplex optimization routine for large-scale problems: a distributed memory implementation. Computational Economics 2014;43:447-61.

[133] Lagarias JC, Reeds JA, Wright MH, Wright PE. Convergence properties of the Nelder--Mead simplex method in low dimensions. SIAM Journal on optimization 1998;9:112-47.

[134] Singer S, Nelder J. Nelder-mead algorithm. Scholarpedia 2009;4:2928.

[135] Gao F, Han L. Implementing the Nelder-Mead simplex algorithm with adaptive parameters. Computational Optimization and Applications 2012;51:259-77.

[136] Gupta D. Solving TSP Using Various Meta-Heuristic Algorithms. International Journal of Recent Contributions from Engineering, Science & IT (iJES) 2013;1:pp. 26-30.

[137] Sivanandam S, Deepa S. Introduction to genetic algorithms.: Springer; 2008.

[138] MathWorks. How the Genetic Algorithm Works. 2014.

[139] McElhaney JH. Dynamic response of bone and muscle tissue. J appl Physiol 1966;21:1231-6.

[140] Keyak J. Improved prediction of proximal femoral fracture load using nonlinear finite element models. Med Eng Phys 2001;23:165-73.

[141] Keyak JH, Kaneko TS, Tehranzadeh J, Skinner HB. Predicting proximal femoral strength using structural engineering models. Clinical orthopaedics and related research 2005;437:219-28.

[142] Keyak J, Rossi S, Jones K, Les C, Skinner H. Prediction of fracture location in the proximal femur using finite element models. Medical engineering & physics 2001;23:657-64.

[143] Niebur GL, Feldstein MJ, Yuen JC, Chen TJ, Keaveny TM. High-resolution finite element models with tissue strength asymmetry accurately predict failure of trabecular bone. J Biomech 2000;33:1575-83.

[144] Imai K, Ohnishi I, Bessho M, Nakamura K. Nonlinear finite element model predicts vertebral bone strength and fracture site. Spine 2006;31:1789-94.

[145] Keaveny TM, Hoffmann PF, Singh M, Palermo L, Bilezikian JP, Greenspan SL, et al. Femoral bone strength and its relation to cortical and trabecular changes after treatment with PTH, alendronate, and their combination as assessed by finite element analysis of quantitative CT scans. Journal of bone and mineral research 2008;23:1974-82.

[146] Keaveny TM, Kopperdahl DL, Melton LJ, Hoffmann PF, Amin S, Riggs BL, et al. Age-dependence of femoral strength in white women and men. Journal of bone and mineral research 2010;25:994-1001.

[147] Maghous S, Dormieux L, Barthélémy J. Micromechanical approach to the strength properties of frictional geomaterials. European Journal of Mechanics-A/Solids 2009;28:179-88.

[148] Kelly N, McGarry JP. Experimental and numerical characterisation of the elasto-plastic properties of bovine trabecular bone and a trabecular bone analogue. Journal of the mechanical behavior of biomedical materials 2012;9:184-97.

[149] Zysset P, Rincón L. An alternative fabric-based yield and failure criterion for trabecular bone: Springer; 2006.

[150] Rincón-Kohli L, Zysset PK. Multi-axial mechanical properties of human trabecular bone. Biomechanics and modeling in mechanobiology 2009;8:195-208.

[151] Wolfram U, Gross T, Pahr DH, Schwiedrzik J, Wilke H-J, Zysset PK. Fabric-based Tsai–Wu yield criteria for vertebral trabecular bone in stress and strain space. Journal of the mechanical behavior of biomedical materials 2012;15:218-28.

[152] Launey ME, Buehler MJ, Ritchie RO. On the mechanistic origins of toughness in bone. Annual Review of Materials Research 2010;40:25-53.

[153] Garcia D. Elastic plastic damage laws for cortical bone. 2006.